BREMEN UNIVERSITÄT

Slope stability in the Beaufort Sea, Canadian Arctic

Geohazard analysis focused on gas hydrate dissociation and permafrost thawing

Tiago Biller Teixeira Zuanazzi

WiSe 2015/2016

Supervisors:

Prof. Dr. Achim J. Kopf

Prof. Dr. Tobias Mörz

The Beaufort Sea offshore Northern Canada is an Arctic region that has continuously gained the attention of private and governmental organizations due to its potential for future developments in mineral resource extraction, climatic modification forecasts, opening of navigation routes and several other matters of geopolitical, economic and scientific importance. Currently experiencing notable changes resulting from the warming associated with Holocene sea level rise, the Beaufort Shelf is still accommodating a thermal pulse of about 10°C that has been propagating since the last marine transgression, in which relatively warm waters flooded areas of permafrost occurrence. The harmonization of this thermal contrast creates circumstances where gas hydrates and permafrost can become destabilized, which in turn potentially undermines slope stability. Additionally to the warming rooted on the glacial-interglacial cycle, the broadly accredited present tendencies of anthropogenic climatic change are deemed of sufficient magnitude to be relevant in the problematic here examined. Though many sources of geohazards are at play in this region, this study focuses on the effects of temperature-induced gas hydrate dissociation and permafrost thawing in prompting mass wasting events. Through a number of computational steps based on empirical data and experiments on samples acquired during scientific research expeditions, it is reckoned that rather modest sediment temperature variations are sufficient to cause slope failure at the Beaufort Shelf and Slope.

Table of contents

1. Introduction:

The Canadian Beaufort continental shelf (**Figure 1**) covers an area of 50,000 km2 and stretches from the United States border at 141°W to the entrance of Amundsen Gulf at 128°W, forming a shallow gently sloping plain region from 68°N to 71.5°N, which reaches the shelf break between 90 and 120 m of water depth. The area is divided into three major geographic regions: the Yukon Shelf adjacent the US Border, the Mackenzie Trough and the broad Central Shelf, which can divided into two sub-areas at 133.5°W, where there is a change in surficial sediment from clay (western shelf) to sandier sediments (eastern shelf). This thesis focuses on the Central Shelf.

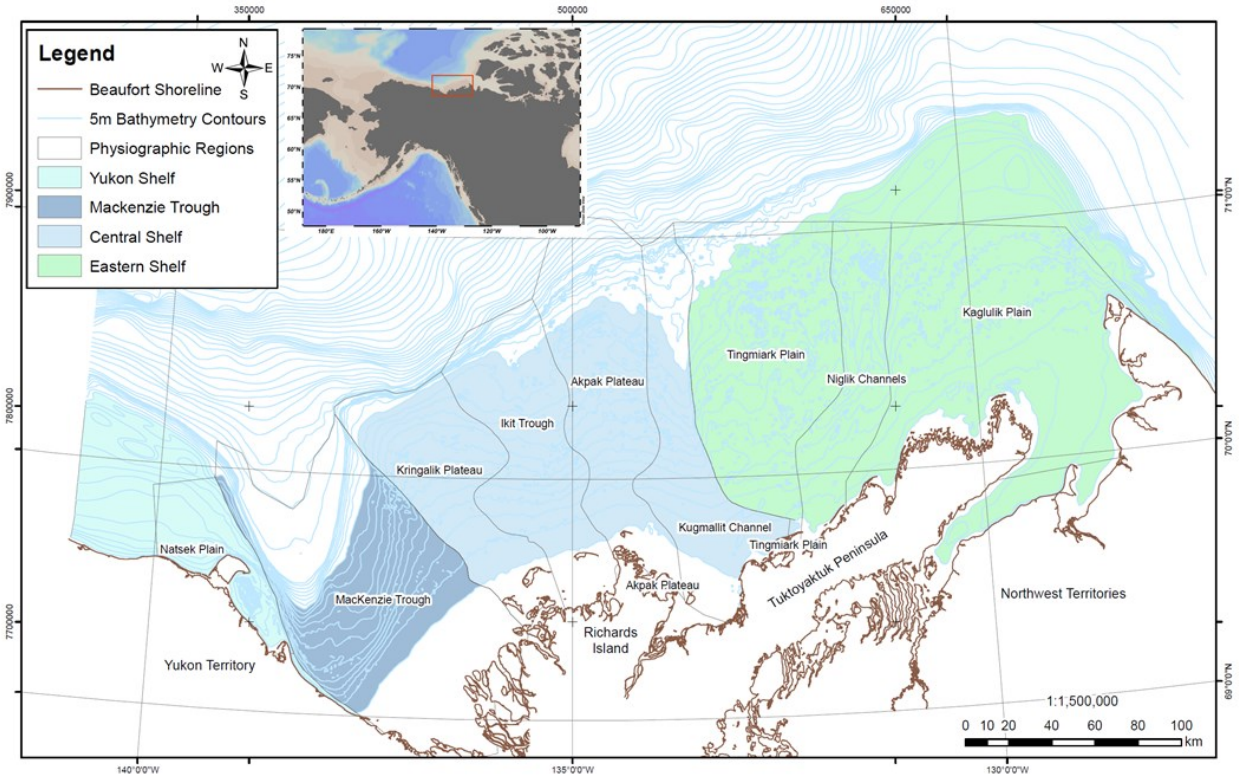

Figure 1: Regional subdivision of the Canadian Beaufort Sea Continental Shelf and detail showing relative position (modified after Blasco et al., 2013)

The Central Shelf is 350 km long, up to 150 km wide and slopes evenly with an average gradient of 0.03°. The smooth relief is interrupted by cross-shelf, partially infilled to infilled linear troughs oriented in the north direction, such as the Ikit Trough and Kugmallit Channel (**Figure 1**).In addition to the break in slope and bathymetry, the edge of the continental shelf is characterized by a number of morphological features and geological structures, including pull-apart basins, grabens, folds, faults and pingo-like

features (PLFs)[1]. Shoreward of the shelf break, the seafloor rises to the shoreline at an average slope of 0.03° to 0.06°. The continental slope is a narrow area with a gradient between 0.5˚ and 6°. Water depth ranges from 100 to 1500 m and width varies from 20 km to 100 km. The slope is generally concave upward and steepest just below the shelf break. Much of the present slope morphology appears to be a result of mass transport processes. The slope is marked by a hummocky surface topography which may represent the downslope movement of sediments.

1.1. Scope

The Arctic continental shelf is presently going through changes provoked by the warming associated with Holocene sea level rises, during which relatively warm waters flooded cold permafrost (PF) areas of the Arctic Shelf. A thermal gradient of over 10^{o}C is still propagating into the submerged sediment, where gas hydrate, as well as PF thawing might take place. (Paull et al, 2007). Hence, this thesis aims to:

- Calculate slope stabilities based on varied data inputs, such as geophysical, and geotechnical measurements.
- Provide correlations that could allow for a reliable extension of the characteristics (e.g.: geotechnical parameters, lithology) here observed to areas where data availability might be scarcer, at a regional scale.
- Estimate how slope stability might be affected by temperature changes that could destabilize elements as gas hydrates and PF.
- Determine which areas are more likely to have their slope stability undermined by effects of sediment temperature changes as well the level of thermal increment necessary for such effects.
- Appraise the size of possible mass movements.

[1] Terrestrial pingos are conical ice-cored mounds, in average 10–40 m in high and 100 m or more in diameter, with their relief generally attributed to the expansion of ground ice. Submarine pingos, or PLFs, have sizes comparable to those of their largest terrestrial counterparts, with some PLFs protruding from nearly circular (1–2 km in diameter, 10- to 20-m in deep) bathymetric depressions, often called 'moats'. PLFs are also thought to result from gas hydrate decomposition within the sediment (Paull et al., 2007).

1.2. Geological setting

This section is generally based on the report by Blasco et al (2013), "2010 state of knowledge: Beaufort Sea seabed geohazards associated with offshore hydrocarbon development" – this is the source reference for the passages of this chapter where no citation is displayed. Other sources were also used (vide mentioned citations).

1.2.1. Study area; Geological summary

The Mackenzie Delta (**Figure 2**) is located in the central part of the Beaufort-Mackenzie structural basin and currently discharges onto a ca. 100 km wide continental shelf in the Beaufort Sea. During the last glacial maximum (LGM) the shelf was mostly emergent, although for short time intervals it was covered by the continental ice sheet, which reached as far as the present day shelf edge (Blasco et al., 2013). As the ice front retreated from the shelf edge, glaciomarine sediments formed a deposit that pinches out at the shelf edge and thickens down slope (Saint-Ange et al, 2014)

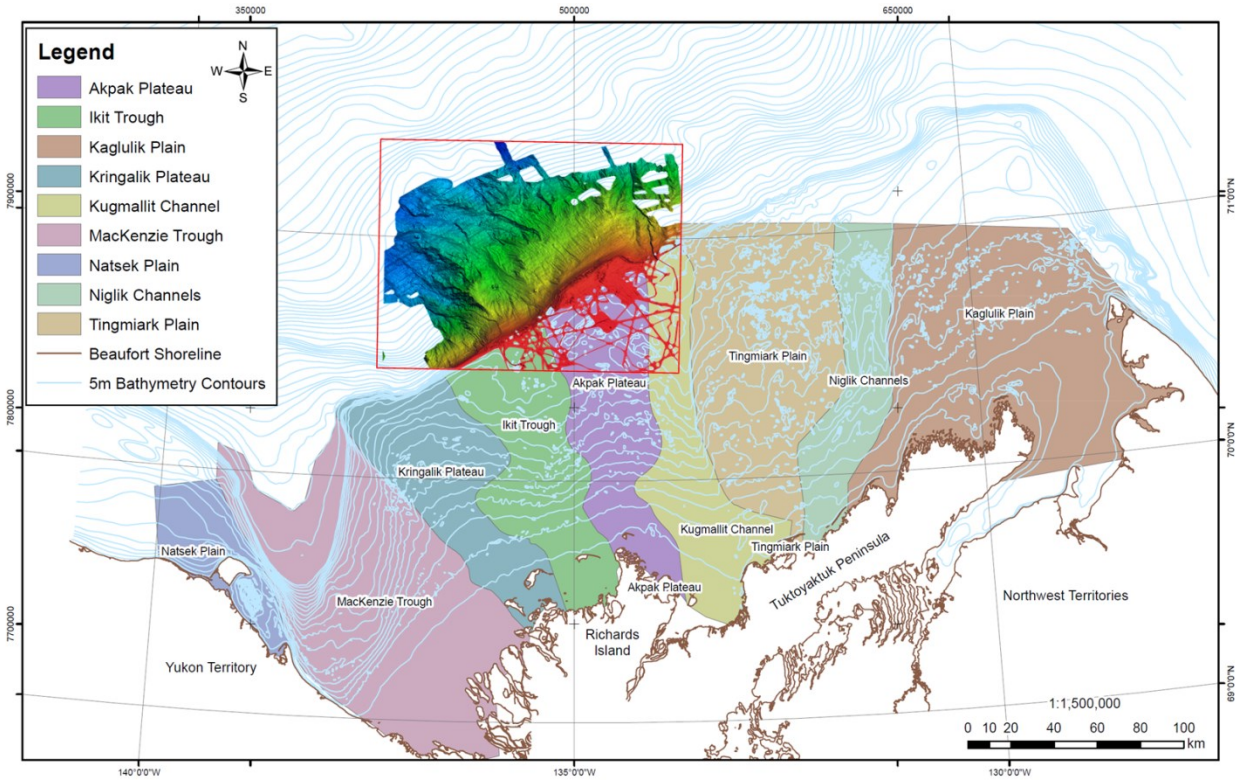

Figure 2: Beaufort Sea Physiographic subdivision (Blasco et al., 2013). The overlain bathymetry grid (within red square) shows the definite location of the area from which the data to be exposed and investigated in the subsequent parts of this thesis were retrieved.

The Mackenzie River has the largest sediment load of any river discharging into the Arctic Ocean, with ca. 127 × 10^6 Mt·a^{-1} (Carson et al., 1998), but relatively little sediment reaches the central shelf edge since the Coriolis force drives the sediment plume eastwards along the inner shelf (Blasco et al., 2012).

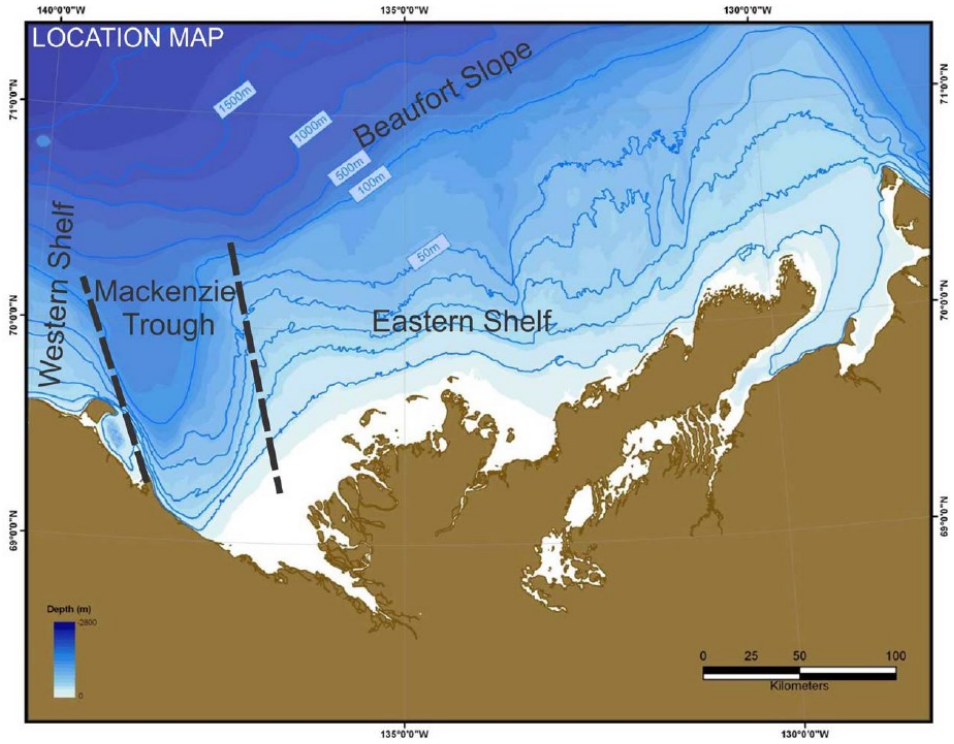

Figure 3: General locations of the Eastern Shelf, Mackenzie Through, Western Shelf and Beaufort Slope (Blasco et al., 2013).

The uppermost 100 m of the Beaufort Shelf sediments are no older than ≈27 k.a. (Hill et al., 1985), representing late Wisconsinan to Holocene deposits that propagate down slope (Blasco et al., 2013). At the uppermost Beaufort Slope, sedimentation rates during the late Holocene were estimated at about 1.4 m·ka^{-1}, stressing the post-deglaciation sediment input relevance of the Mackenzie River (Scott et al., 2009; Bringué and Rochon, 2012). This has been ground-truthed with a sediment core retrieved at 671 m depth in the Mackenzie Trough contains 8 m of soft mid- to late Holocene silty mud overlying laminated early Holocene to late Pleistocene muds (Schell et al., 2008). It has also been observed that at 1000 m water depth on the Beaufort Slope the mid- to late Holocene silty muds are 2 m thick and overlie relatively uniform clays with thin sandy intervals (Scott et al., 2009).

More than 700 m of ice-bearing sediments are present in the Beaufort Shelf, pinching out at ca. 100 m water depth, which corresponds to the present shelf edge. These ice-bearing sediments turn out to be impermeable, forming a barrier for fluid migration. Over time such fluids have migrated towards the edge of the permafrost (PF) and escaped to the seabed along the shelf break. Over 700 mud volcanoes

(Blasco et al., 2013) are found in the shelf edge area; the massive presence of such features is strongly suggested to be a result of concentrated fluid escaping at the permafrost edge.

Regarding earthquake activity, records suggest that it is rather low in the Beaufort region, being mostly associated with crustal response of uncompensated sediment load on the continental slope (Atkinson and Charlwood, 1988). Low magnitude seismicity (<4) is typical for this region, with few events in the past 100 years being reported to reach magnitudes above 5 (Lamontagne et al., 2008; Cassidy et al., 2010).

1.2.2. Stratigraphy and Structure

The seabed of the Beaufort Sea consists of two main areas, the Canadian Beaufort Shelf and the Beaufort Slope (**Figure 3**). The Canadian Beaufort Shelf is in turn subdivided into three main regions: the narrow Western Shelf adjacent to the Canada – US border, the Mackenzie Trough and the Eastern Shelf

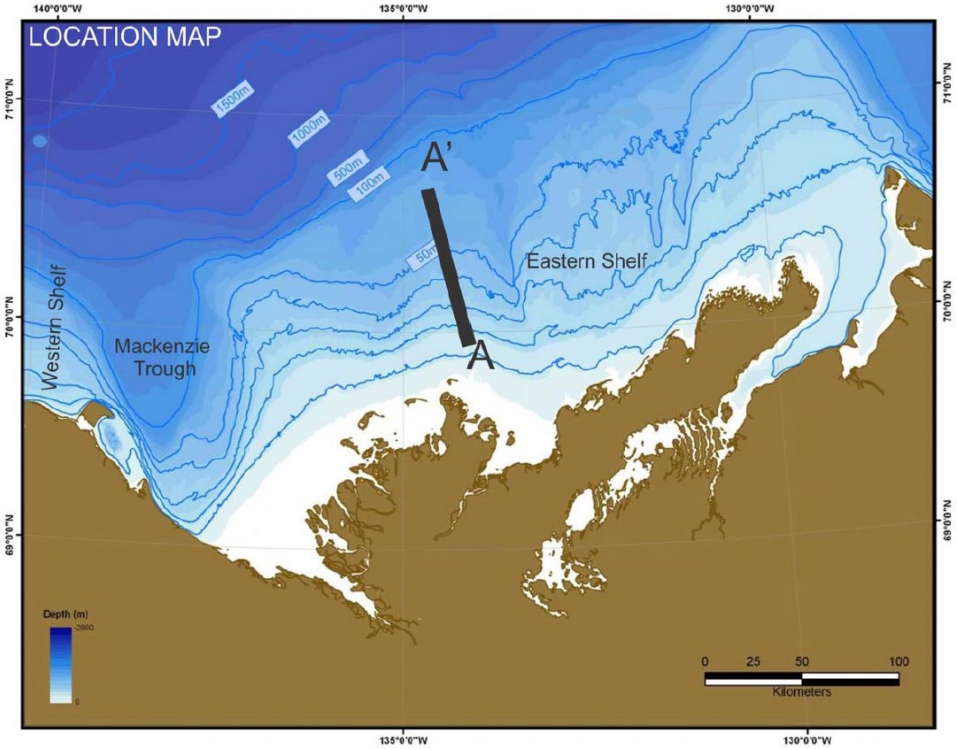

Figure 4: Beaufort Shelf with contour lines and cross section A-A' (Blasco et al., 2013).

The Eastern Beaufort Shelf is a broad shallow shelf that lies between the Mackenzie Trough and Amundsen Gulf. It is 350 km long and 150 km wide with an average slope gradient of 0.03 degrees. The Eastern Shelf is divided at ca. 133.5°W longitude where there is a change in surficial sediment from clay over the central shelf to sandier sediments on the eastern shelf. The upper 100 m of sediment on the

Eastern Beaufort Shelf has been sub-divided into five stratigraphic units: A; B; C; D; and E (**Figure 4** and **Figure 5**).

Unit A is the youngest, uppermost sedimentary unit of the Beaufort Shelf composed of a horizontal sequence of recent marine silt and clay deposited under low energy circumstances subsequent to the last sea level rise. Its thickness ranges from a few centimeters up to 20 m, with most of its sediment originated from the outflow of fine-grained material from the Mackenzie River. Unit A grades downward into Unit B, which consists of a transgressive sequence of littoral, deltaic, and lagoonal sand, silt and clay deposited in a transitional environment that existed during the last sea level rise. This unit unconformably overlies Unit C which is composed of silts, clays, sand, and gravel originating from former continental (glacial, fluvial, and eolian) and transitional environments (littoral, deltaic). Unit D, underlying Unit C comprises silt and clay up to 40 m thick representing a delta-margin or inner-shelf marine depositional environment. Unit E, a medium to fine grained sand of unknown thickness is below Unit D. Data indicates this unit was deposited during alternating sub-aerial delta plain and near-shore marine environments similar to Unit C.

The Western Shelf is less than 60 km wide by 80 km long, and slopes seaward at a gradient less than 0.05 degrees. The Western Beaufort Shelf has been divided into three units (**Figure 45**). The lowermost unit, Unit III, is a massive clay with exotic clasts of granitic and dolomitic composition. Unit II overlies Unit III and is composed of clay. A major erosional unconformity separates Unit II from the youngest unit, Unit I, composed of laminated silty clay that outcrops on the seabed in the outer shelf and reaches thicknesses up to 70 m on the shelf edge. Unit I is overlain by a discontinuous thin veneer of late-Wisconsinan / Holocene sediments.

The Mackenzie Trough is a paleo-valley which is partially infilled with more than 300 m of Quaternary sediments. The trough was excavated to its maximum depth by glacial erosion, leaving behind the glacial till - Unit MT5 (**Figure 6**). A thick sand sequence, Unit MT4, was deposited with the retreat of the glacier. Speculation exists, about a second ice advance into the trough, partially eroding Unit MT4. Unit MT3 represents a deformation structure caused by the ice or possibly a moraine deposit. The silty-clays of Unit MT2 are a result of subglacial drift, also deposited by the ice. Deglaciation was associated with Unit MT1 which was formed by the deposition of deltaic sediments, followed by transgression and deposition of marine clays which reach up to 125 m in thickness in the central Trough area.

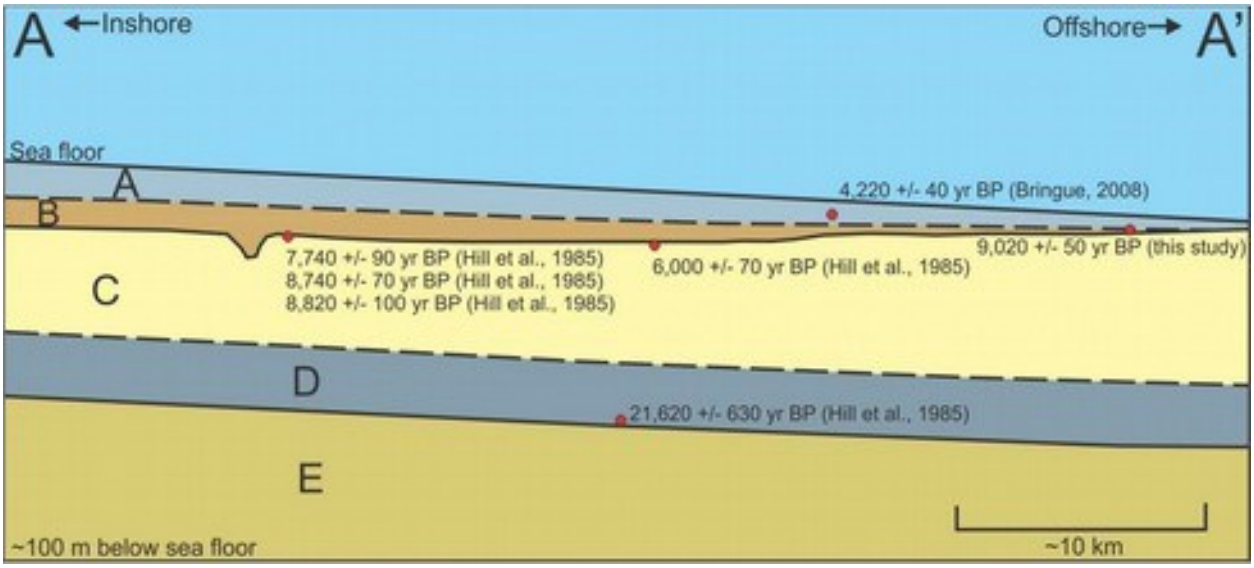

Figure 5: Schematic north-south cross section across the Eastern Beaufort Shelf showing the stratigraphic units of the upper 100 m of sediment (Blasco et al, 2013).

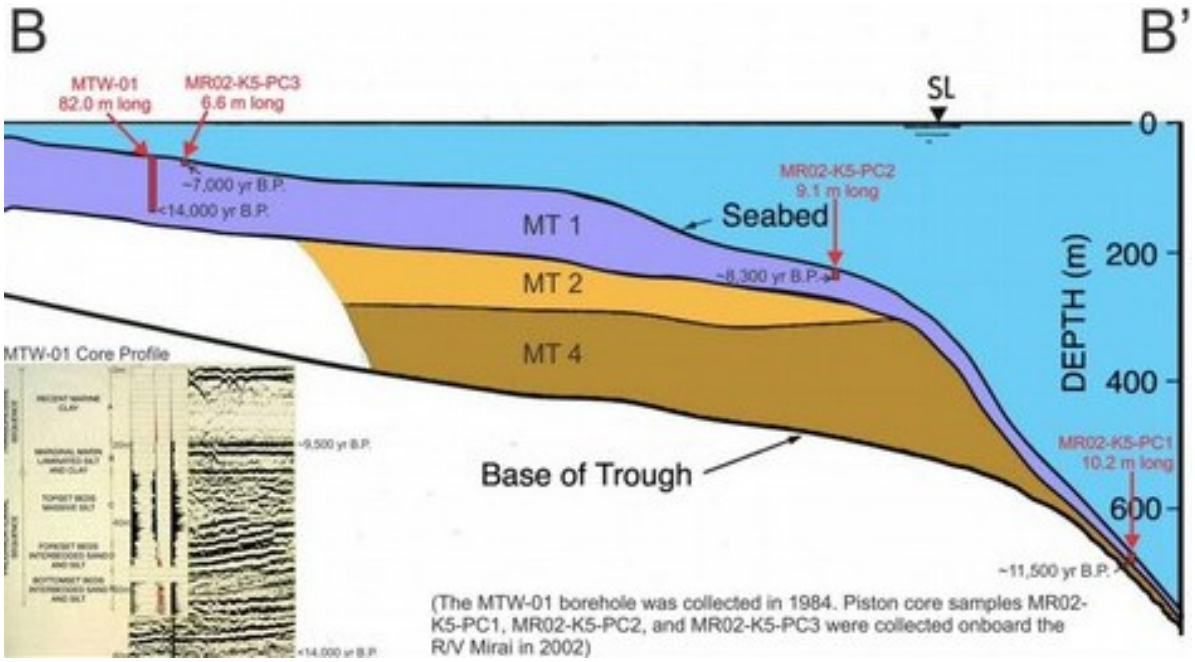

Figure 6: Schematics of the Mackenzie Trough showing seismostratigraphic units infilling the Trough (Blasco et al., 2013).

The Beaufort Shelf was sub-aerially exposed and accumulated sand (Unit C; **Figure 5**) as a glacial outwash plain during the LGM. Simultaneously, the Beaufort Slope was a near-shore to marine environment gathering sediment from periglacial sources as well as marine sedimentation. The lower sea level during LGM would have created a dynamic environment with a high sedimentation rate on the slope, perhaps contributing to an increase in slope failures and deposition of mass transport deposits. Marine transgression after the glacial maximum then provided marine sedimentation to the shelf. These

two different depositional environments have led to different but likely time-equivalent sediment deposits on the slope and shelf.

1.2.3.Geohazards

Seabed mapping of the central Beaufort Slope area using high-resolution multibeam sonar (MB) and sub-bottom profiler (SBP) provides an insight into processes active on the seabed over the last 10,000 years. These data indicate that both stable and unstable areas of the seabed exist down slope.

Sub bottom profile data indicate thick sequences of stratified sediments, in excess of 70 m exist down slope. The lack of disturbance in this sequence indicates sediments in these areas have been stable for a long time, possibly several thousand years.

Conversely, an area of submarine slides has been identified in which sediment was dislodged to form scars approximately 25 km wide (E-W) and 20 km long (N-S). The age of this slumping activity is unknown. Submarine slides are considered geohazards because such events can damage engineering structures such as drilling systems and pipelines placed on or below the seabed.

1.2.3.1. Gas Vents and Oil Seeps

Caused by the venting of fluids or gases from the sub-surface into the water column, pockmarks are roughly circular-shaped depressions on the seafloor. Pockmarks have been found to be abundant in the Kugmallit Channel, in the eastern Mackenzie Trough physiographic region and at the edge of the Beaufort Shelf. Gas in the water column has been detected in relation to pockmarks. Oil was observed in seafloor sediments at the central shelf. Gas vents and oil seeps allude to unstable conditions below the seabed, constituting a possible geohazard, other than an indicator for deeper reservoirs or gas hydrates presence.

1.2.3.2. Mud Diapirism (Garry Knolls Area)

Mud diapirs seem to be an important variety of instability features and are widespread throughout the area. A complex sub-seafloor reflector scheme is associated with numerous instability features at the southeast margin of the Gary Knolls area (**Figure 46**). These features are found on the margins of subsiding basins or over domed structures. Diapirs in the region are commonly asymmetric and associated with growth fault zones; they are also distributed in a narrow northwest-southeast trend along the Gary Knolls area. They apparently have developed in cycles of intrusion, extrusion, and

subsidence with sediment and mud flow fillings. Their origin seems related to deep and mobile underlying strata, boosted by gas migrating along faulted conduits from depth. (**Figure 47** and **Figure 48**)

1.2.3.3. Subsea Shallow Gas

The presence of subseafloor shallow gas is observed in many areas of the Beaufort Sea. Regional geophysical surveys identified their presence throughout the shelf as discontinuous and localized volumes within sediments from the seabed down to over 500 m depth. From the geohazard perspective, subseafloor shallow gas at depth represents a risk since overpressure in such deposits can lead, for instance, to well-bore instability during drilling activities (**Figure 49**).

1.2.3.4. Subsea Permafrost

PF (in sediments below 0°C), is pervasive in the Beaufort Shelf (Pelletier, 1987). It has formed during low-stand sea level episodes, in which parts of the shelf formed an emerged coastal plain subject to very cold periglacial temperatures. Concerning geohazards, the presence or absence of ice bonding is very significant. With ice bonding the sediment compressive and shear strength are intensified, though the sediment porosity and permeability are diminished.

Since PF-bearing sediment has its pore space and fissures at least partially filled by ice (which also has considerably higher shear strength), ice veins might support part of the overburden load, keeping such load from being fully absorbed by the sediment itself (not effectively compressing and consolidating the sediment as the ice framework sustains part of the pressure). This arrangement can result in under-consolidated sediment. Hence, with PF thawing the sediment can undergo strain deformation, changes in pore water pressure and strength deterioration (**Figure 48**, **Figure 50**, **Figure 51** and **Figure 52**).

Ice-bearing sediments in the shallow shelf (top 100 m of sediment) are presented as hummocky PF, stratigraphically controlled and marginally or partially ice-bonded, being discontinuously distributed in the region (Blasco et al., 2013). Deep shelf ice-bearing permafrost (IBPF) stretches with a SW-NE orientation. A notable westward thickness reduction and an eastward elongation of the IBPF is guided by the distribution of sand layers.

Among the important aspects of better understanding the arrangement and behavior of ice bonded PF in the Beaufort-Mackenzie region are: better constraining seismic reflection reading, defining the stability zone of gas hydrates (GH), and refining heat flow and thermal history models. The thickness of the hydrate stability zone tendentially increases with the thickening of the PF interval.

Seismoacoustically, the PF is a relatively high velocity interval above water-saturated sediment (interface characterized by decrease in impedance).

1.2.3.5. Subsea Gas Hydrate

Natural gas hydrates (GH) are solids formed from water and gas that resemble packed snow or ice, in which the gas molecules are "caged" within a crystalline structure, composed of water molecules. They were reckoned at the southern Beaufort Sea through interpretation of well logs and drilling response (Weaver and Stewart, 1982; Smith and Judge, 1993; Osadetz and Chen, 2010). Also known as gas clathrates, they form in low temperature and high pressure conditions, provided adequate gas supply, pore water and porosity conditions. The presence of IBPF (generally from the shore to ca. 100 m water depth), regulates the sediment temperature conditions for PF gas hydrate occurrence. Given the differences in thermal conditions at the Beaufort Sea, gas hydrates are predicted to be found in roughly two varieties (**Figure 7**). One is the intra-permafrost gas hydrate, which forms at temperatures below 0°C and possibly comprises pore ice. The other one is the sub-permafrost gas hydrate, with formation temperatures over 0°C. Additionally, gas hydrates are also assumed beneath the slope and further offshore since bottom water temperatures are near 0°C and water depths are above ≈250 m.

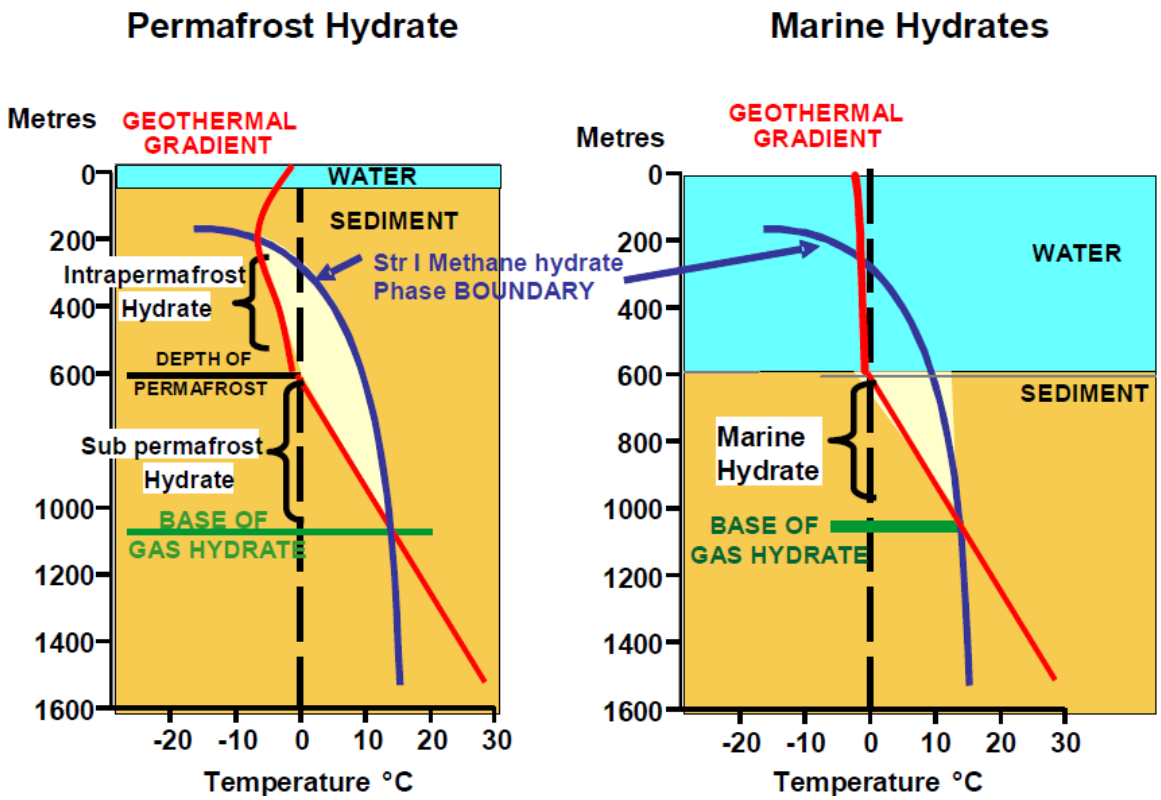

Figure 7: Diagrams plotting permafrost and marine gas hydrate pressure and temperature stability conditions in the Beaufort Sea (Blasco et al., 2013).

When gas hydrates are found in the sediment, its strength and consolidation properties tend to be analogous to those of ice bonded PF. In addition, similarly to sediments with considerable ice content, the dissociation or thawing of gas-hydrates in the sediment (if at sufficient pore space concentrations) should provoke a considerable reduction in strength and strain/consolidation. Yet, natural phenomena and anthropogenic activities (e.g.: drilling) might also disrupt gas-hydrate-bearing sediments, possibly promoting the liberation of important quantities of free gas (up to 160 times their initial volume at standard atmospheric conditions) (Blasco et al., 2013).

During the Pleistocene sea level was ca. 120 m below present levels (Fairbanks, 1989), thus a large fraction the Beaufort Shelf was an emergent coastal plain. Parts of the shelf were then episodically ice covered, but this area was supposedly too arid for the growth of glaciers. As a result, PF formed due to the exposure to cold temperatures and was eventually submerged by marine transgressions. The thickness of the PF is estimated to be up to 700 m based on the long periods of exposure to such cold temperatures (Fortin and Blasco, 1990), which implies the base of the gas hydrate stability zone (GHSZ) to be deeper than 1200 m. Moreover, Weaver and Stewart (1982) conclude that the geothermal conditions are suitable for gas hydrate stability between 225 m and 1500 m depth). Such estimates essentially consider the sediment depth that corresponds to geothermal conditions that allow for the formation of intra-PF and sub-PF gas hydrate (**Figure 53**), though the geothermal conditions are not a sufficient parameter (i.e.: the presence of free gas is another crucial factor).

Well log interpretations indicate gas hydrates mainly in sands with possible intervals of over pressure. Regionally, gas hydrate presence studies are in some cases difficult due to data quality issues, generally expressing that up to 80% of 93 exploration wells drilled on the shelf suggest sub PF gas hydrate occurrences (Smith and Judge, 1995; Osadetz and Chen, 2010).

Marine transgression could be a trigger for gas hydrate dissociation in the Beaufort Shelf (Paull et al, 2007; 2011). Post transgression warming might also have caused PF and/or gas hydrate dissociation, as hinted by shallow geologic studies geothermal modeling and the geochemistry of sediment pore waters. This hydrate dissociation could have induced upward migration fluids and sediments, in turn inducing the formation of pingo-like features (PLFs) on the Beaufort Shelf

Gas hydrate occurrence is plausible at water depths greater than ≈250 m, since the annual bottom temperatures are around 0°C at these depths (**Figure 7**). In 2009 a cruise gathered data indicating possible GH presence on the Beaufort Slope (Campbell, 2011). Paull et al., (2011) observed methane

degassing upon recovery of several PLF core samples (between ≈250 and 400 m water depth). Such cores from the crest of the PLFs exhibited a “moussy texture”, typical of gas charged and previously gas hydrate bearing cores. Isotopic analysis of the gas showed the methane in the samples to be a product of microbial CO2 reduction, including a shift on co-isotopic $\delta^{13}C$ vs. $\delta^{13}D$ plot, with signals normally ascribed as being gases from mixed biogenic and thermogenic sources, though C3 and higher hydrocarbons were not detected.

1.2.3.6. Geothermal regime

The Geothermal Gradients of the Beaufort MacKenzie Basin is generally that of typical sedimentary basin, with values of about 25-30°C/km (green pattern in **Figure 54**). Comparatively higher sedimentation rates (>1 km/M.y.) at the outer shelf during the Pliocene-Pleistocene probably resulted in the observed lower heat flow and geothermal gradients in this area (<25°C/km). At the SE basin margin (parallel to the Eskimo Lakes Fault Zone, on the Tuktoyaktuk Peninsula) comparably higher geothermal gradients (30-50°C/km) are measured, possibly related to the heat contribution from thicker, intact continental crust and subsurface fluid flow. The SE basin also has a thin sedimentary cover, thus magnifying errors of gradient calculation. The central part of the basin (along Tarsiut-Amauligak Fault Zone in the Beaufort Fold Belt and near the Taglu Fault Zone on Richards Island) shows higher gradients (>30°C/km), likely stemming from heat advection by upwelling fluids along fault systems. Chen et al. (2008) demonstrated a tendency for temperature increase towards major faults in the Basin.

1.2.3.7. Overpressure

Overpressure is commonly associated with undercompacted sediments in the Beaufort-Mackenzie Basin and is here defined as the fluid pressure that exceeds hydrostatic pressure. Such high pressure conditions could represent a geohazard. Multi-parameter data (well log, mud weight, pressure test, and temperature data) were used to identify the depth to top of overpressure at well locations throughout the Beaufort-MacKenzie region. The depth of the overpressure was mapped through the analysis of drill wells, showing among other things that overpressure is associated with structural highs.

The compaction of sediments buried in normal conditions commonly allows the material to preserve enough pore interconnectivity to permit the expulsion of formation fluids and maintenance of hydrostatic pore fluid pressure (a typical hydrostatic gradient is ca. 10 kPa/m). Usually, a lithostatic gradient of about 23 kPa/m results from the pressure of a saturated sediment column. Rapid sediment burial can cut off deep fluids from the above fluid column and prevent deep fluid expulsion due to low

permeability “seals”. Since the confined pore fluids carry part of the weight of the sediment column above, the conditions for surges in pore fluid pressure under these seals arise. The fluid pressure might even get higher than the lithostatic pressure, consequently provoking rock failure and breach of seals.

The analysis of ca 250 wells (105 of which pierced the overpressure zone and the remaining ones show consistency with normal hydrostatic conditions) yielded the contour map of the depth to top of overpressure shown in (**Figure 55**). The represented values give the depth to primary overpressure, which coincides with a considerable change into high pressures linked to undercompacted sediments.

A correlation has been found between overpressure and thick undercompacted deltaic deposits (Upper Cretaceous-Cenozoic, limited to offshore areas and to the Central Delta region (Issler et al, 2011). The top of overpressure is associated with Paleocene strata in the south, progressively crossing younger strata to the north. Deep overpressures are related to normal faulting (e.g., Tarsiut-Amauligak Fault Zone) while shallow overpressures seem to correspond to structural highs and exhumed and deformed strata of the Beaufort Fold Belt in the southwest. Faults seem to work as horizontal barriers that segment the pressure distribution and there is evidence for vertical fluid migration in areas with extensive normal faulting (Chen et al., 2010).

1.2.3.8. Earthquakes and Tsunamis

The seismically active zone of The Beaufort Sea shows considerable earthquake occurrence spanning a ca. 250 km wide area. In average one earthquake with a magnitude ≈4 is expected per year (in 1920 a magnitude 6.5 earthquake was registered) (Blasco et al., 2013). The origin of seismicity in this area is unknown due to data availability limitations preventing modern analysis. Seismicity in the Beaufort-Mackenzie area has been monitored with distant observation stations, which intrinsically restrains the capacity to determine the location and depth of historical earthquakes. The Richardson Mountains seismic zone (south of the Beaufort Sea) has a relatively high seismicity, three magnitude 6 earthquakes detected in the past 60 years. The Eskimo Lakes fault zone and the front of the modern Mackenzie Delta are other earthquake source zones.

Tsunamis are high amplitude ocean waves that impact the shelf and coastal zone, normally resulting from earthquakes or submarine mass movements. No evidence of tsunamis is found in the recent geological record or within traditional knowledge. Both earthquakes and tsunamis are considered geohazards since they can severely damage engineering structures (**Figure 56**).

1.2.3.9. Faults

Regions deeper than 100 m below seabed have documentation showing faulting (e.g.: Fortin & Blasco, 1990). Faults in the area are generally characterized as belonging to two main groups: high angle normal fault systems and normal listric 'growth' fault systems. In the Eastern part of the Beaufort Sea high angle normal faults are correlated with the offshore extension of the Eskimo Lakes Fault Zone (**Figure 56**).

Faults in the region trend in a N-NE direction, with the downthrown block generally to the west. Vertical displacements on the order of 50-100 msec (50-100 m based on a sound velocity of 2000 m/sec) were documented at the Late Miocene unconformity (Fortin & Blasco, 1990). In the Issungnak-Amauligak area of the Beaufort Sea inner shelf normal listric “growth“ faults were interpreted from different data. This fault system offsets Late Eocene to Late Miocene strata and foreshadows the Late Miocene unconformity. Moving west, the down-to-the-basin trend in faulting gives way to a more complex Wrench-Related fault zone (Fortin & Blasco, 1990). Strata displacement within unconsolidated sediments was observed in different areas with considerable sequences of laminated sediment (**Figure 57** and **Figure 58**).

2. Materials and Methods

This section describes techniques applied during the expeditions CCGS Sir Wilfrid Laurier 2013, ARA04C (IBRV Araon, 2013).and ARA05C. The materials and methods here presented are mainly based on the ARA04C Cruise Report (Jin & Riedel, 2014), nevertheless other sources were also used (vide citations).

2.1. Sub-bottom profiler (SBP) survey

Sub-bottom profilers are used to identify and characterize layers of sediment under the seafloor. Its operation principle is based on a sound source that sends a pulse toward the seafloor. Part of the energy of this pulse is reflected on the seafloor, while some of it penetrates the sediments. The penetrating fraction is both reflected and refracted as it goes through different layers. The returning signals are then detected by hydrophones. Subsurface images from SBPs represent the underlying sedimentary structure.

The conventional acoustic signal frequency used by this equipment is 3.5 KHz and, ideally, up to 10 cm thick layers could be detected depending on the sediment structure. The average vertical resolution is ca. 0.5 m. In the Canadian Beaufort Sea surveyed area, subsurface structures are frequently related to PF and gas presence.

In the ARA04C expedition the used profiling system was the SBP120 (**Figure 59**; **Table 4**), an extension of the EM122 Multibeam echosounder system which has a broadband receiving hydrophone system. The adaptation to the multibeam which allows for sub-bottom profiling capability is the addition of a low frequency transmitting transducer, electronic cabinets and operator stations. The SBP120 has a frequency range between 2.5 and 7 KHz, and a beam width of 12 degrees with 24 transducers (footprint of 20% of the water depth). It features roll and pitch electronic stabilization and can be steered to adjust to bottom slope. Due to synchronization with the multibeam system these two systems can operate simultaneously. The SBP120 produces data in the TOPAS .raw format.

More than 3000 line-kilometers were surveyed with the SBP during the ARA04C cruise and co-located with multibeam and backscatter data (**Figure 60**). These data are very helpful for the study of sub-seafloor PF and provide insights into sediment dynamics at the continental slope.

During the ARA04C cruise the work of SBP data acquisition had the involvement of Michael Riedel (Geological Survey of Canada, GSC), Jong Kuk Hong (Korea Polar Research Institute, KOPRI), Kim Conway (GSC), Dong Seob Shin (KOPRI), Sookwan Kim (KOPRI), Hyoung-Jun Kim (KOPRI), Hakkyum Choi (KOPRI), Young-Gyun Kim (KOPRI), Nari Seo (KOPRI), Malaika Ulmi (GSC),Ren Hyun Seung Kim (GSC), Eunji

Byun(SNU), and Young Joo Lee (Korea Institute of Geoscience and Mineral Resources, KIGMR), being ultimately processed and provided by the KOPRI.

2.2. Multibeam survey

Multibeam echo sounders gather bathymetric information using a swath perpendicular to the ship track, electronically forming a series of beams in the transducer and then recording the returning signal after it interacts with the sediment surface. The bathymetric contours are thus measured in discrete angular increments or sectors across the swath (Hughes-Clarke et al., 1996).

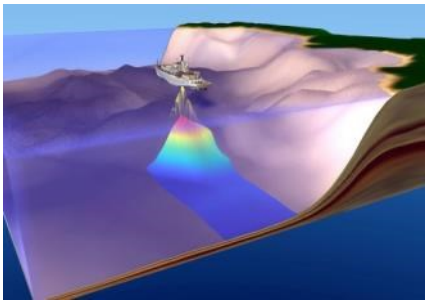

The multibeam system consists of a hull-mounted transmit and receive transducer, transceiver unit, and operator station (**Figure 61**, **Table5**)

During the cruise ARA04C, swath bathymetry and backscatter data were acquired with the EM122 multibeam system, which has a wide beam angle (-70 - 70 degrees). Sound velocity profiles were collected from CTD castings and then applied in the calculations of the hydroacoustic measurements. The bathymetry data were processed onboard with the CARIS software. Malfunction of the supporting navigation system (Seapath) during the survey caused recording errors, which would generally disrupt the water depth calculation, resulting for instance in data gaps.

During the ARA04C cruise the work of Multibeam data acquisition had the involvement of Michael Riedel (GSC), Jong Kuk Hong (KOPRI), Kim Conway (GSC), Dong Seob Shin (KOPRI), Sookwan Kim (KOPRI), Hyoung-Jun Kim (KOPRI), Hakkyum Choi (KOPRI), Young-Gyun Kim (KOPRI), Nari Seo (KOPRI), Malaika Ulmi (GSC),Ren Hyun Seung Kim (GSC) and Eunji Byun (SNU).

2.3. In situ temperature and Heat flow

Heat flow distribution studies help to better understand the thermodynamics of the inner Earth and the surficial process within sediments (e.g., Von Herzen and Uyeda, 1963). The comprehension of processes like fluid expulsion from sediments or the detection of sub-seafloor ice is aided by the knowledge of the local heat flow distribution. Measuring geothermal gradients is also a common approach to evaluate the gas hydrate stability zone (e.g. Yamano et al., 1982; Kim et al., 2010). Heat flow measurements have been carried out at several stations during the ARA04C expedition (**Figure 62**), with the intention of assessing the extent of marine PF.

The heat probe used during the ARA04C was an Ewing-type, employed to measure in-situ thermal conductivity and geothermal gradients by single penetration of the probe into the sediments. In this expedition the use of this method was complicated due to extremely cold temperatures, sea ice, and particularly competent sediments.

During the cruise ARA04C, the Heat Flow data acquisition had the involvement of Young-Gyun Kim (KOPRI) and Eunji Byun (SNU), and during the 2013 CCGS Sir Wilfrid Laurier cruise of Greg Middleton (GSC), Timo Fleischmann (MARUM), Kira Aβhoff (MARUM) Scott Dallimore (GSC) and Charlie Paull (MBARI).

Equipment description:

Two main physical properties define the heat flow measurements: geothermal gradient and thermal conductivity of the sediments. The heat probe is basically composed of a frame (weight and barrel) and electrical parts (sensors, data logger, and thermistors). A data logger containing different sensor is usually attached to the top-weight, and thermistors are fixed to the barrel below the top-weight.

Cruise ARA04C:

(Jin & Riedel, 2014)

The Ewing-type heat probe is capable of measuring the in-situ geothermal gradient and thermal conductivity **(Figure 63**, **Table 6**). Active (heat-generating)and passive thermistors are attached to the barrel, adding up to nine thermistor channels in total - three heating channels and a maximum six passive thermistors. In-situ thermal conductivity is determined through the so-called transient method, being based on the speed of heat dissipation (Von Herzen and Maxwell, 1959; Carslaw and Jaeger, 1959). Shock and tilt sensors evaluate the tool-conditions to generate heat after penetration of the probe. Accurate positioning of the probe is done with a pinger and transponder.

The standard steps for the measurement of marine heat flow with the Ewing-type probe are: 1) deployment, 2) 10 minute standby at tens of meters above seafloor, 3) 20 minute standby after sediment penetration, 4) withdrawal from sediments and standby for 5 minutes above seafloor, 5) second penetration and standby for 15 minutes - to check measurement reliability - , 6) final extraction of probe from the sediment and 7) data retrieval from the data logger.

Calibration functions are then used to convert the thermistor data into temperature values and a data-quality control is done through checking changes of tension, tilt and general data trends.

Cruise CCGS Sir Wilfrid Laurier 2013:

(Riedel et al., 2014)

Miniaturized Temperature Data Loggers (MTLs) were the equipment of choice for this expedition, attached with outriggers to the outside of a gravity core sampler. The loggers can measure temperatures between -4.5°C and 60°C, with peak resolution of 1 mK (Pfender and Villinger, 2002). The sampling was done with a rate of one measurement per second and the maximum logging time was 18 hours. Calibration took place in August 2013, at the University Bremen. Even though the tool configuration varied during the expedition, all measurements obtained after station #56 were obtained with this geometry: 5 outriggers and loggers, located at 20 cm, 45 cm, 70 cm, 120 cm, and 170 cm measured from the bottom of the core barrel (**Figure 8**, **Figure 9**, **Figure 10**).

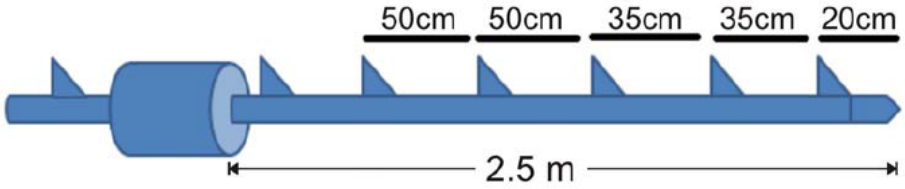

Figure 8: Diagram of gravity core sampler and intervals in which the Miniaturized Temperature data Loggers (MTLs) were placed (Riedel et al., 2014).

Figure 9: Photo on the deck of the ARAON after recovery of (partially covered by sediment) gravity core with MTLs attached (Riedel et al, 2014).

The measurement procedure consists of: 1) core penetration into the sediment, 2) keeping the equipment in the sediment for about 7 minutes to allow for thermal equilibrium and 3) withdrawal from sediments.

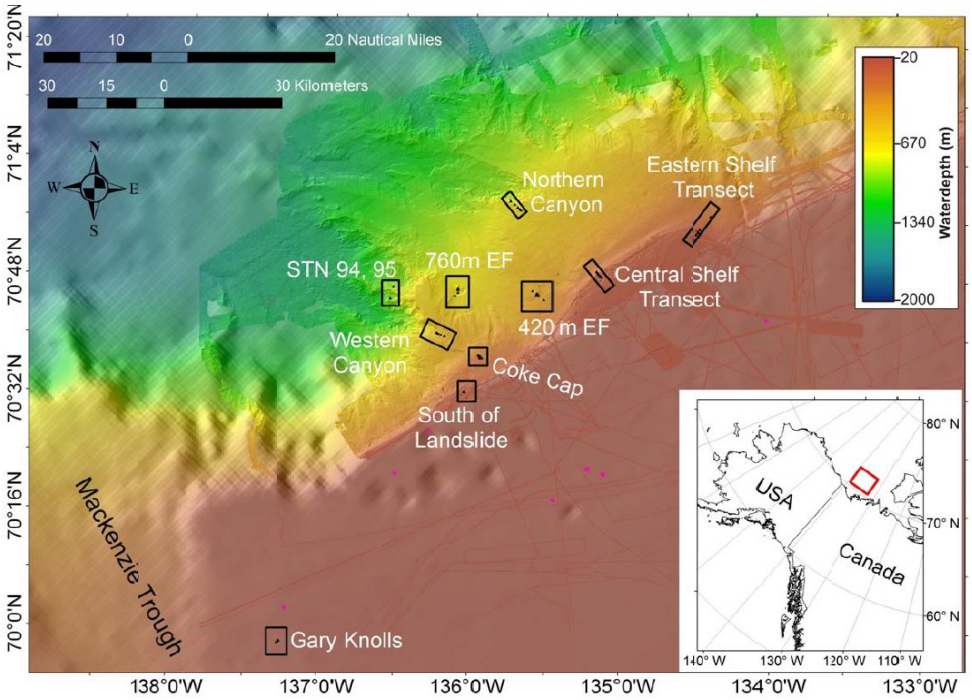

Figure 10: Research area of the CCGS Sir Wilfrid Laurier 2013 expedition, with sub-regions where temperatures were measured (Riedel et al, 2014).

2.4. Sediment coring

The goal of the marine geology program during the ARA04C was to collect sediment cores from the selected areas in order to provide a better understanding of the local stratigraphy, glacial history, geohazards and gas hydrate occurrence (**Figure 64**). This program was composed of the following sections: 1) acquisition of sediment cores for studying late Quaternary glacial history and paleoceanographic changes from the northern Alaskan continental margin; 2) sediment coring, SBP and multibeam data collection based on IODP proposal 753 for drilling in the Beaufort Sea; and 3) retrieval of sediment cores from the selected core sites searching for evidence of gas hydrates.

The acoustic-derived characterization of the first 100 m of sediments is done with the SBP, which is then employed in studying aspects of past depositional environments. The hydroacoustic survey methods were aimed at: a) aiding the interpretation of acoustic facies relative to different sedimentary environments, b) identifying patterns of acoustic stratigraphy for lateral correlation, with the aid of the sediment cores, c) defining coring stations, and d) complementing high-resolution surveys of the uppermost portions of seismic profiles.

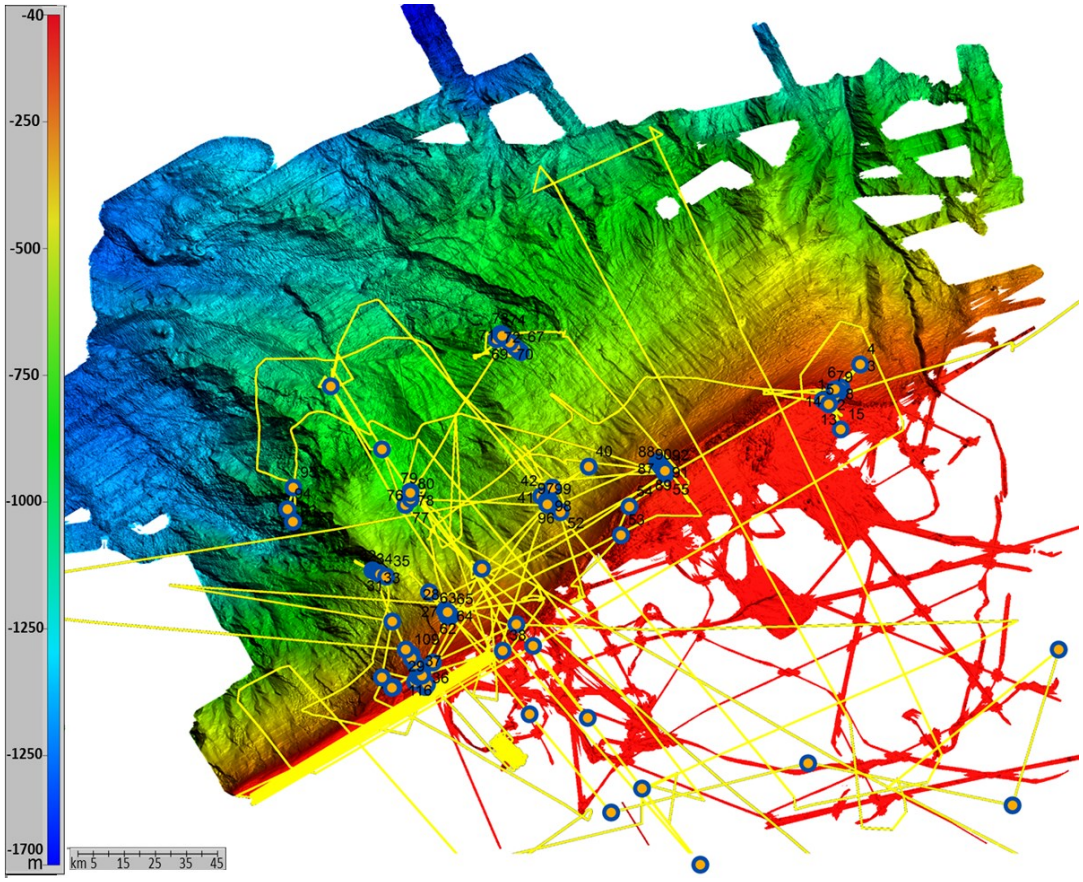

Figure 11: Map including ship tracks (yellow line) and all sampling locations (orange-blue dots).

2.4.1.Gravity corer

The used gravity corer was 10 cm in diameter, with a 1.5 ton headstand and had 3 m long barrels, capable of configurations conceding the acquisition of up to 9 m long cores. The retrieved cores were segmented into 1.5 m long sections and, after an overnight temperature equilibration, scanned with a GeoTek multi-sensor core logger. Pore water was collected with Rhizon samplers at 20 cm intervals.

During cruise ARA04C the sediment coring had the participation of Seung-Il Nam (KOPRI), Kim Conway (GSC), So Young Kim (KOPRI), Borom Lee (KOPRI), Yeongsam Sim (KOPRI), Michael Schreck (KOPRI) Anna Hedwig Quantmann-Hense (Alfred Wegner Institute, AWI), Changhoon Han, Young Joo Lee (KIGMR) and Eunji Byun (SNU). During cruise 2013 CCGS Sir Wilfrid Laurier it was done by Greg Middleton (GSC), Timo Fleischmann (MARUM), Kira Aβhoff (MARUM) Scott Dallimore (GSC) and Charlie Paull (MBARI).

2.5. Determination of sediment physical properties with multi-sensor core logging

Initial core characterization is given by the measurement of physical properties, which can be done with high vertical resolution, making possible the definition and interpretation of stratigraphic patterns related to different aspects like the encountered lithologies or other properties derived from sediment color or XRF scanning. The association of these logging methods with high-resolution echo sounder profiles results in a powerful strategy for core correlation.

A high resolution Multi Sensor Core Logger (MSCL), manufactured by the company GEOTEK (UK), was used for measurements of density, sonic velocity, magnetic susceptibility and electrical resistivity on the obtained sediment cores. The acquisition of the MSCL data was a brought upon by Michael Schreck (KOPRI) and Anna Hedwig Quatmann-Hense (AWI).

2.5.1. Method and data acquisition

Gravity cores were measured in 150 cm long sections. Onboard the parameters measurements were: core geometry (diameter), temperature, P-wave travel time, gamma-ray attenuation, magnetic susceptibility and electrical conduction at 10 mm intervals using a standard MSCL track (GEOTEK Ltd., UK, Ser. No. 25; detailed equipment description at the "Multi-Sensor Core Logging" manual, found at the website www.geotek.co.uk). The obtained values served as input in calculating secondary physical properties like bulk density (WBD in g/cm^3), P-wave velocity (V_p in m/s), volume-specific magnetic susceptibility (MS in 10^{-6} SI) and non-contact electrical resistivity (NCR in Ωm).

2.5.2. Geometry

The core diameter is defined by the distance between the faces of the Vp-transducers by using rectilinear displacement transducers coupled with the V_p transducers. Core thickness is measured as the deviation from a reference similar in length as the core diameter. The median wall thickness of KOPRI liners was determined empirically as 2.8 mm (Kang, 2012) resulting in a total wall thickness of 5.6 mm. The reference (industrial) outside diameter of the KOPRI GC liner is 115 mm. The calibration of the core diameter was done with three plastic cylinders logging: 110 mm, 114.95 mm, and 120.02 mm. With the GEOTEK Utility Software A/D readings from the test panel were obtained for each of these cylinders and traced as function of the deviation from the reference (-5 mm, -0.05 mm, 5.02 mm). The resulting linear

regression is put into the logger settings (www.geotek.co.uk) in order to log core-thickness deviation in mm and saved in the raw-data.

2.5.3.Density

The calculation of the Wet Bulk Density (WBD) was derived from the attenuation of gamma-ray beam transmission from a radioactive source (^{137}Cs) and a collimator was used to focus the radiation through the core-center into a gamma detector (**Table 7**). GEOTEK-MSCL software was used (www.geotek.co.uk) to determine the density of gamma counts, using a 2^{nd} order polynomial function to describe the relationship between the natural logarithm of gamma counts per second and the product of density and thickness of the measured material. For calibration the three constants of the equation are determined empirically for each day by logging a standard core consisting of different proportions of aluminum and water as described in Best and Gunn (1999).

2.5.4.Porosity

Fractional Porosity (FP) is defined as the ratio of the total volume over the volume of the pores filled with water. FP determined by MSCL-logging is not an independent data acquisition parameter but can be calculated from the WBD as follows: $FP = (\rho_g - WBD) / (\rho_g - \rho_w)$ where ρg = grain density (2.7 g/cm^3) ρ_w = pore-water density (1.03 g/cm^3). This approach assumes that grain density and pore-water density are constant.

2.5.5.Temperature

Core-surface temperature was used for measuring the temperature (T), with known temperature water samples (between 17°C to 37°C) for calibration. Since some sensors are sensitive to this variable, temperature is measured to monitor equilibration between core-temperature with laboratory temperature.

2.5.6.Measurement procedure

The measurement steps of the sediment physical properties can be described in the following steps:

1. Collection of Multi Sensor Core Logger raw-data from cores with GEOTEK software.

2. Initial processing of sediment core data with GEOTEK software, including calculation of core thickness, V_p, and WBD. MS and NRC sensor measurements were kept in raw-data state (10^{-5} SI and mV, respectively).

3. Further processing of core data with the *Kaleidagraph*™ software. This step involves data quality control on calibration sections logged on top and below the bottom of the core (250 mm liner filled with water) and data editing, also excluding the liner caps from the depth scale and data resulting from liner caps on V_p, WBD and NCR. Finally MS is converted into volume-specific MS, and the WBD details used to calculate the fractional porosity.

4. Plotting of data using the *Kaleidagraph*™ and *Adobe Illustrator*™ software.

2.6. Cone Penetration Testing (CPT)

(From Melling, 2013)

Essentially, the CPT probe is a free-falling instrument aimed at penetrating the seabed and measuring the in situ strength and pore pressure of the uppermost meters of sediment. The model used during the CCGS Sir Wilfrid Laurier, Leg 3, was designed and manufactured in Germany by the group *Marine Geotechnics* at the University of Bremen (https://www.marum.de/en/In_situ_Messinstrumente.html). The main parameters extrapolated from CPT measurements are commonly derived as follows: the total force acting on the cone, Q_c, divided by the projected area of the cone, A_c, produces the cone resistance, q_c. The total force acting on the friction sleeve, F_s, divided by the surface area of the friction sleeve, A_s, produces the sleeve friction, f_s.

The equipment is composed of a 20 cm cylindrical pressure housing ca. 1 m long and a lance that can be assembled with different lengths (between 0.5 and 6.5 m) (**Figure 12**). The different configurations are naturally reflected on the weight of the probe, varying between 40 and 170 kg. The power supply is battery-based and a data storage unit is built-in. The deployment of the probe was done by a 5/16 inch (≈8 mm) non-conducting wire with the DFO (Canadian Department of fisheries and Oceans, Institute of Ocean Sciences) Hydrowinch. CPT deployments were in practice a night-time activity and the operations were performed with a minimum of two scientific staff personnel and the assistance of a night watch crew member. When using a shorter lance (1-2 m) the removable section of the used rail was generally kept in place, and with a longer lance safety chains were used and the rail section was removed.
This investigation aims to clarify aspects concerning:

- Nature and sequence of the subsurface strata (geologic domain)
- Groundwater conditions (hydrologic domain)
- Physical and mechanical properties of the subsurface strata

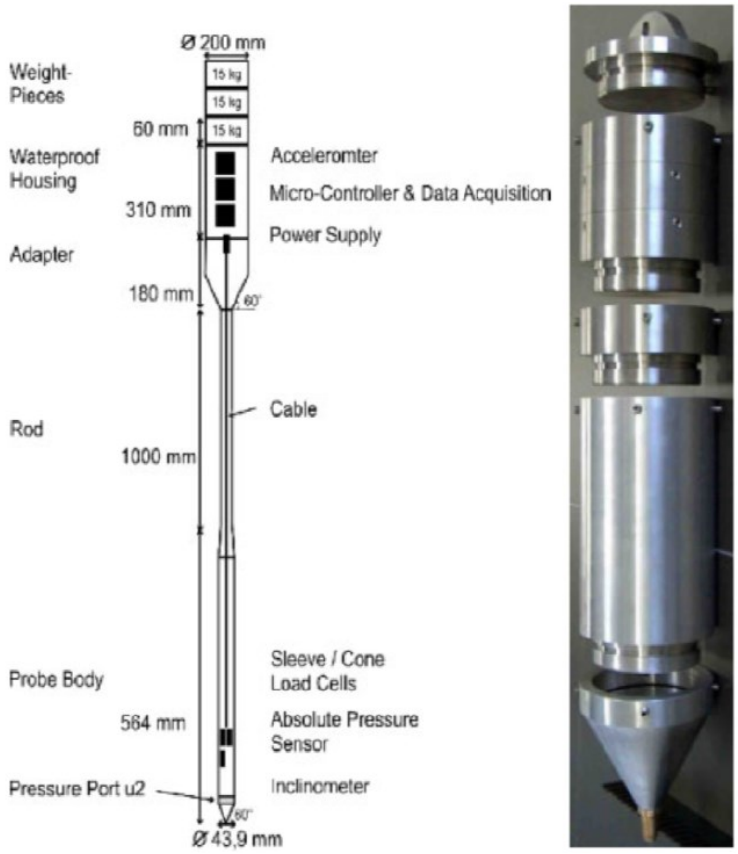

Figure 12: Schematic of CPT probe used during cruise CCGS Sir Wilfrid Laurier, September-October 2013. The penetrometer was employed in measuring sediment strength, pore pressure and geothermal heat flux. On the detail is a snapshot of the disassembled probe head.

The CPT measurements were performed during the 2013 cruise CCGS Sir Wilfrid Laurier by Greg Middleton (GSC), Timo Fleischmann (MARUM), Kira Aβhoff (MARUM) Scott Dallimore (GSC) and Charlie Paull (MBARI).

2.7. Ring Shear test

Also called torsional shear, this method allows for the characterization of the shear-stress-displacement relationship. The equipment is fundamentally composed of two metallic rings that encase the material to be tested in an annular cavity between the two rings. A normal force of chosen value (depending on the level of normal stress to be used in a particular exam) is applied to the sample and while one of the rings is kept static, the other (typically the upper one) rotates (**Figure 13**). The relative circular displacement of the rings then induces a shear force that will internally deform the tested sediment and

ultimately provoke material failure along a particular plane (Bromhead, 1979). From this technique the two produced parameters especially relevant to this work are the internal friction angle and the cohesion values, which are used in the calculation of the Factor of Safety.

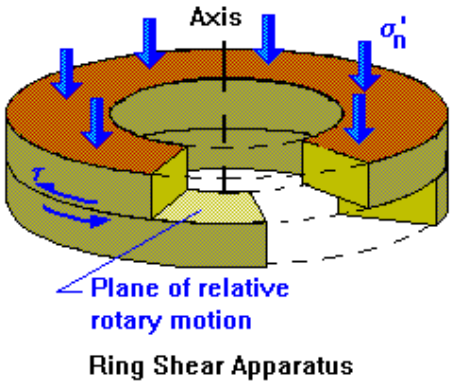

Figure 13: Schematic of the Ring Shear test equipment showing the two rings between which the material to be tested is placed. The relative movement of the rings creates a shear stress that deforms and brings the tested sediment to failure. A vertical force is also applied second to the decided normal stress to be simulated.
(http://environment.uwe.ac.uk/geocal/SLOPES/GIFS/PEAKRESR.GIF)

The Ring Shear test was realized at the geotechnical laboratory of the MARUM using samples from the 2013 cruise CCGS Sir Wilfrid Laurier, and was performed by myself, Tiago Biller, with the guidance of Matt Ikari (MARUM) and Matthias Lange (MARUM).

2.8. Equations

In this section the mathematical formulas used for the calculations and their respective variables are listed.

1. Water density as a function of temperature and concentration (McCutcheon et al., 1993):

$$D = \rho + A \cdot S + B \cdot S^{\frac{3}{2}} + 0.00048314 \cdot S^2$$

$$\rho = 1000 \cdot \left(1 - \frac{T + 288.9414}{(508929.2 \cdot (T + 68.12963))} \cdot (T - 3.9863)^2\right)$$

Where D is the total water density (Kg/m^3), ρ is the pure water density (Kg/m^3), T is the temperature (°C), S is the salinity (g/Kg), A and B are coefficients.

2. Pressure temperature correlation for checking whether GH could exist under the given conditions (Nixon & Grozic, 2006):

    a. For Methane hydrates at T≥0°C:

$$\ln P = 38.98 - \frac{8533.8}{T + 273.15}$$

    b. For Methane hydrates at T<0°C:

$$\ln P = 14.717 - \frac{1886.79}{T + 273.15}$$

With P as pressure (kPa) and T as temperature (°C)

3. Real gas equation of state (Émile Clapeyron, 1834):

$$P \cdot V = z \cdot n \cdot R \cdot T$$

Where for the gas in question P is pressure (kPa), V is volume (m^3), z is the compressibility factor, n is the number of mols, R is the universal gas constant (8.3144598 J mol^{-1} K^{-1}) and T the temperature (K).

4. Compressibility factor (Z) of natural gases(A.K. Coker):

$$Z = F_1 \left\{ \frac{1}{1 + \frac{A \cdot P \cdot 10^{1.785 \cdot Sg}}{T^{3.825}}} + F_2 \cdot F_3 \right\} + F_4 + F_5$$

Where Z is the resulting compressibility factor of the gas in question, A, F_1, F_2, F_3, F_4, F_5 and F_6 are calculated coefficients, P is the pressure (psia) T is temperature (°F) and S_g is the specific gravity of the gas.

5. Confined compression modulus relation to the coefficient of compressibility, a_v (Nixon & Grozic, 2006):

$$M = \frac{1 + e}{a_v}$$

With M as the confined compression modulus of the soil, a_v is the coefficient of compressibility and e the void ratio.

6. Volume change due to gas hydrate dissociation and the corresponding increase in excess pore pressure (Nixon & Grozic, 2006):

$$\Delta\sigma' = -\Delta u = M \cdot \left[n \cdot (1 - S) \left[0.13 - 164.6 \cdot \frac{T_2}{298.15} \cdot \frac{1}{P_2} \right] - \left(\frac{P_1}{P_2} - 1 \right) \cdot V_{G1} \right]$$

In which Δσ′ is the change in effective stress caused by melting of gas hydrate (kgf/cm^2), Δu the change in pore pressure (kgf/cm^2), M the confined compression modulus of soil, n the porosity, S the degree of water saturation, T_2 the equilibrium temperature of gas hydrate (K), P_2 the equilibrium pressure of gas hydrate (atm), P_1 the pressure at the previous step (atm), and V_{G1} the volume of the free gas at the previous pressure (m^3).

7. Factor of safety (FS) from equilibrium equations with Mohr-Coulomb constitutive law, full soil saturation and effective stresses (Steiner, 2013):

$$FoS = \frac{c' + (\gamma' \cdot cos^2[\alpha]) - \Delta u) \cdot tan[\varphi']}{\gamma' \cdot z \cdot cos[\alpha] \cdot sin[\alpha]}$$

Where FoS is the resulting Factor of Safety, c' the effective cohesion (kPa), α the slope angle(°),γ' the submerged unit weight of the soil, Δu the change in pore pressure (kPa), ϕ' the effective friction angle and Z the depth below seabed (m).

8. Drained Shear Strength (Terzaghi, 1942):

$$\tau = \sigma' \cdot \tan(\varphi') + c'$$

Where $\tau$is the shear strength, $\sigma'$is the effective normal stress, φ' is the effective friction angle and c' is the effective cohesion.

9. UNESCO freezing point of seawater (*Fofonoff & Millard, Unesco, 1983)*:

$$T_f = a_0 \cdot S + a_1 \cdot S^{\frac{3}{2}} + a_2 \cdot S^2 + b \cdot P$$

Where $T_f$is the resulting freezing temperature (°C), a_0, a_1, a_2 and b are equation coefficients, S is the salinity (PSS-78) and P is the pressure (kPa).

With the data obtained through the several described methods, the relative GH stability and Factor of Safety calculation for each of the probed positions followed the following steps:

I. Calculation of hydrostatic pressure using the water density from equation **1**;

II. Estimation of pressures at which GH would be stable based on the sediment temperatures at hand using equations **2a** and **b**;

III. Define whether GH would or not be stable by confronting the calculated GH stability pressures with the hydrostatic pressure (if pressure resulting from **I** was higher than that of **II**, GH were considered stable);

IV. Apply an increment to the measured in situ temperatures (of the positions where GH was reckoned as stable) to simulate at which temperature increment it would cease to be stable;

V. Evaluate volume increase from eventual GH dissociation with equations **3** and **4**;

VI. Approximate the confined compression modulus of the soil with equation **5**;

VII. Determine the change in pore pressure and change in effective stress from the dissociation of GH with equation **6** -based on the determined pressure and temperature values of the positions where GH became unstable after simulation of temperature increase;

VIII. Ultimately, based on the determined pressure, temperature, sediment load and geotechnical parameter values, compute with equations **7** and **8**the Factor of Safety of positions where GH became unstable after temperature increase.

The calculation of the PF stability for the probed positions used the available hydrostatic pressure, and salinity (obtained from the NOAA open data repository) to calculate with equation **9** the temperature at which ice would be stable in the sediment.

Computational implementation of the equations above in order to streamline the calculation process and allow for the creation of a versatile model of the problem at hand was done by me, Tiago Biller, using the MS Excel software. The choice of this system was based on its operational robustness, software availability, ease of use and reproducibility.

3. Results

3.1. Bathymetry

The characterization of the seafloor in the Beaufort region is here done with the aid of tridimensional grids from the Multibeam survey. The morphology can reveal elements that, underline different superficial geological aspects, allowing for an initial subdivision of the study area in different zones. Such subdivision serves as a preliminary guide to subsequent analysis.

The Beaufort Shelf surveyed morphology (**Figure 14**) is based on the intercalation of plateaus and canyons, with water depths ranging between ca. 50 m at the shelf and 1700 m at the deepest troughs. The shelf break is roughly at 100 to 120 m water depth and are a series of localized elevations contouring the shelf edge (many of which are identified as PLFs; detail example in **Figure 15**). The most significant depressions beyond the shelf break are two canyons, both with a north-west main direction and with their highest and lowest points approximately at water depths of 600 m and 1700 m respectively.

In an attempt to subdivide the morphology of the study area, broad-scale features are here considered**.** Given the central theme of this work, the first sort of noted elements are the areas with typical signs of mass movements or slides, in particular the headwalls of slope failures, as indicated by the **yellow arrows** in **Figure 14** (detail example in **Figure 16**), in front of which the canyons develop as depth increases. The result of slope failure is here highlighted by the more chaotic seafloor found in different areas (generally indicated on **Figure 14** by the orange letter **C**; detail example in **Figure 16**), all of which are lying downslope of the yellow arrow positions. These zones are quite certainly composed of remobilized material that collapsed from disrupted slopes.

The Beaufort Shelf is easily identifiable as the red plateau area of the bathymetry map, with its transition to the slope corresponding to the rather well defined transition between the red and orange color-coding. Secondary but nevertheless important features to this thesis are the roughly circular mounds interpreted as mud volcanoes, asserting the movement of fluids and therefore the dynamism of the regional stratigraphic set-up (**full yellow circles**).

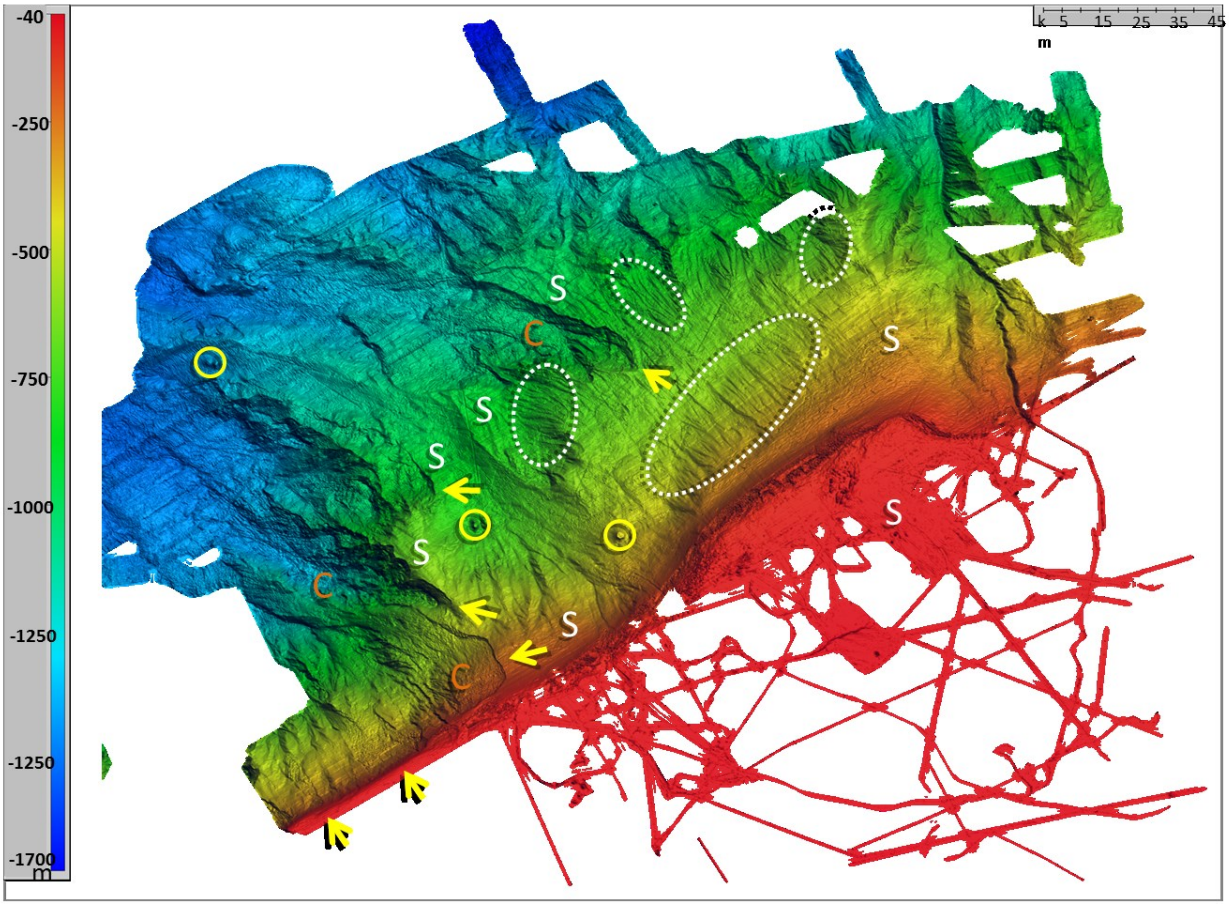

Figure 14: Bathymetry of the surveyed Beaufort Sea region, with color-coded water depth scale on the left. Vertical exaggeration: 50X. Yellow full circles: mud volcanoes: White dotted perimeters: vertically grooved areas; Yellow arrows: Headwalls of mass wasting events; 'S': Smoother areas (generally remnant topography); 'C': Chaotic seafloor zones (material remobilized by mass wasting events).

Marked by **dotted ellipses** (**Figure 14**; detail example in **Figure 17**)are a few areas where the slope is covered by grooves running parallel to the fall line, which suggests their association with gravity-driven flows, though with an apparently less dramatic - slower, less energy intensive, mobilizing process than the above mentioned slides.

In between the general feature types so far described, it is interesting to notice that have been relatively less affected by sediment remobilization (indicated on **Figure 14** with a white letter **S**). These regions have a considerably smoother morphology than their adjacencies and in many cases appear to be vulnerable to the same sorts of processes that disturbed the chaotic zones. Therefore, such areas deserve differentiated attention in estimating slope destabilization potential, being more critical candidates for geohazard occurrence.

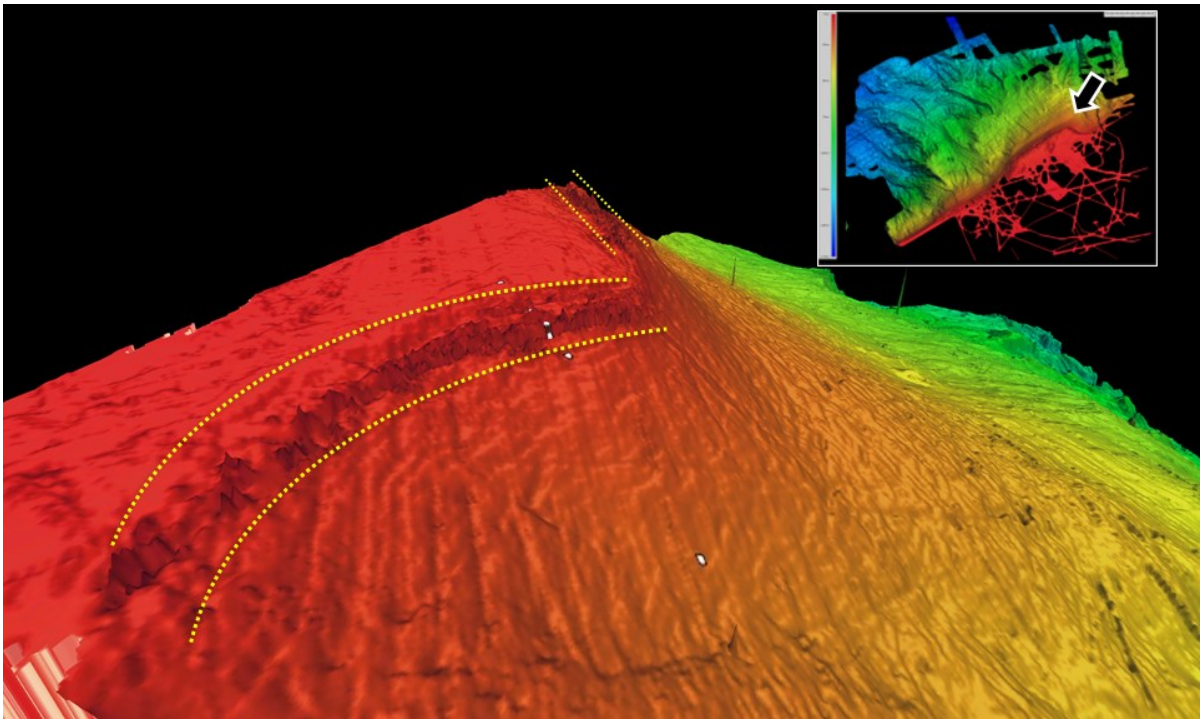

Figure 15: Detail of bathymetric grid with the shelf edge contour along which several mounds (dotted yellow lines) are found – mostly interpreted as PLFs. White dots indicate positions of CPT measurements. The approximate point of view shown on upper right corner. Vertical exaggeration: 20X.

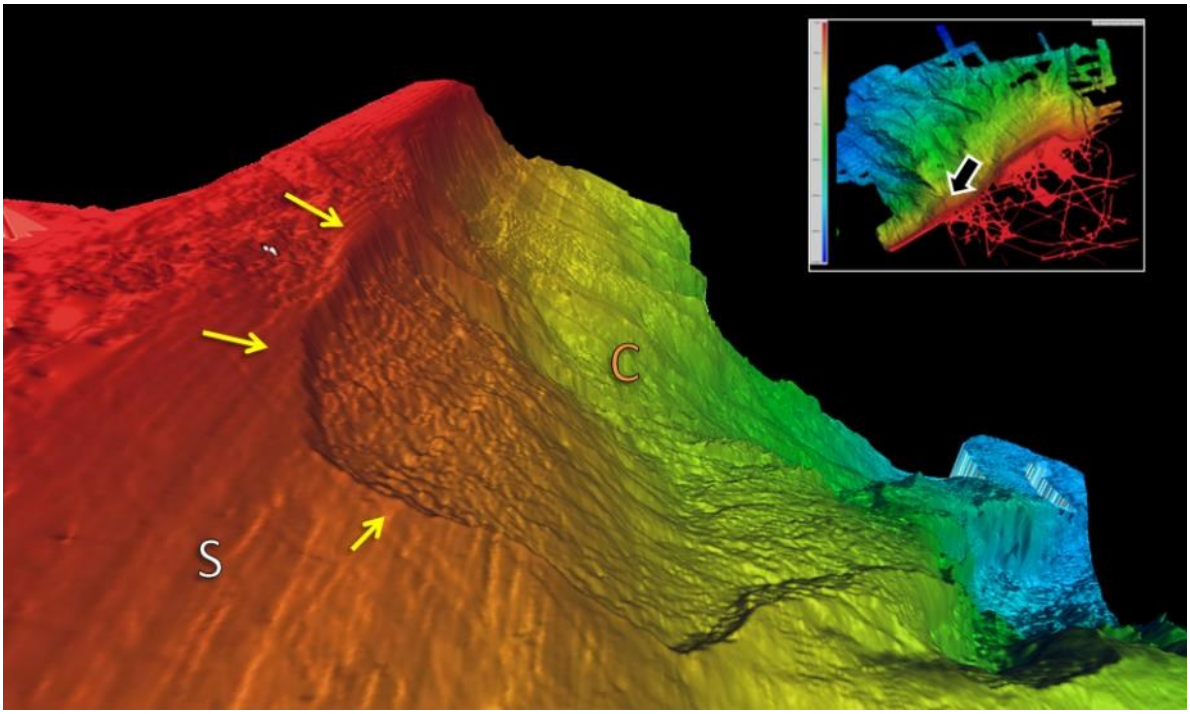

Figure 16: Detail of bathymetric grid illustrating a transition zone between smoother (S) and more chaotic (C) seafloor, where the first correlates with remnant topography and the second is a result of mass wasting. Headwall of such mass wasting event(s) is pointed by the yellow arrows. White dots indicate positions where CPT measurements were taken. The approximate point of view is shown on upper right corner. Vertical exaggeration: 20X.

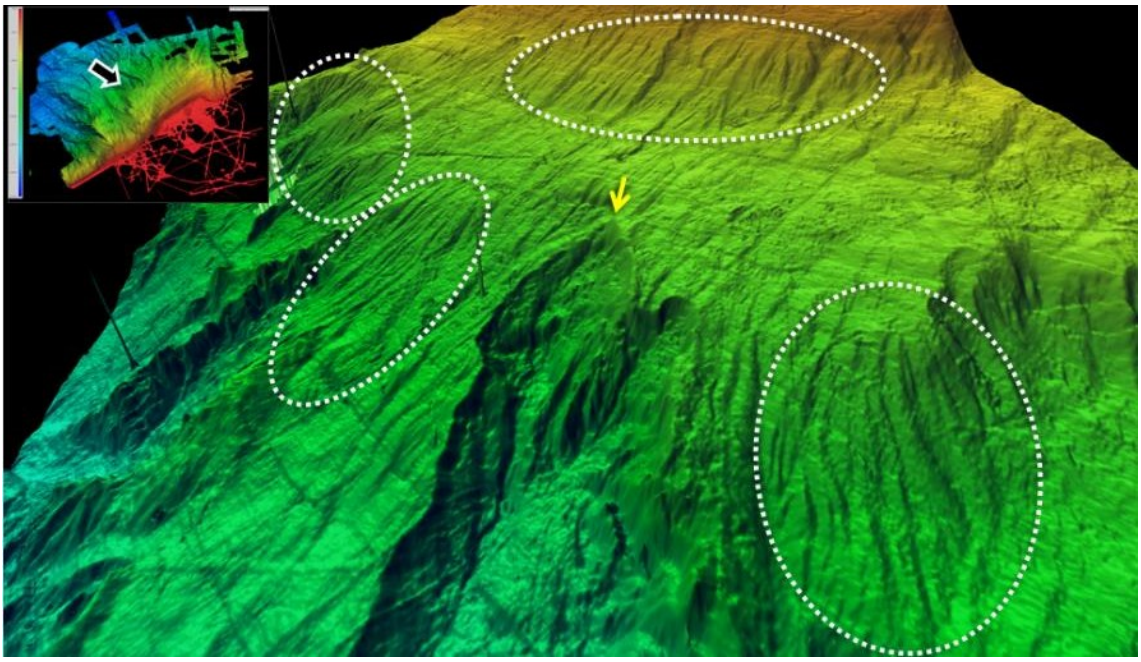

Figure 17: Bathymetric grid detail of areas where vertical grooves are found along the continental slope (dotted white circles). Headwall of past mass wasting event is indicated by the yellow arrow. The approximate point of view is shown on upper right corner. Vertical exaggeration: 20X.

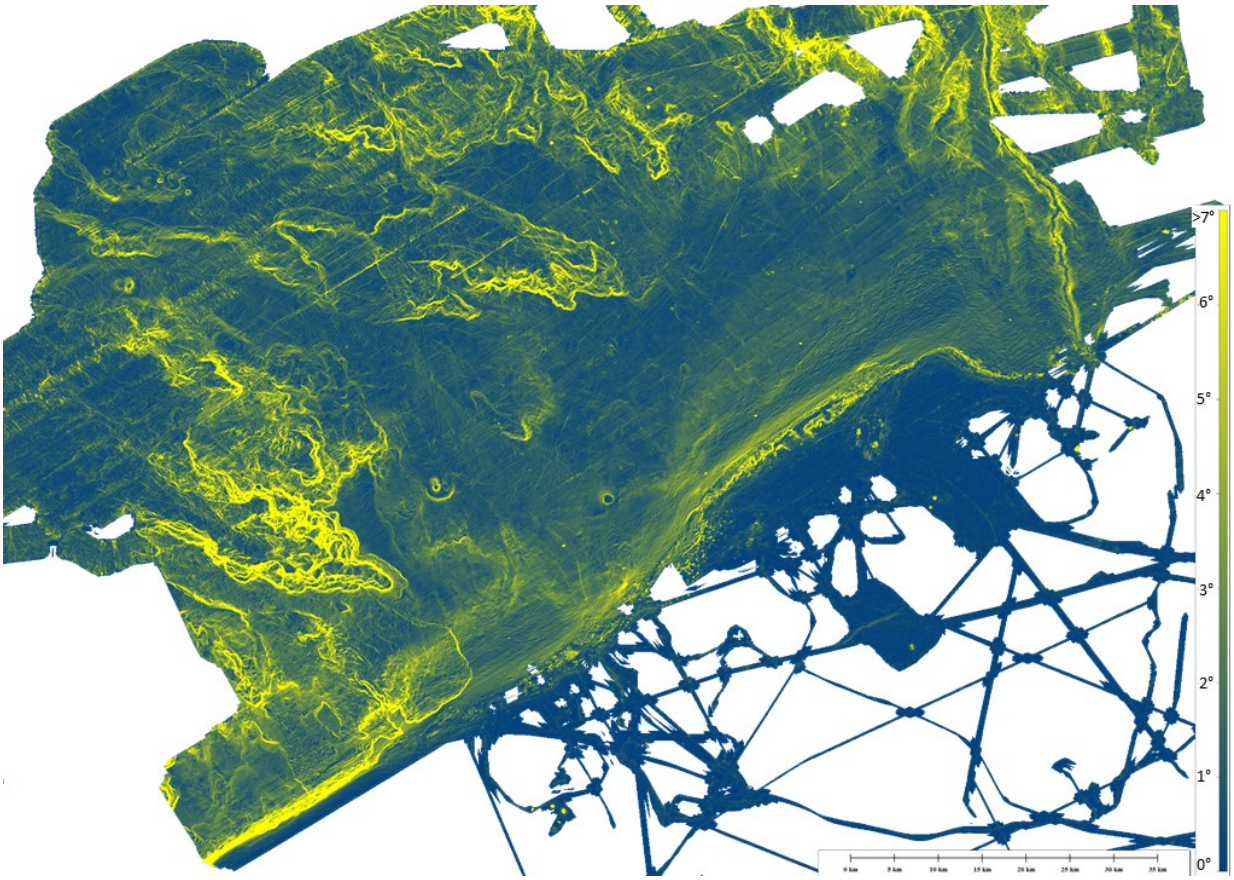

Figure 18: Map of the study area where the bathymetric information was converted into slope gradients. Yellow areas represent higher slope angles and blue areas are flatter. Scale gives the slope angles.

As an input to the Slope Stability calculations, the bathymetric data was also used to produce maps based on the slope angles as seen in **Figure 18**. In this map it is evident how the higher slope angles correspond to the locations of major mass wasting events.

3.2. SBP

The produced sub-seafloor images display the interesting way in which the regional stratigraphy is arranged, with the sedimentary strata normally corresponding to seismoacoustic reflection surfaces resulting of changes in impedance (product of the acoustic velocity in the sediments and their density). In this thesis the analyzed SBP are focused on the features around the shelf-slope transition and on the locations with considerable slope gradients (for being typically more prone to mass wasting). This part of the work aims to identify patterns indicative of geohazards (either ongoing or suspected to happen in the future) and extended the punctual measurements information (physical properties of sediment cores, CPT, temperature, etc.) to the surrounding region - all within the limits of the currently accepted scientific principles and of the dataset itself. An overview of the SBP positions can be seen in **Figure 19**.

Regarding the dataset it is initially observed that above the shelf break the acoustic signal has a rather low penetration capacity. This effect might reasonably be associated with the inferred regional permafrost-bearing sediment (PBS) distribution and the reported relationship between sub-surface PF and an important reduction in SBP penetration (Jin & Riedel, 2014). It is rather safe to conclude that the lack of sub-seafloor imaging on the shelf area is a result and confirmation of the PF presence in the area (**Figure 20** and **Figure 21**).

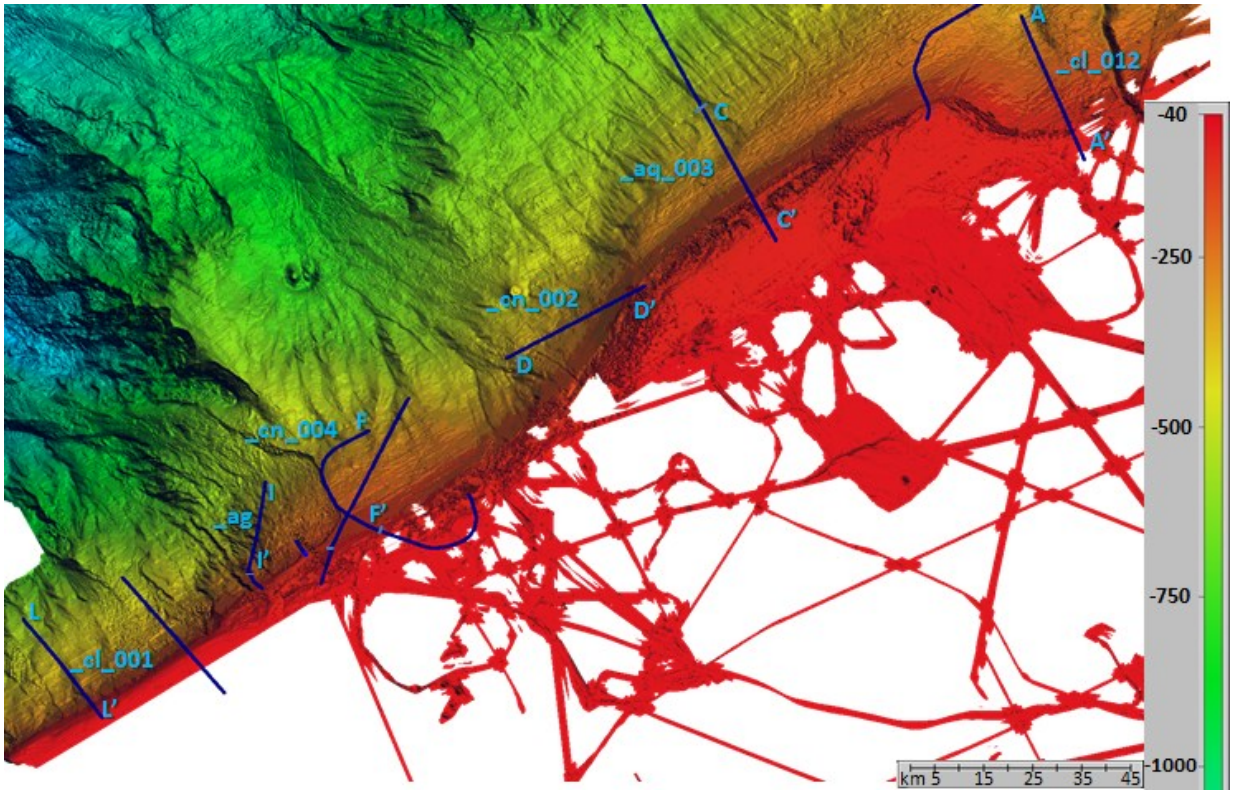

Figure 19: Track lines of the described sub-bottom profiles around of the Beaufort shelf.

Figure 20: SBP ARA05C_cl_012. The penetration of the acoustic signal progressively increases downslope, being particularly low at the shelf, likely effects of the downward thickening sediment layers (also caused by material more prone to signal penetration) and of the permafrost-bearing sediment inhibiting acoustic measurements. The vertical interruptions on the slope (observable in practically all the profiles) are often gaps in the data sequence caused data acquisition issues.

Right below the shelf break the effect observed on the shelf area rapidly gives place to a richer context. From this point on the sub-bottom reflectors begin to be visible, with the thickness of the penetrated sediment interval sensibly increasing (**Figure 21**). This signal penetration behavior could, at least in part, be a result of the higher sediment accumulation rates in the deeper regions (granted sufficient sediment supply), promoting the deposition of thicker layers. Given the regional stratigraphic structure discussed in the chapter **Stratigraphy and Structure**, certain discontinuity zones are expected to be highlighted by the SBP, particularly the transition between the here named Unit A and Unit B (**Figure 5**), interpreted as a passage dating from the last oceanic transgression.

Along the continental slope, the analyzed profiles show several elements that are here divided in two main groups: those deforming (or even piercing through) the seafloor and those having practically no expression on the morphology; of course ignoring apparent data acquisition artifacts. In the first group are mostly mounds (likely PLFs or mud diapirs), found either isolated (generally right above the shelf break or clustered downslope); e.g.: profiles ARA05C_cn_002, Shot Point (SP) 5900-6130 (**Figure 21**) and ARA05C_aq_003 (**Figure 24**). Depending on the penetration and quality of the profiles, these bodies can be vertically traced all the way through the exposed sub-bottom reflectors (e.g.: profile ARA05C_cl_012, SP 450-550, 800-850, 925-980; **Figure 20**), indicating a rather deep rooting structure, though in some seemingly less frequent cases a lower boundary is shown (e.g.: profile ARA05C_cl_001, SP 1900-1700; **Figure 23**). In this first group are also somewhat smooth superficial irregularities, which seem to be related to underlying parallel reflectors that are in general folded or interrupted by apparent faulting (e.g.: profile ARA05C_cl_012, SP 1200-1500, 1830-2900; **Figure 20**).

The second group here broadly defined, that of SBP features with little or no clear effect on the local bathymetry and is mainly represented by discontinuities (horizontal and vertical; e.g.: blanking, erosional surface) and discordances (e.g.: angular discontinuity) of reflectors. These elements tend to be slightly deeper in the reflector sequence, below the first layers of draped sediment. Examples of such elements can be seen on the SBPs: ARA05C_cn_004 (SP 13270; **Figure 22**), ARA05C_cl_012 (SP 1090-1135; **Figure 20**), ARA05C_cl_001 (SP 2045, 1720-1800, 600; **Figure 23**) and ARA05C_cn002 (SP 8780-8150; **Figure 21**).

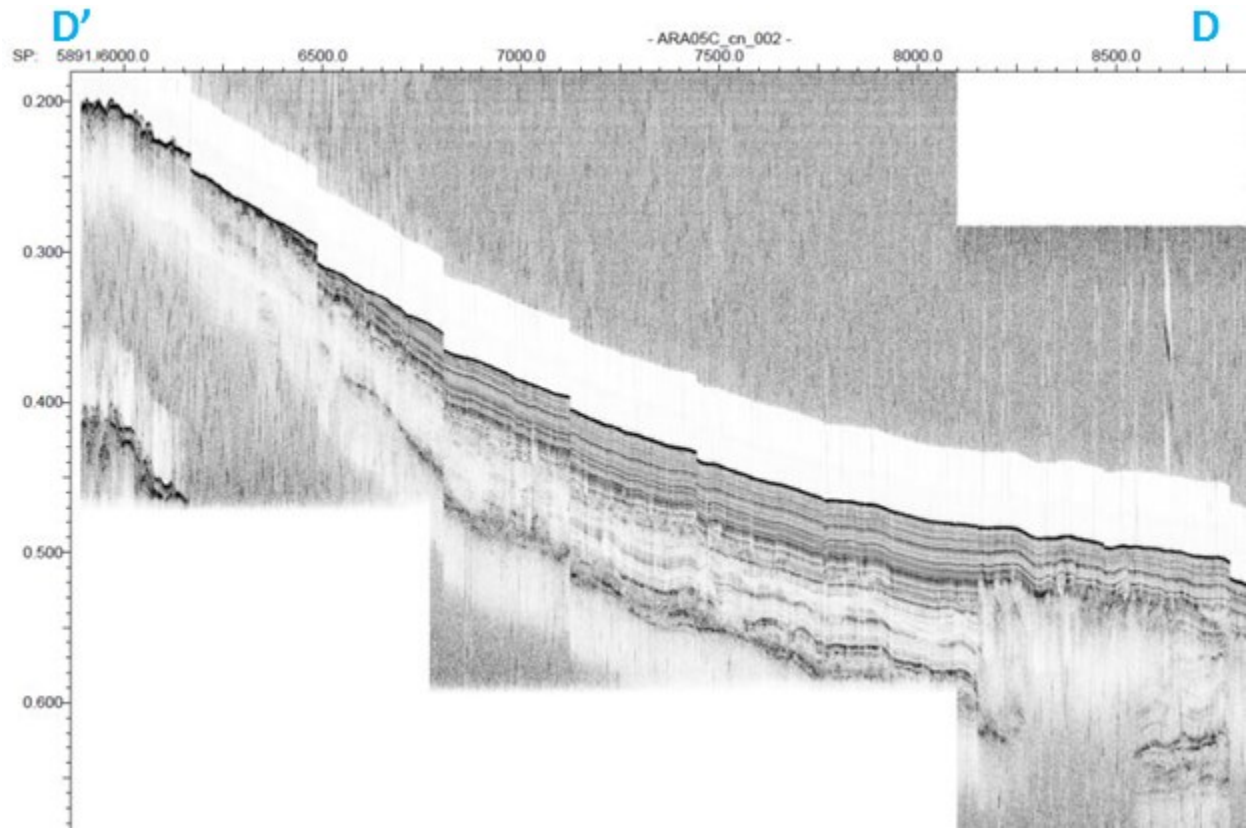

Figure 21: SBP ARA05C_cn_002. Acoustic signal penetration progressively increases downslope, being lowest at the shelf, as in Figure 20, likely effects of the downward thickening of the sediment layers (perhaps also caused by material more prone to signal penetration) and of the permafrost-bearing sediment inhibiting signal penetration, respectively. Such pattern is found whenever a profile approaches the shelf and/or crosses a region with ice-bearing sediments (almost ubiquitously at water depths less than 120 – 100 m).

Beyond the features of the profiles already mentioned the slope failure evidence in the available records is also a major aspect of this study. Characteristically, the signs of such events are headwall/failure scars (ideally with well-marked strata interruption) followed by a downslope region along which the collapsed material imposed a distinguishably more chaotic pattern. Profile ARA05C_ag (**Figure 25**) perfectly shows such a set-up. In it, roughly between SP 1 and 125 the apparent remnant stratigraphy is represented by a harmonious parallel reflector succession, then interrupted by a brusque vertical drop, interpreted as the headwall, and followed by a stretch of fairly disorganized topography and unclear sub-bottom reflections (SP 230-1050).

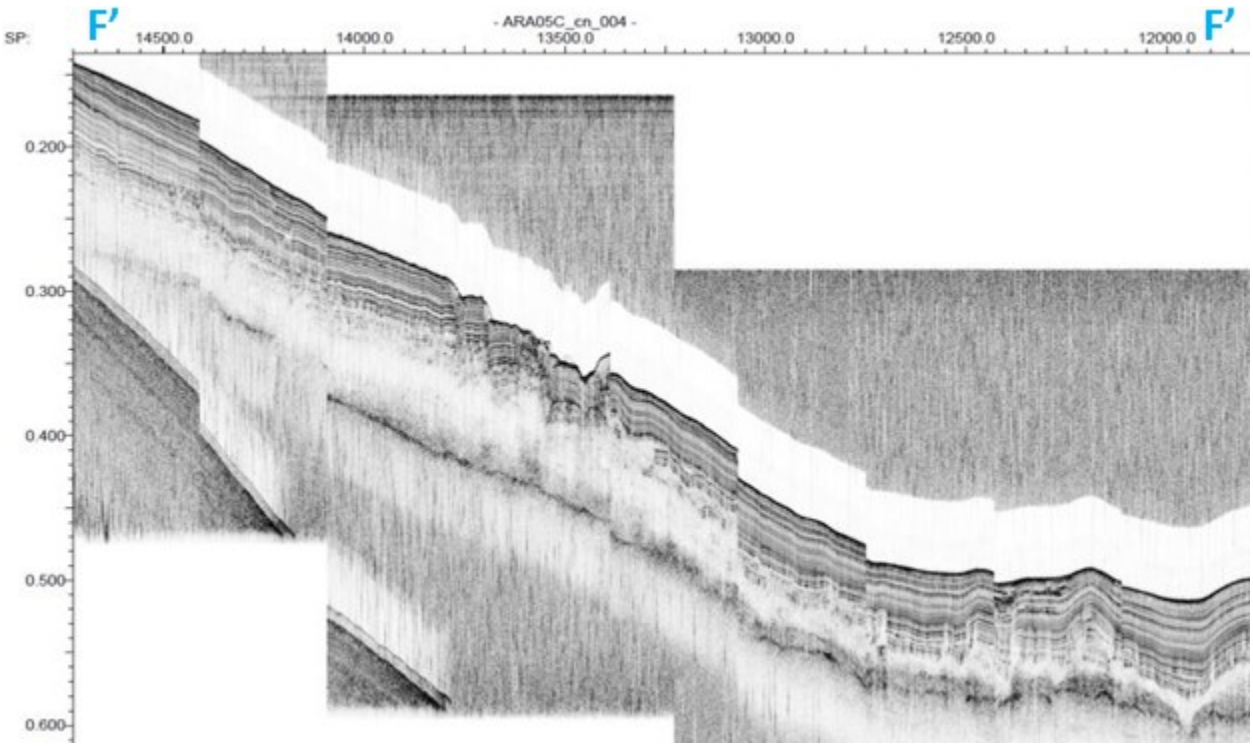

Figure 22: SBP ARA05C_cn_004. Between shot points 13800 and 13350 the sequence of parallel reflections observed throughout the profile is interrupted by an interval of rougher topography and more complex sedimentary structure, apparently also including vertical disruption of the sub-bottom layers.

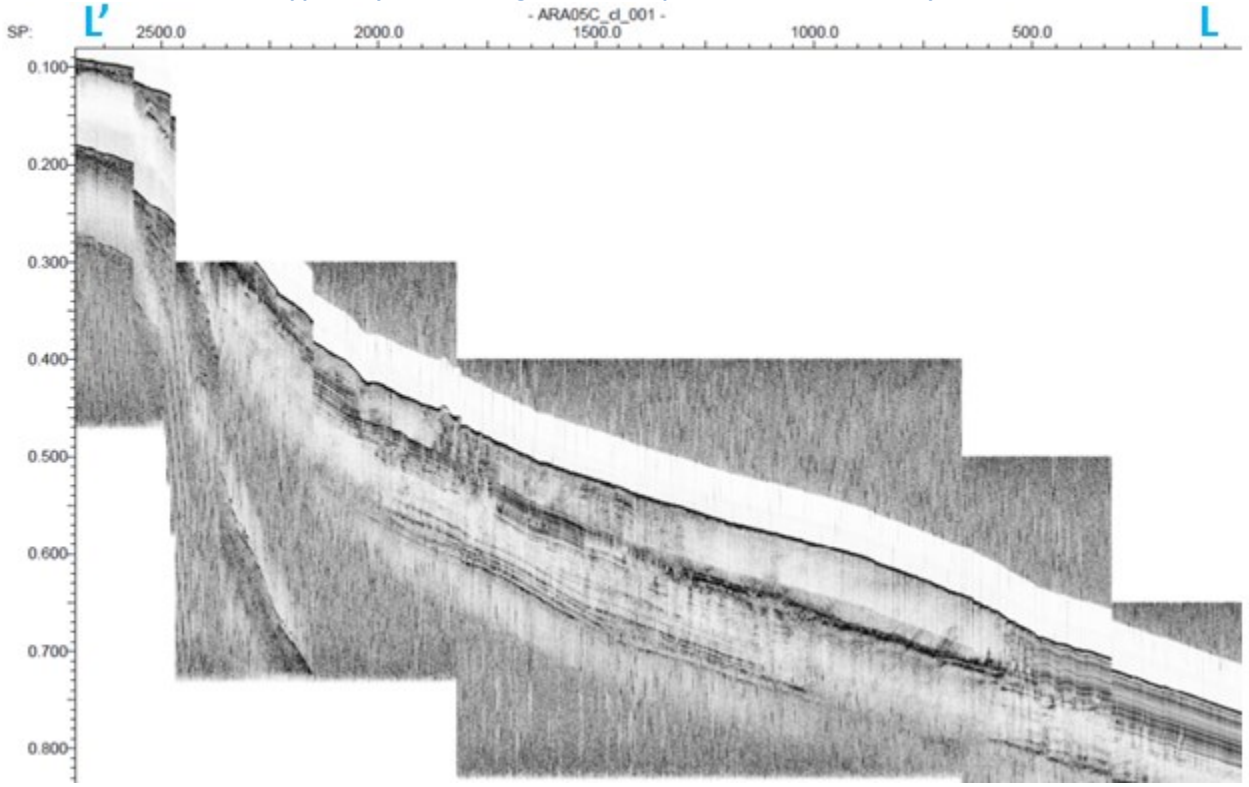

Figure 23: SBP ARA05C_cl_001.Particularly interesting profile, in which the following can be found: vertical strata interruption (SP 2100), partial blanking/lack of reflections (SP 2100-550), reflectors being pierced (SP 1750), exposure of deeper reflections (SP 2100-1100 – conceivably as more acoustic energy gets through the sediment due to conducing impedance properties of upper strata).Data cut between SP2500 and 2250 is due to data acquisition issues.

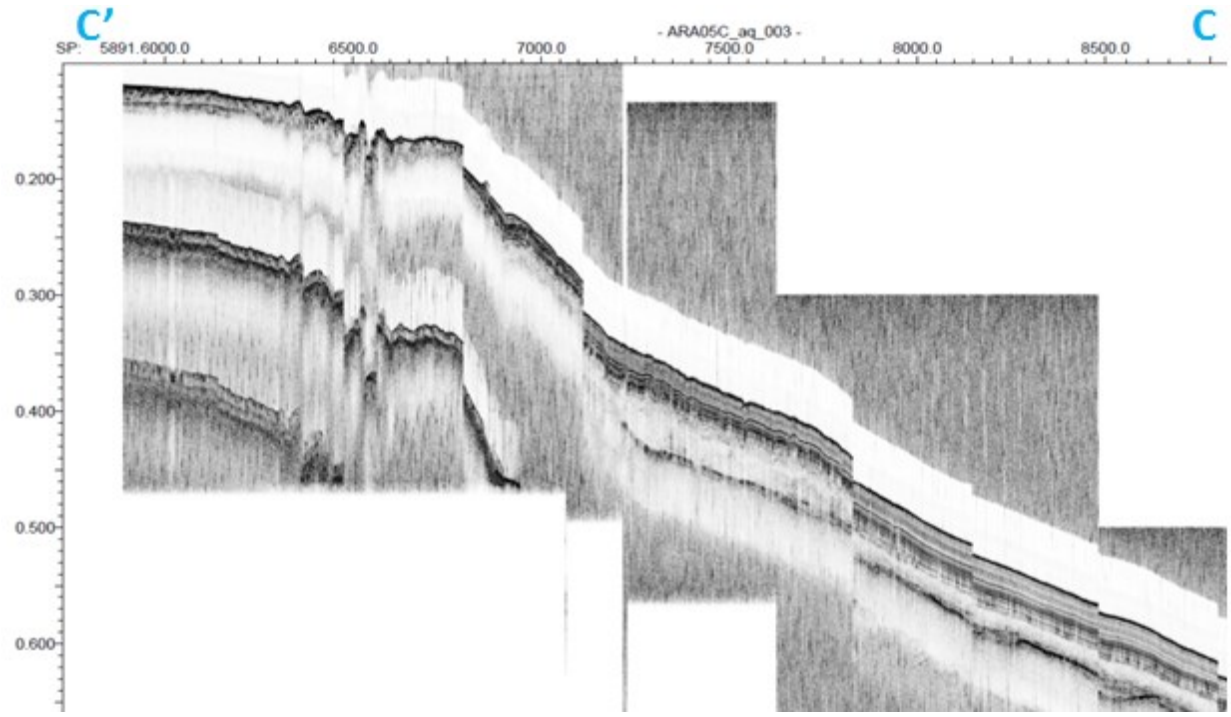

Figure 24: SBP ARA05C_aq_003. Presence of mounds interpreted as pingo-like features (PLFs) around the shelf break and upper portion of the slope (SP 6900-7900) displaying a wrinkly seafloor and reflector sequence than the contiguous sediments downslope.

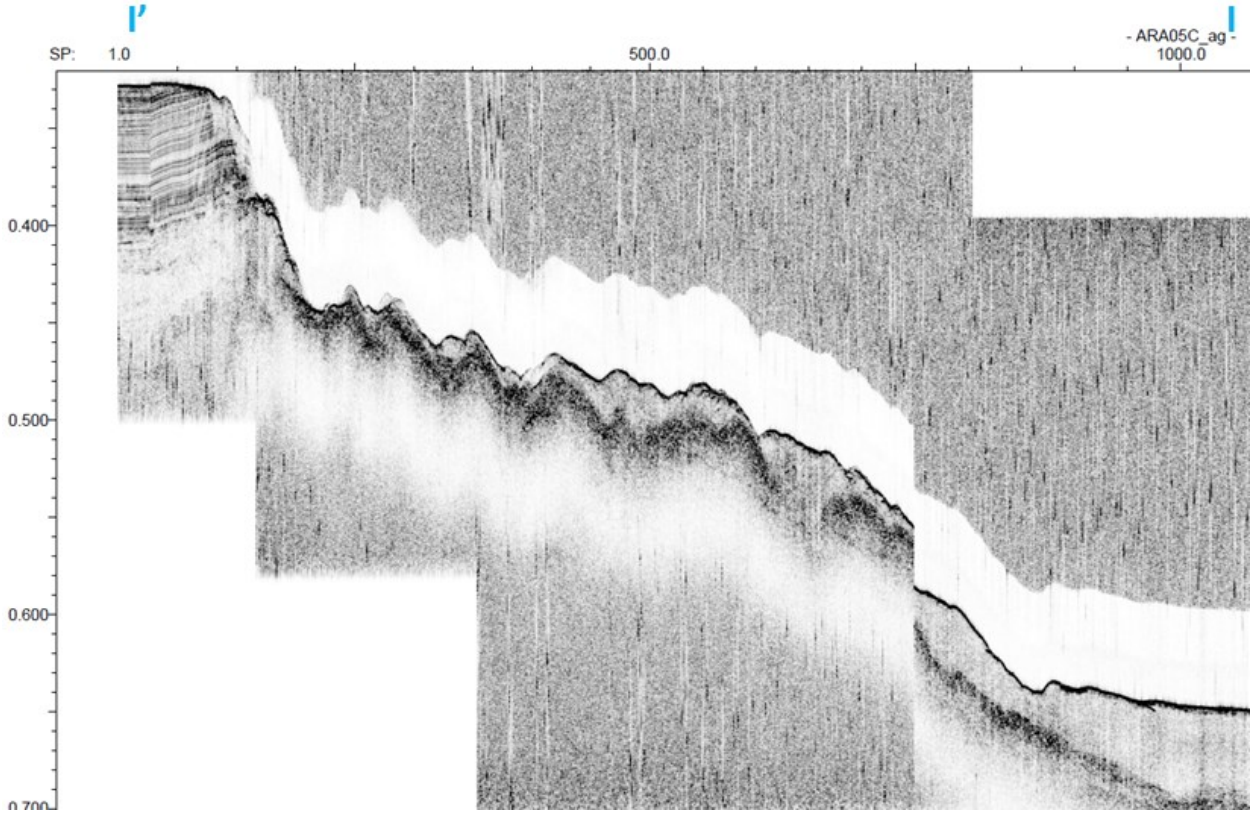

Figure 25: SBP ARA05C_ag. In this comparably short profile the transition between an area thought to be preserved topography and an adjacent portion where slope failure took place is shown. The remnant topography (top left) corresponds to a sequence of parallel layers. Virtually the whole rest of the profile represents a zone severely modified by a mass wasting event, with the absence of a discernible stratigraphic structure and a quite irregular seafloor.

The phenomenon of fluid displacement within the sedimentary succession is one that should also not be ignored. Though not always fully straightforward, this physical process is seemingly related to what is seen in **Figure 20** (line ARA05C_cl_012 SP 400-1000), **Figure 23** (line ARA05C_cl_001 SP 1800-1300), **Figure 24** (line ARA05C_aq_003 SP 6300-6700) and **Figure 21** (line ARA05C_cn_002 SP 8100-8800). In these, the upward flow of material (probably driven by density contrasts) seems to be of importance. In the first and third of these cases and less clearly in the second one (due to its higher complexity), the closest evolution model would be that of a mud diapir or a PLF, given the relatively deep rooting (within the context of the here assessed SBPs) and the piercing through several sediment layers. The fourth case matches the features described on the other three in its shallowest part, although its deeper portion presents a more intriguing feature. In this profile (ARA05C_cn_002) a progressive, especially enhanced, signal penetration occurs downslope, culminating with a sudden blank area delimited by reflector disturbances. These suggest a volume of material pushing through the lowermost strata but being contained by the uppermost layers without reaching the sediment surface.

3.3. Physical properties

The properties here exposed are result of tests and measurements done on the retrieved sediment core samples and in-situ (as explained in the **Materials and Methods** section). In this study, the central purpose of this data is to ultimately serve as input for the calculations of GH, PF and slope stability, besides helping to understand the characteristics of the local sedimentary sequence. As the spatial distribution of the physical property data is of limited coverage and density, concessions have to be made to allow for reasonable extrapolation and zonal extension of the punctual measurements.

Deriving from the methods exposed in the previous section of this thesis, the tables below show a compilation of the parameters collected, essentially representing the most superficial stratigraphic unit in the Central Shelf of the Beaufort region (**Figure 1**, **Table 1**, **Table 2** and **Table 3**). The positions seen in **Figure 68** are those where gravity cores were collected during the cruise ARA05C and these cores were the source of the material examined with laboratory testing. Detailed granulometric composition of sediment from locations thought to fairly approximate the broader regional context can be found in **Figure 26**, **Figure 27** and **Figure 28**.

Table 1: Summary of Unit A physical properties from the Ikit Trough.

Summary of Unit A* physical properties from the **Ikit Trough**			
Property	Mean	Min.	Max.
Plastic Limit (%)	27	20	32
Liquid Limit (%)	54	39	75
Moisture Content (%)	51	27	93
Bulk Density (g/cm^3)	1.61	1.48	1.85
Clay (%)	53	38	64
Silt (%)	46	35	61
Sand (%)	2	0	7
Undrained Shear Strength (kPa)	7	1	15
OCR	4	1	15
Cc	0.41	0.2	0.72
*Horizontal sequence of recent marine silt and clay deposited subsequent to the last sea level rise			

Table 2: Summary of Unit A physical properties from the Akpak Plateau.

Summary of Unit A* physical properties from the **Akpak Plateau**			
Property	Mean	Min.	Max.
Plastic Limit (%)	24	15	35
Liquid Limit (%)	49	30	82
Moisture Content (%)	55	21	92
Bulk Density (g/cm^3)	1.76	1.6	1.92
Clay (%)	35	25	47
Silt (%)	49	44	57
Sand (%)	13	3	22
Undrained Shear Strength (kPa)	7	1	24
OCR	--	4	12
Cc	0.44	0.37	0.58
*Horizontal sequence of recent marine silt and clay deposited subsequent to the last sea level rise			

Table 3: Summary of Unit A physical properties from the Kringalik Plateau.

Summary of Unit A* physical properties from the **Kringalik Plateau**			
Property	Mean	Min.	Max.
Plastic Limit (%)	29	22	33
Liquid Limit (%)	58	42	71
Moisture Content (%)	54	32	85
Bulk Density (g/cm^3)	1.5	1.3	1.8
Clay (%)	62	56	65
Silt (%)	36	34	38
Sand (%)	3	0	6
Undrained Shear Strength (kPa)	28	6	48
OCR	7	6	8
Cc	--	--	--
*Horizontal sequence of recent marine silt and clay deposited subsequent to the last sea level rise			

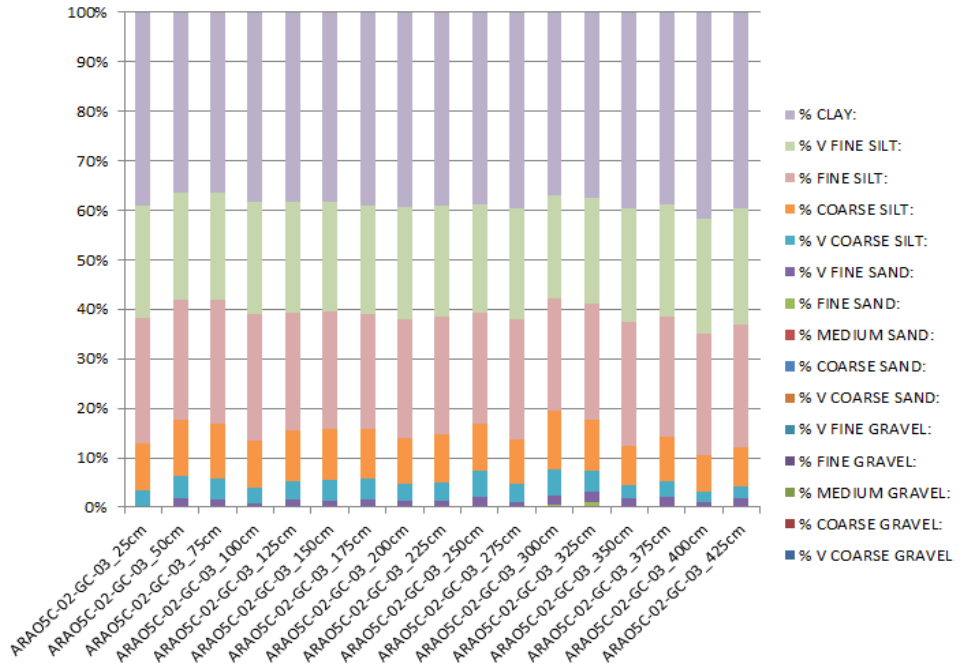

Figure 26: Granulometry of core ARA05C-02, ST02. Vertical axis shows the percentage of the standard grain size classes and the horizontal axis gives the depth (cmbsf) of the sediment sample.

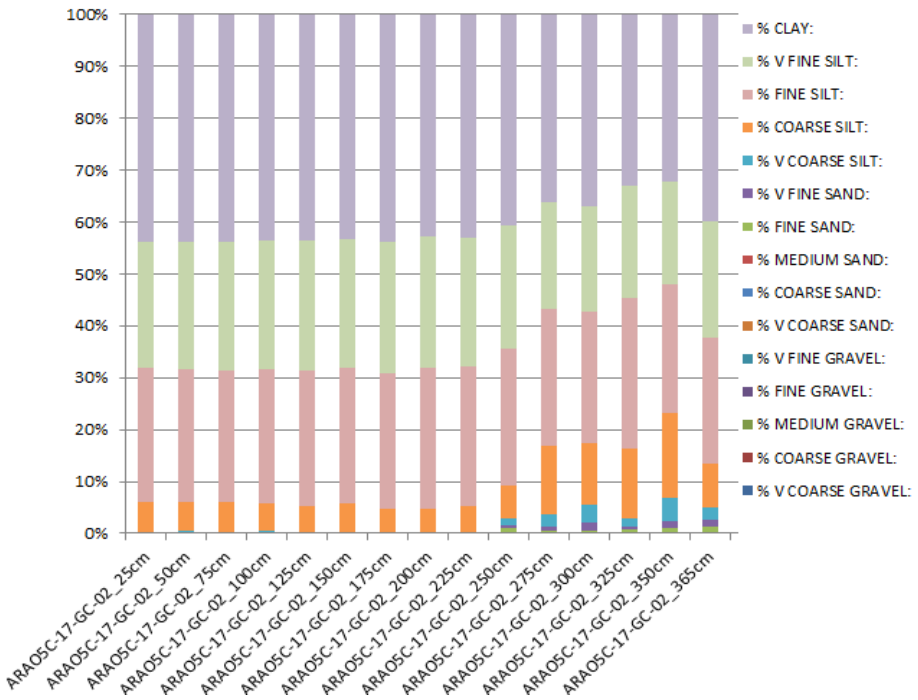

Figure 27: Granulometry of core ARA05C-17, ST17. The vertical axis indicates the percentage of the grain size classes while the horizontal axis gives the depth (cmbsf) of the sediment sample.

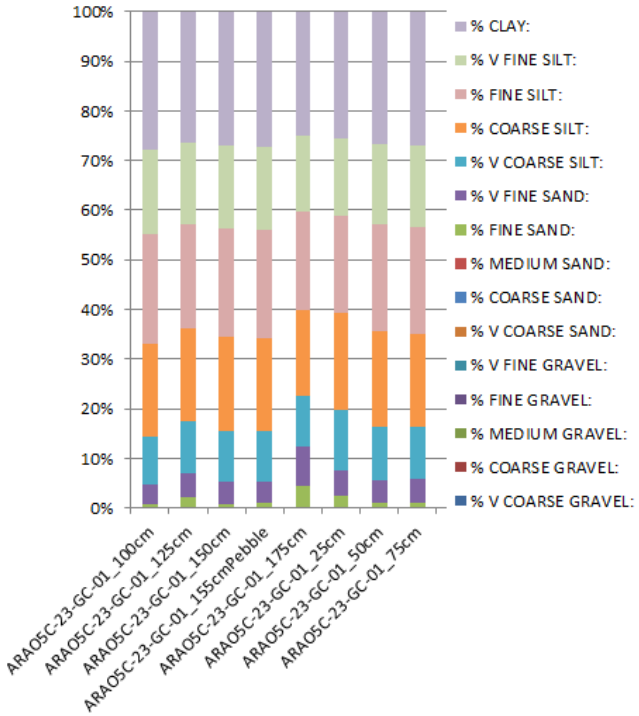

Figure 28: Granulometry of core ARA05C-23, ST23. Vertical axis shows the percentage of the grain size classes and the horizontal axis gives the depth (cmbsf) of the sediment sample.

From the granulometric data above it can be observed that if fine material represents the major portion of the sediment compositions, sediments from closer to the shelf present a more important fraction of larger grain sizes. ST17 (850 m water depth) has an almost negligible amount of grains larger than silt, while ST02 (409 m water depth) shows a slight increase of such coarser material and, most interestingly, ST23 (114 m water depth) has a markedly coarser composition, with fine sand reaching over 10% of the bulk sediment. This variation is very likely related to the important terrigenous contribution (the Mackenzie River being a main source of it), though the occurrence of PLFs and diapirs might also play a role bringing material from deeper in the sediment and mass wasting events could promote material remobilization.

3.3.1. CPT and Ring Shear

These CPT measurements constitute a main source of information for identifying sedimentary layers or intervals that could be of importance in identifying potential slide surfaces, zones of pore pressure accumulation, low strength, etc. When encountered, such intervals or transition zones are associated with other data (i.e.: sediment temperature, lithology, cohesion, effective friction angle) and focused on calculating the Factor of Safety at a given location. A crucial limitation of this dataset is its limited seafloor penetration depth (<3 mbsf). Based on available literature and other data (especially the SBP), vertical and horizontal extrapolation of the obtained CPT values will be attempted.

The role of the parameters produced by the CPT and here described (e.g.:tip resistance, sleeve friction and pore pressure) is particularly useful in this thesis to distinguish between sediment layers tending towards either coarser or finer granulometric compositions. Materials with sand-bound characteristics will have tendency to high tip resistance, low sleeve friction and fast pore pressure dissipation (high permeability), while clay-bound sediment will follow the opposite pattern (Meigh, 1987). From these principles and after a brief observation of the data in question, it can be seen that transitions between finer and coarser sediments occur at different depths at each individual plot (**Figure 30**, **Figure 31** and **Figure 32**). Position of the CPT stations can be seen in **Figure 29**.

In order to achieve the best results, the CPT data were processed using an *in-house* Matlab script crafted by Robert Roskoden, in which the raw data goes through a series of computational steps that ultimately deliver the following plots.

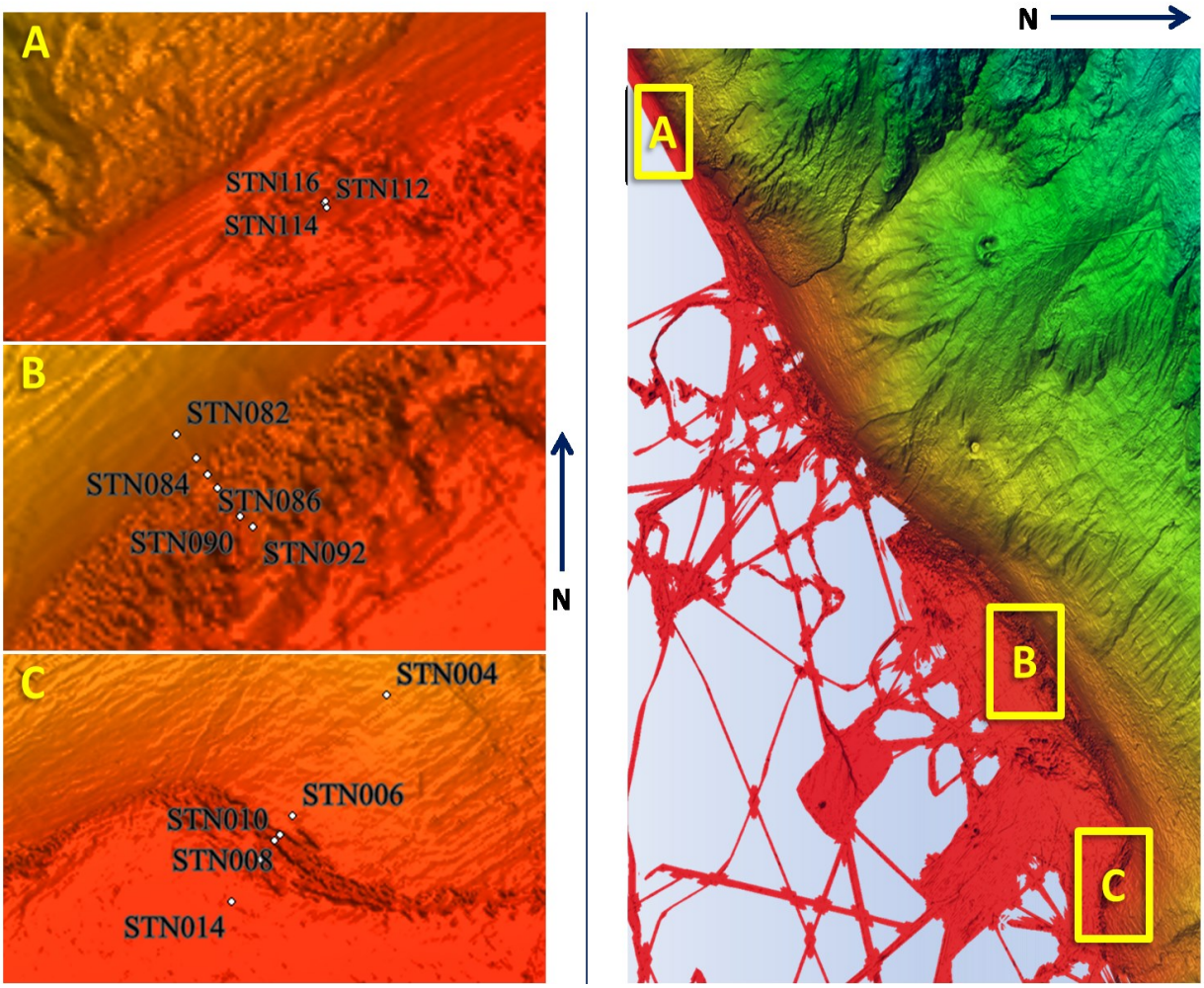

Figure 29: Location of CPT stations along the Beaufort Shelf and Slope. A) South of Slide, with STN 112 to 116, B) Central Shelf, with STN 82 to 92 and C) East Shelf with STN 04 to 14.

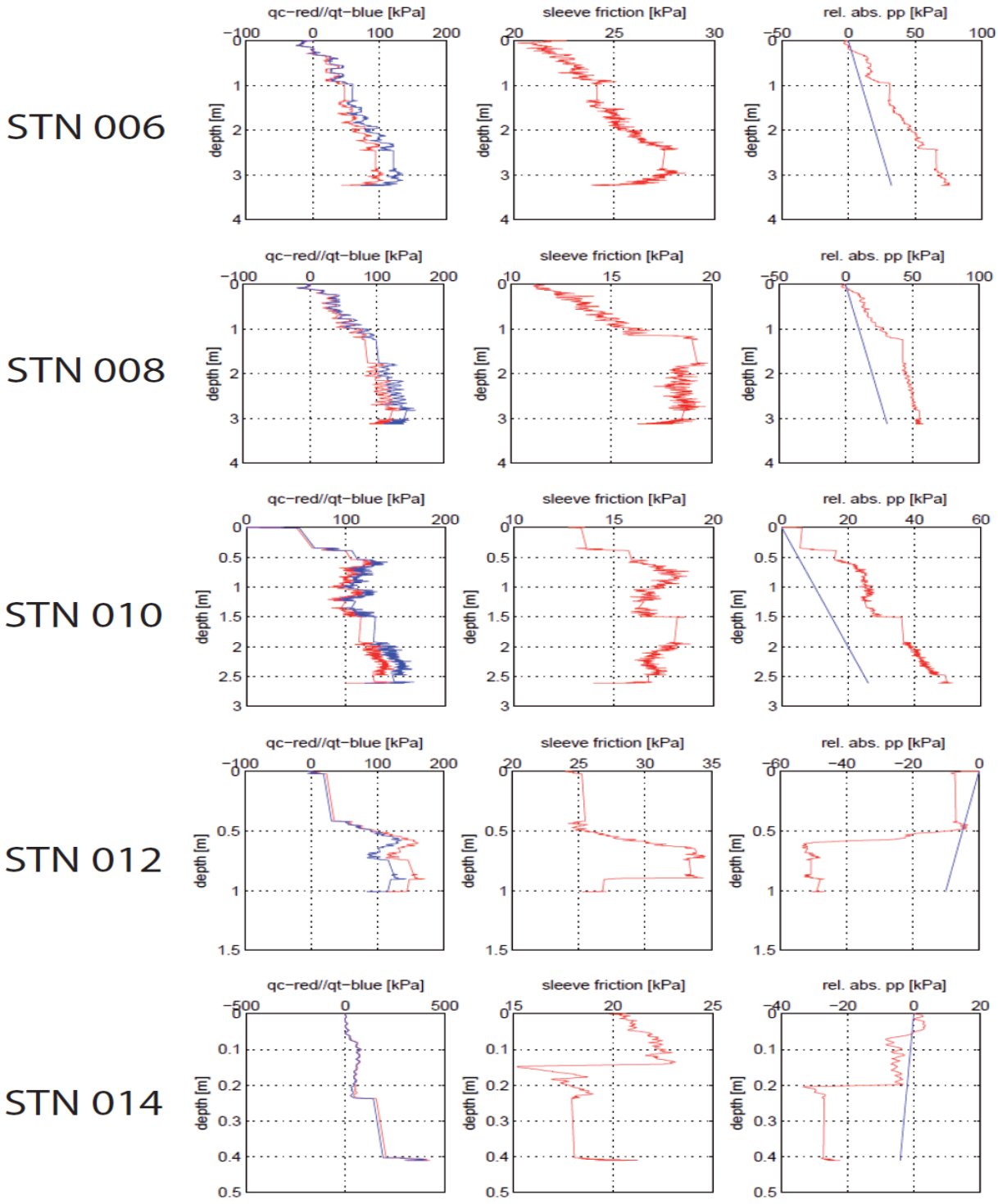

Figure 30: CPT results of the Eastern Shelf, including values of tip (or cone) resistance, sleeve friction and pore pressure.

STN 084

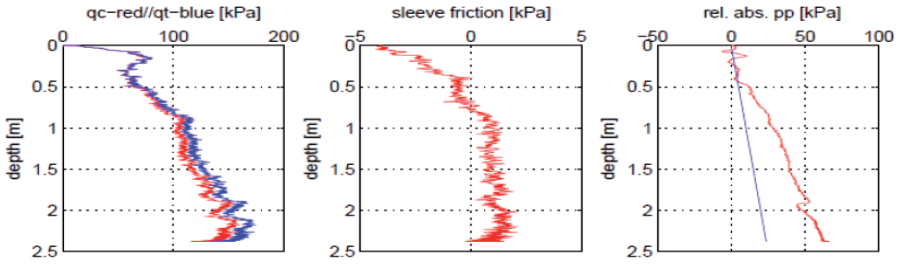

STN 086

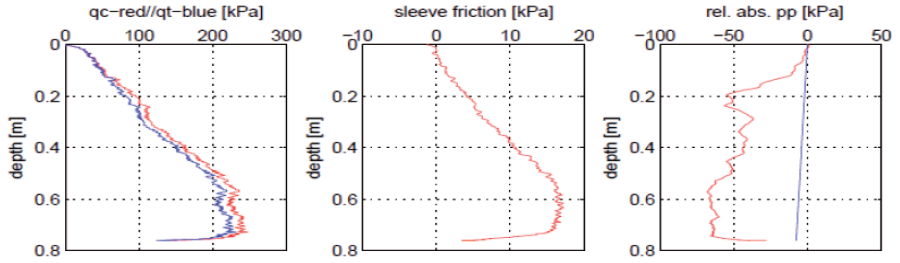

STN 088

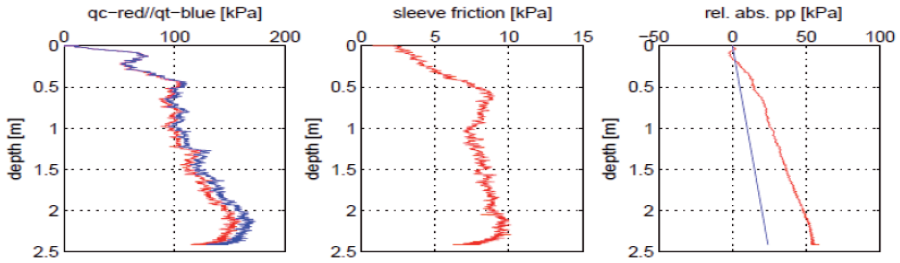

STN 090

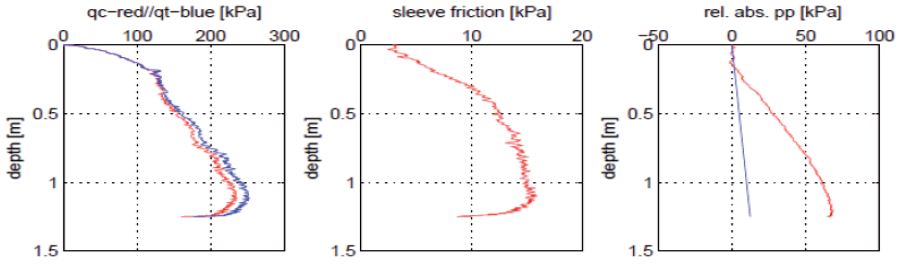

STN 092

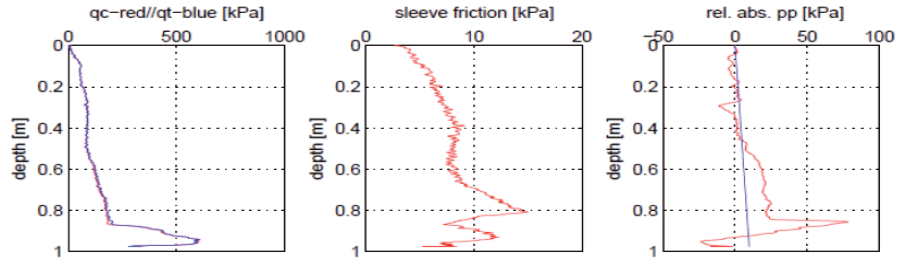

Figure 31: CPT results of the Central Shelf, including values of tip resistance, sleeve friction and pore pressure.

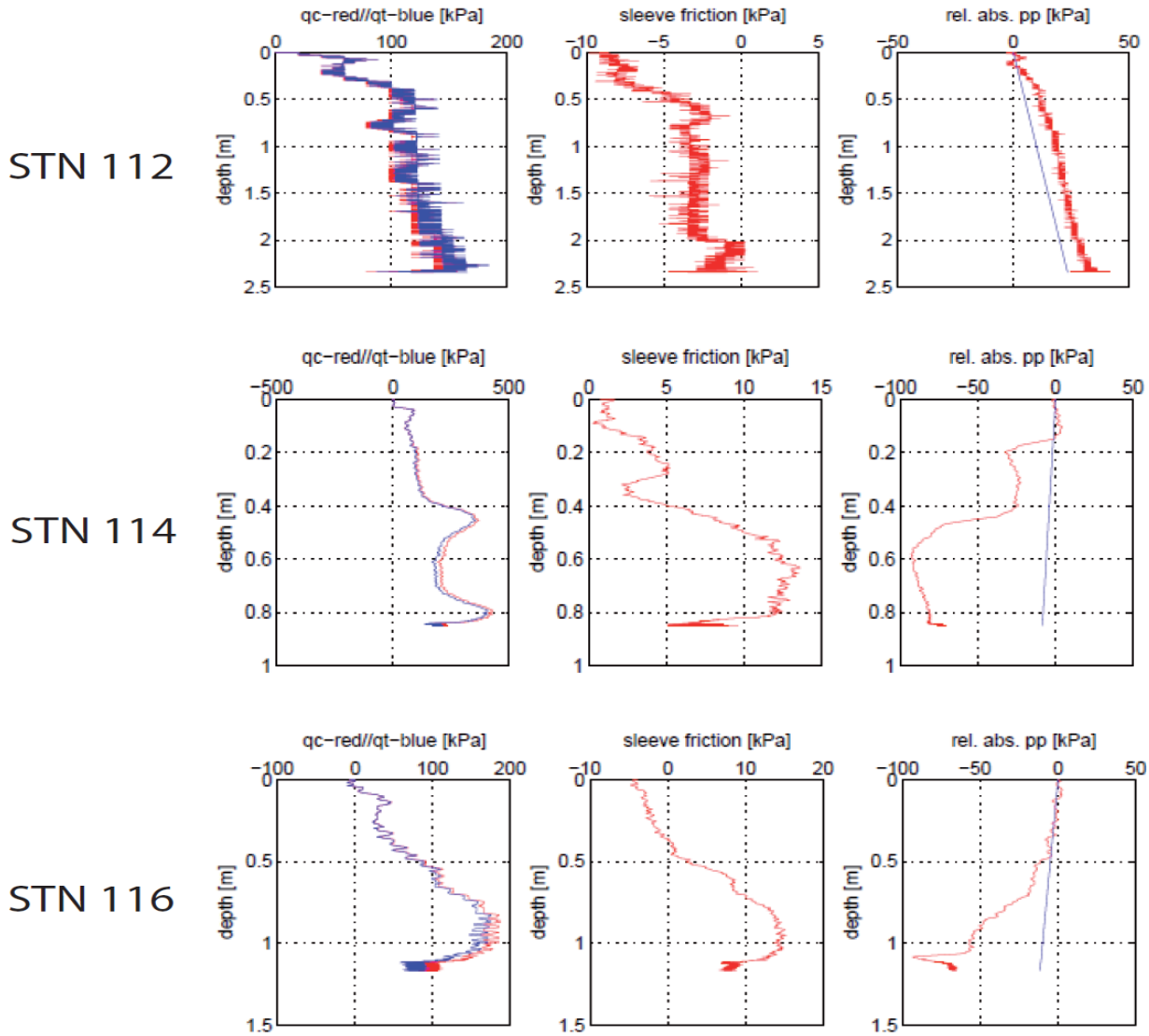

Figure 32: CPT results of the, including values of tip resistance, sleeve friction and pore pressure.

The Ring Shear test was the last experiment to be realized, producing parameters of fundamental importance for Factor of Safety calculations. The outcomes of the Ring Shear derive from the Laurier 2013 cruise samples. The tested sediments were taken from the Central Shelf area at positions STN 81 (230 m) and STN 87 (185 m water depth), both from ≈1.2 mbsf (**Figure 72**).

After simulating approximately the same sediment loads as the in situ conditions and creating data series ranging from the nearly undeformed sediment, through the peak deformation and finally to the residual conditions, the maximum values were translated as shear strength. The results were then clustered and averaged, ultimately delivering a shear strength of 4.8 kPa. Though reduced to a single value, the shear strength is considered representative of the sediment interval for which calculations were performed, mostly because of the relatively small depths and for the cogitated bulk homogeneity of the top sediment layers in the studied region.

From the Drained Shear Strength equation (section 2.8), it is understood that the shear strength is in direct correlation with the cohesion and the friction angle. As the goal of this work is calculating slope stabilities, the role and scale of the resisting forces is well signified by directly using the shear strength as input to the stability calculations. Though with this handling the exact figures for cohesion and friction angle were not determined, which can be bypassed given the scope of this work, appraisal for these values can be approximated by measurements of samples from the Kugmallit Channel, with friction angle and cohesion for the locations Tuwak and Kekertak correspondingly 29.3° and 4.8 kPa and 25.4° and 2.1 kPa, as reported by Blasco et al. (2013).

3.4. Temperatures

The acquired sediment temperature profiles are closely related to the parameter thought to be the most sensitive to environmental change, namely the heat content of the regional water masses, especially the bottom water temperatures. Similarly to the CPT data, these profiles have a rather limited sediment penetration (<2.5 m), but nevertheless represent a quite relevant dataset.

Water temperatures:

The general trend of the obtained sediment temperatures roughly agrees with the bottom water temperatures. Concerning the water temperatures, from the sea surface down to ca. 600 – 700 m water depth, they progressively increase (average of approx. 0.002°C/m in the interval; coldest temperatures found at sea surface), and below ca. 700 m the temperatures start to increase downward. Also noteworthy is the considerably higher temperature variation (-1.5 to 0.5°C, downward) seen between about 170 and 350 m water depth - approx. 0.01°C/m in the interval (**Figure 33** and **Figure 34**).

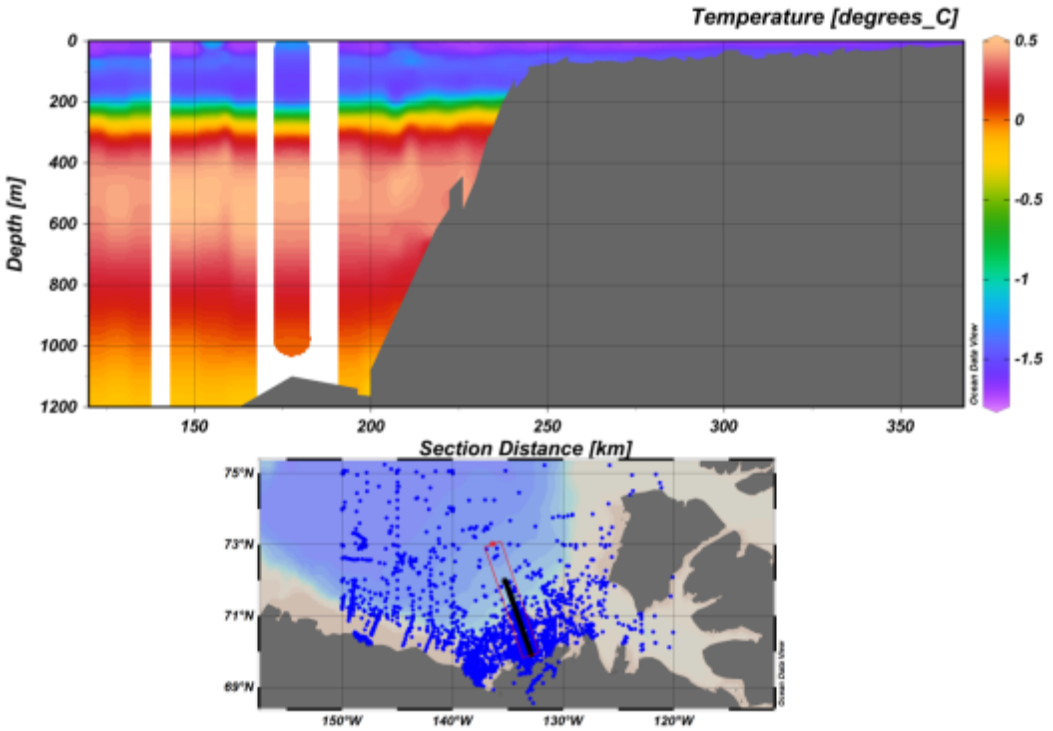

Figure 33: Water column temperature profile down to 1200 m water depth of the transect correspondent to the black line in the map (NOAA; Schlitzer, 2014).

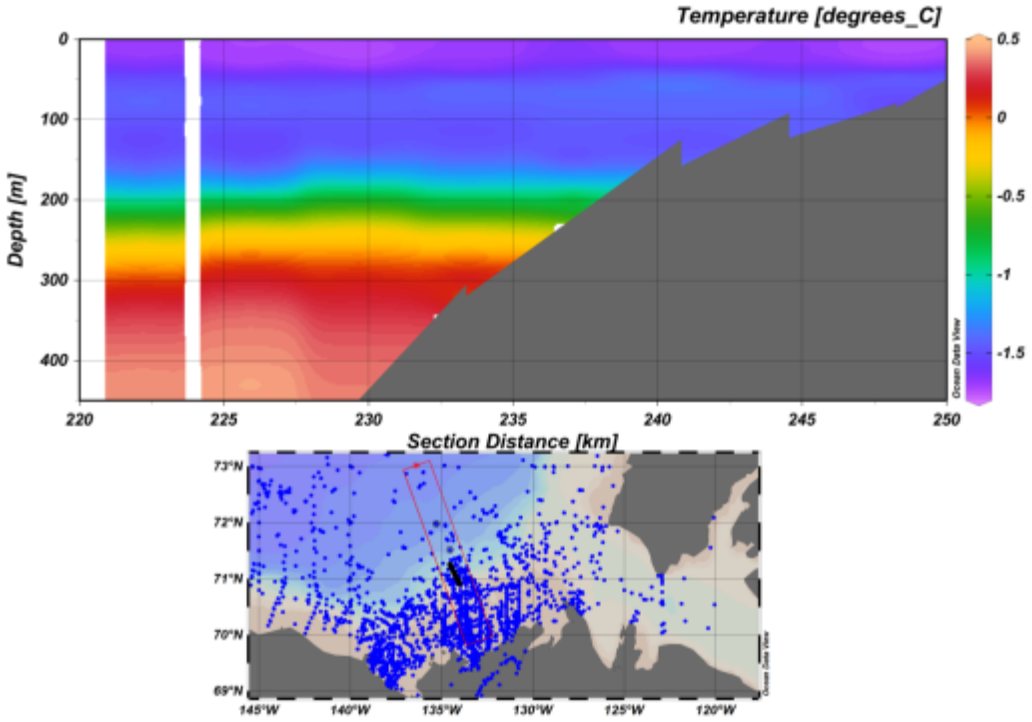

Figure 34: Water column temperature profile down to 450 m water depth of the transect correspondent to the black line in the map (NOAA; Schlitzer, 2014).

Sediment temperatures:

(Relative location of transects can be seen in **Figure 10**)

The locations probed for sediment temperatures on the Eastern Shelf (**Figure 69**) show a pattern in which almost all the probed sites present a temperature increase in the first 0.7 mbsf, from -2 to -1.3°C; below which point the temperature remains constant until the end of the profile. The exception is STN 03, which has generally higher temperatures (even reaching a positive value at 0.7 mbsf), also has a temperature increase in its first 0.7 mbsf (ca. -0.2 to 0.05°C) and downward decreases and stabilizes at ca. -1.7°C. One possible reason for the different behavior of STN 03 could be its deeper location.

In Western Canyon transect, where all the measured temperatures are positive, a discreet overall trend of temperature decrease associated with deeper water depths of the sampling positions can be noted. General variability of temperatures in this area is modest, ranging between 0.24 and 0.4°C. The two deeper stations (STN 31 and 32 – also at about the same water depth, 686 m) have just about the same temperature profile. Stations 34 and 35 present a downward sediment temperature increase, although they show rather constant values between 1.3 and 1.8 mbsf. Profiles of STN 31 and 32 show nearly constant temperatures (ca. 0.25°C) between 0.8 and 1.3 mbsf, with values increasing to 0.37°C at the bottom of the profiles. Station 33 has the most particular of the profiles in this area, with temperatures dropping (from 0.27 to 0.24°C) between 0.8 and 1.3 mbsf and rising below that point, reaching a maximum of 0.32°C.

The sediment temperatures taken from the Northern Canyon (**Figure 37**and **Figure 71**) reveal a general trend of rising values with increase in depth below sea floor, though between about 1.5 and 2 mbsf all the plotted curves see a change in trend, with the rate of temperature increase with depth either reversed (STN 68, 70, 71 – all located below apparent head wall of mass wasting) or being constant (STN 67 – above head wall). This observation could be sign of a significant change in properties (e.g.: fluid content, thermal properties, hydrates presence) at the mentioned sediment depth interval. Moreover this group of stations is at relatively elevated water depths, between 740 and 870 m.

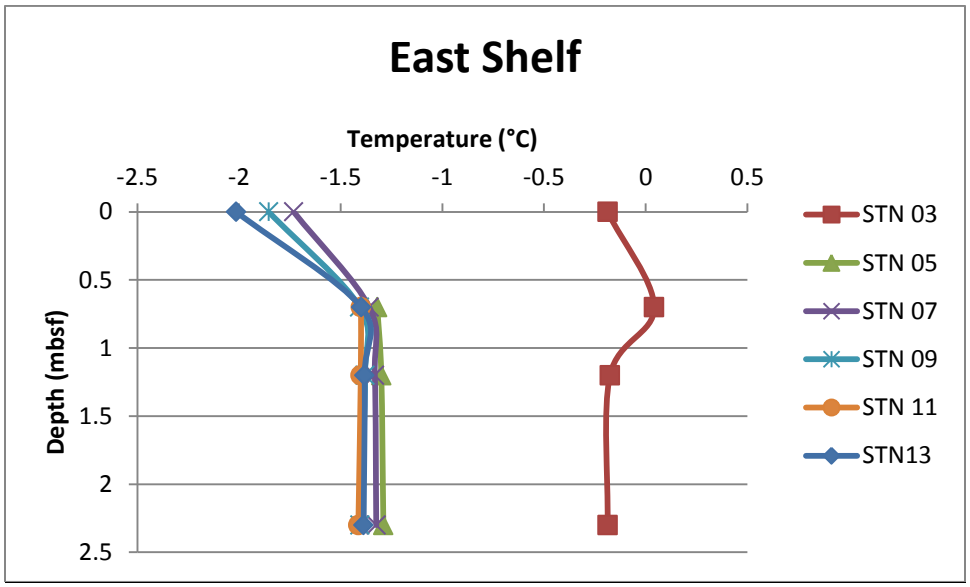

Figure 35: Subsurface temperature profiles of the Eastern Shelf (profile positions are found in Figure 69).

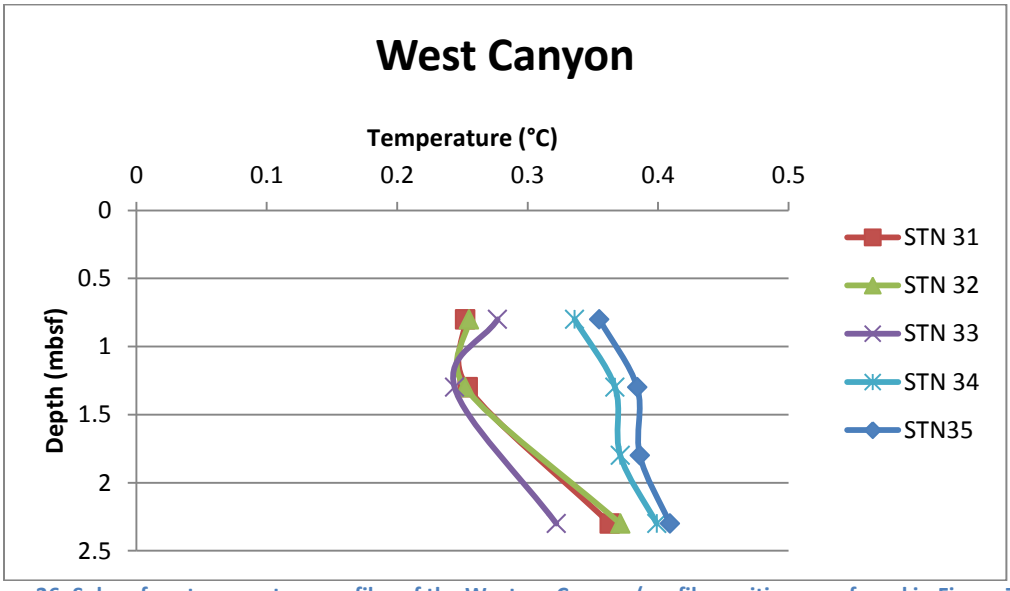

Figure 36: Subsurface temperature profiles of the Western Canyon (profile positions are found in Figure 70).

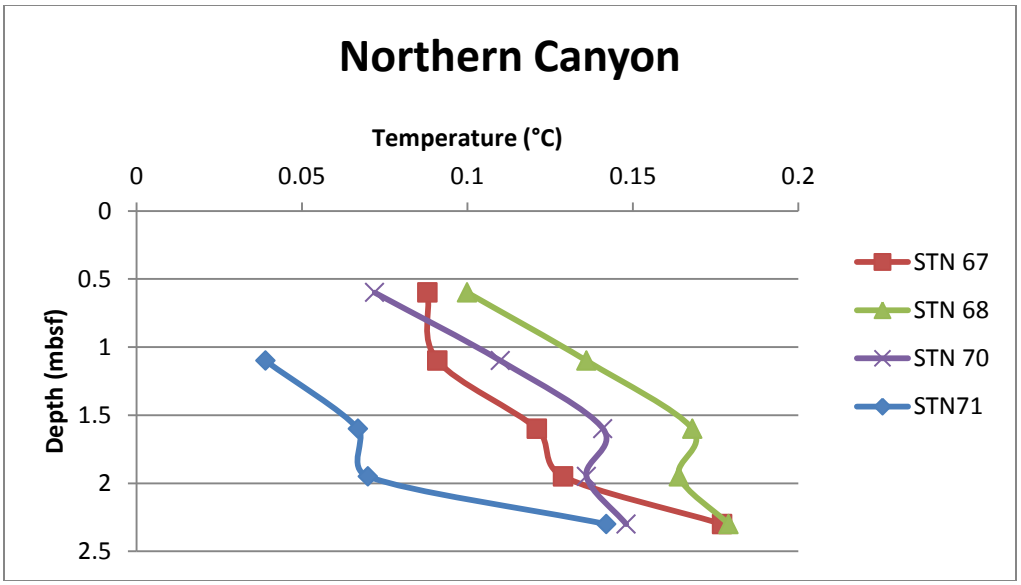

Figure 37: Subsurface temperature profiles of the Northern Canyon (profile positions are found in Figure 71).

At the Central Shelf the sediment temperatures give a rather particular set of profiles (**Figure 38** and **Figure 72**). The two deepest profiles (STN 81 at ca. 230 m and STN 83 at 210 m water depth) show an opposite trend compared to the other three in this area, with temperatures generally dropping (profile SNT 81 going from positive to negative values) at two general rates: a higher one down to about 1.3 mbsf and a lower one from this point downward. These two profiles also show the highest measured temperatures at the Central Shelf.

The other four profiles (STN 85, 87, 89 and 91; all water depths shallower than 190 m) could be briefly described as somewhat dissimilar from one another. STN 85 has arguably the most erratic curve, alternating between rise and drop downward until 1.8 mbsf and then further rising in temperature to a maximum of ca. -0.6°C. STN 087, the shortest profile only starting at 1.3 mbsf, shows a small temperature decrease until 1.8 mbsf which then changes to a maximum of -0.5°C. STN 89 gives a temperature increase down to 1.3 mbsf (peak of -0.7°C) then dropping to about the same temperature it has nearest to the sediment surface (ca. -0.9°C)and stabilizing down to its end. Lastly, STN 91 presents a quite gentle temperature decrease down to about 1.8 mbsf (from about -1 to -1.1°C) and then reverses to an increase until its bottom (2.3 mbsf) reaching a maximum of ca. -0.8°C

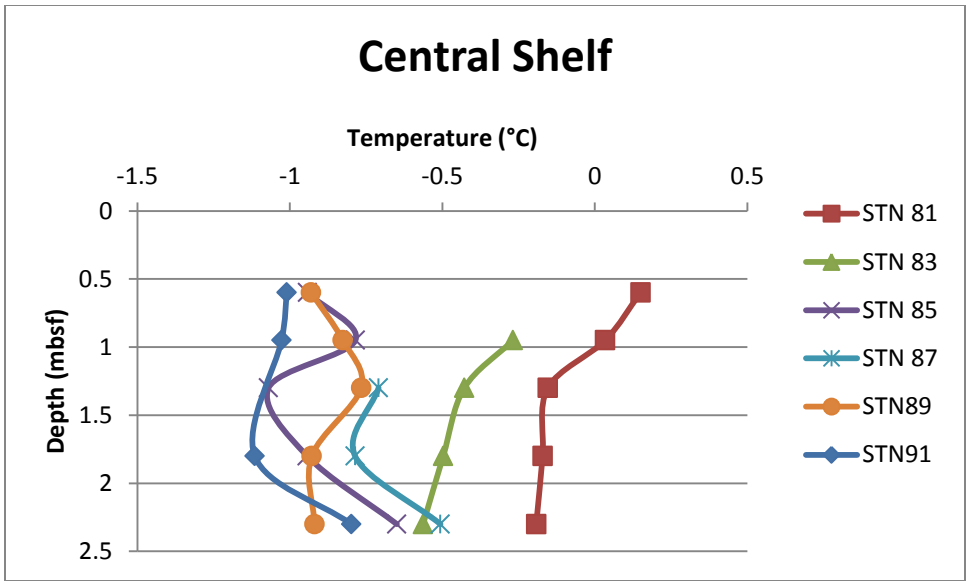

Figure 38: Subsurface temperature profiles of the Central Shelf (profile positions are found in Figure 72).

Observing the water temperature profiles (**Figure 33** and **Figure 34**) an interesting pattern emerges, showing rather well defined thermal zonation. When confronting these profiles with the measured top sediment temperatures, it results that sediment temperatures for the **Central Shelf** (**Figure 72** and **Figure 38** -between 100 and 200 m water depth)range between ≈ **-1.0°C** (**STN91**, ca. **170 m** water depth) and **0.1°C** (**STN81**, ca. **230 m** water depth), and for the **Eastern Shelf** (**Figure 69** and **Figure 35**) the temperatures vary between **-2°C** (**STN 13**, **90 m** water depth) and ≈**0°C** (**STN 03**, **235 m** water depth). The correspondent bottom water temperatures for these locations are ≈-**1.4°C** (**100 m** water depth) and -**0.6°C** (**200 m** water depth - note the temperature increase with depth).

At deeper locations (700-1000 m), the comparison of sediment and water temperatures (**Figure 71**, **Figure 37** and **Figure 33**) reveals for the **Northern Canyon**: sediment temperatures of **0.08°C** for **STN67** (ca. **750 m** water depth) and **0.03°C** for **STN 71** (**865 m** water depth) and bottom water temperatures of **0.3°C** at **700 m** and **0.2°C** at **810 m** water depth. For the **Western Canyon** (**Figure 70** and **Figure 36**), the sediment temperatures range between **0.2°C** (**STN 31**, ≈**690 m** water depth) and **0.4°C** (**STN 35**, ≈ **570 m** water depth), with about the same bottom water temperatures.

This set of observations indicates that, considering the given water temperatures and the resulting extended gradient, the sediment temperatures seem to be in an approximate thermal equilibrium (at least in the assessed subsurface) with the water column.

3.5. Calculations

With the **Equations** previously described, calculations were realized using the produced physical properties. The generated results were developed for individual positions, due to the very nature of the input information and its various acquisition techniques. Naturally, the relevance of the results is proportional to their applicability to reasonably broad areas, in the scale of phenomena that would not be negligible. Based on generally accepted scientific principles and discretion, the results here given are considered to be applied to their adjacencies at least as rather sound approximations. Different scenarios were constructed, with the central variable being the sediment temperature. Temperature increments were progressively applied, with the focused consequence being the effect on GH stability and subsequently the change in the Factor of safety of different slopes. The main aspect here considered for the relationship between GH stability and slope instability is that the dissociation of each cubic meter of methane hydrate produces about 164 m^3 of gas (Nixon & Grozic, 2006), consequently causing overpressure and potential slope failure. Though several parameters were used in the calculations (as shown by the required variables of the used **Equations**), the ones that appear to be most influential in the outcomes are water depth, temperature, slope angle, cohesion, porosity and friction angle of the material in question.

Calculations of the permafrost stability in response to temperature changes were performed having as basic principle that of water phase boundaries as constrained by salinity, pressure and temperature (Fofonoff& Millard, Unesco, 1983). From these calculations it is assumed that if water ice would not exist at a certain location, IBPF would not be a possibility. Therefore the passage from conditions where water ice is calculated as stable to conditions where this is not true is naturally considered as a passage that leads to PF thawing.

The outcomes of the calculations regarding the stability of the PF initially show that the available sediment temperatures (section **3.4**) and correspondent hydrostatic pressures and salinities (Schlitzer, 2014) fall into the stability of subsea ice just in the shallowest data points of the Eastern Shelf stations (STN09 and STN13 – considering the provided sediment temperature profiles reliable), essentially at the water-sediment interface. To be noted that the lowest temperatures in this area are found at the top of the thermal profiles, especially in the shallowest stations (**Figure 35**). Associating this finding with the determination of **Subsea Permafrost** in the Beaufort Shelf, it can be conjectured that the ice bearing sediments in other portions of the Shelf are located deeper into the sediment (beyond the reach of the temperature profiles used in this work), where colder relict conditions are to be found.

To estimate at which temperatures PF would be present in other positions, progressive temperature subtractions were here simulated, resulting that different areas of the Beaufort Shelf find ice stability at different temperature dips (assumed to exist deeper into the sediment; Figure 40). Discounting 0.45°C, the top sediments of STN 111 (115 m water depth; South of the SW Slide, on top of the Shelf) enter ice formation conditions. At about the same drop (-0.45°C) deeper sediments of the Eastern Shelf (below the already ice-stable top) begin to freeze. With the drop reaching -0.5°C the full profiles of STN 09, 11 and 13 reach ice stability (all shallower than 110 m water depth above the shelf break) where the inferred pinching out limit of PF occurrence is thought to be. A change of -0.6°C makes all the data points of STN 111 and 113 prone to ice formation. Thus, A and B in **Figure 39** indicate where PF is expected to be found closest to the seafloor, considering the thermal gradient of the upper part of the Beaufort Shelf in **Figure 40**. Stations at depths below that of the nearest Shelf Break (100 to 120 m water depth), such as those from the Central Shelf (which has relatively high slope gradients) were not considered since even though they could be simulated to reach ice stability such results would not be supported by previous studies (geophysical, drillings and paleo climatologic), which affirm that the PF extension is limited to the Beaufort Shelf (**Figure 39**).

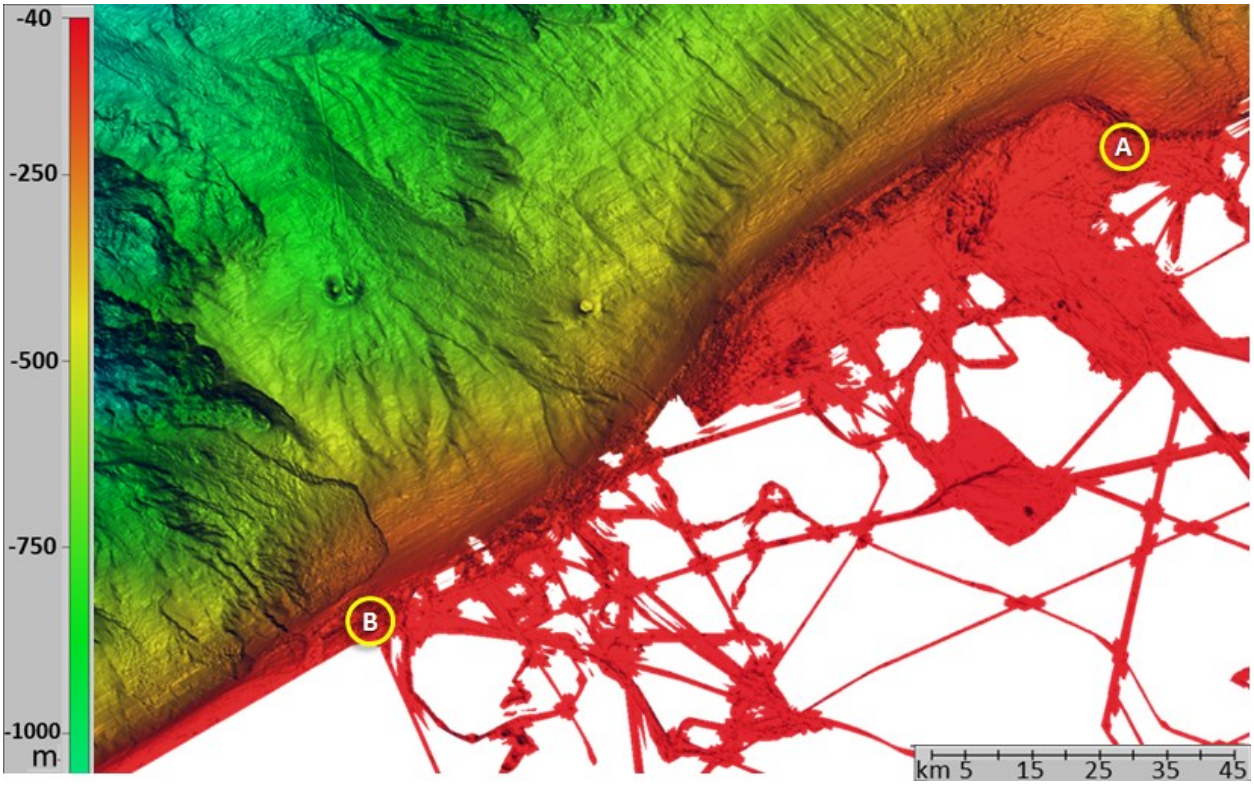

Figure 39: Locations on the Beaufort Shelf where ice stability is estimated as colder(relict) sediment temperatures reach lower values with depth. (A) represents the approximate location of STN 09, 11 and 13 on the East Shelf and (B) indicates the STN 111 and 113 at the South of the SW Slide.

4. Discussion

4.1. Climate change forecasts

The well-established climate balance and forecasts presented by the Intergovernmental Panel on Climate Change (IPCC) is the primary mean to understand the level of environmental variability concerning the Arctic region. In the report it is found that due to natural processes and, with an arguably greater extent and likeliness, anthropogenic influence, environmental conditions are to be perturbed at a global scale with, among other consequences, projected general temperature rises.

As an effect of Polar Amplification[2] the Arctic region is expected to warm faster than other regions, in effect this region is projected to warm the most, with 'very high confidence' stated for such a forecast (IPCC, 2014). In simulations, Arctic zones (north of 60°N latitude) were projected to warm at a rate of 1.36°C per century, nearly twice as fast as the global average (Bekryaev et al., 2010). Besides for the expected temperature hikes, other important consequences of this process are shrinking and thinning of Arctic sea ice cover, disrupted precipitation patterns, decrease of surface permafrost, change in water salinities and modification of oceanic currents (IPCC, 2014).

The available data, from about the year 1800 to the present, shows that significant changes in sea-ice quantity and temperatures have already happened. Because of lags in reaching equilibrium conditions, it is said that the existing oceanic circumstances still have not fully absorbed the climatic variations from the recent past (century scale). Therefore, the climatic phenomena in question correspond to an ongoing process, presently and continuously amplified by anthropogenic environmental influence.

This described climatic context comes about in parallel to the introduced thermal pulse at play in the Beaufort Sea since the last marine transgression episode.

4.2. Temperature changes and permafrost thawing

Given the referred occurrence of PF in in sediments of the Beaufort Shelf (***Subsea Permafrost***), this is inherently the only portion of the study area that could suffer consequences from its thawing. With a focus on the uppermost sediment layers, which are intuitively also the most sensitive to bottom-water

[2]Polar amplification takes place if the level of regionally averaged surface temperature variation at high latitudes surpasses the globally averaged temperature change, in reaction to climate forcings and on time scales greater than the annual cycle. This phenomenon is of global concern due to the likely effects of future warming on ice sheet stability and, accordingly, global sea level and carbon cycle feedbacks like those related to permafrost thawing.

temperature variations, it is possible to note that the water temperatures in the interval where near-surface PF occurs are rather low when considering the broader water column temperatures (**Figure 33** and **Figure 34**). This observation already hints to aconceivable vulnerability of the ice-bearing sediments in question to either changes in general water temperatures or to some kind of rearrangement of oceanic water masses and currents, particularly when considering the hypothesized effects of ccontemporary climate change trends as reported by the IPCC. For the purposes of this study, detailed effects of climate change will not be discussed, though it will be considered that such climatic transformations are possible and could significantly influence the region here under scrutiny.

To be noted is the spatial separation of areas where PF and GH are present in the most superficial sediments, as PF only occurs at its deepest around the shelf break (≈100-120 m) and GH are stable roughly below 200 m of water depth – reminding that these two do seem to coexist in deeper sediments (**Figure 7** and **Figure 40**). Therefore PF thawing and GH dissociation would occur in different areas, which is why they are treated separately in this thesis.

When it comes to the regional extent of PF in the Beaufort Shelf (**Figure 51**), Frederick and Buffett (2015) argue that a decisive factor is the role of the local hydrology on temperature and salinity. From numerical modelling they fundamentally infer that the saltwater-fresh water boundary practically corresponds to the limits of the detectable PF and, as fresh water can in practice conserve relict ice, greater amounts of (fresh) groundwater discharge may favor a broader extension of the PF. The main local source of fresh water is the McKenzie River.

Of the temperature profiles available to the development of this thesis, only two of them have pressure, salinity and temperature conditions that would be liable to the presence of ice in the sediment. These locations are at the Eastern Shelf transect (STN09 and STN13, respectively in the middle of the slope at 110 m water depth and on the shelf at 90 m; **Figure 69**). In both cases the subseafloor depths have been calculated to be susceptible to bear ice are quite close to sediment-water interface (within 0.5 mbsf). Curiously, STN11 (between the two mentioned, at 105 m water depth) does not seem to also have water freezing conditions. In calculating the stability of water ice in the sediment, after adding progressively higher temperature increments (pressure and salinity kept unchanged), the ice becomes unviable at STN09 and STN13 after an increase of 0.1 and 0.2°C respectively.

Though these arguably narrow temperature intervals and small number of data points suggest the presence of ice-bearing sediment, it must be pointed out that PF has been inferred to pinch out at the

shelf break (with its deepest occurrence roughly between 100 and 120 m below the water table). When accounting for this factor, it can be contended that the observed subsurface temperature data points (those that are close to or at slopes) barely overlap with the subsea PF, at best coinciding to its outer limits. Additionally, a coarser approximation exercise considering regional average values of water parameters at 100 m water depth (salinity of ≈32.6 psu, from Schlitzer 2014) says that water ice would occur at ca -1.8°C, which is colder than the bottom water of ca. -1.5°C (as reported by the average regional values), making ice not viable at these conditions. Consequently, the geophysically inferred PF should occur deeper into the sediment and down the slope (added to the points at the East Shelf mentioned as already ice-stable), where relict temperatures and salinities compatible with ice existence are possibly preserved. In general, at a larger, deeper scale, as seen in **Figure 40**, the sediment temperatures at the Beaufort Shelf get colder down to about the first couple hundred meters, making ice bonding at depth more likely.

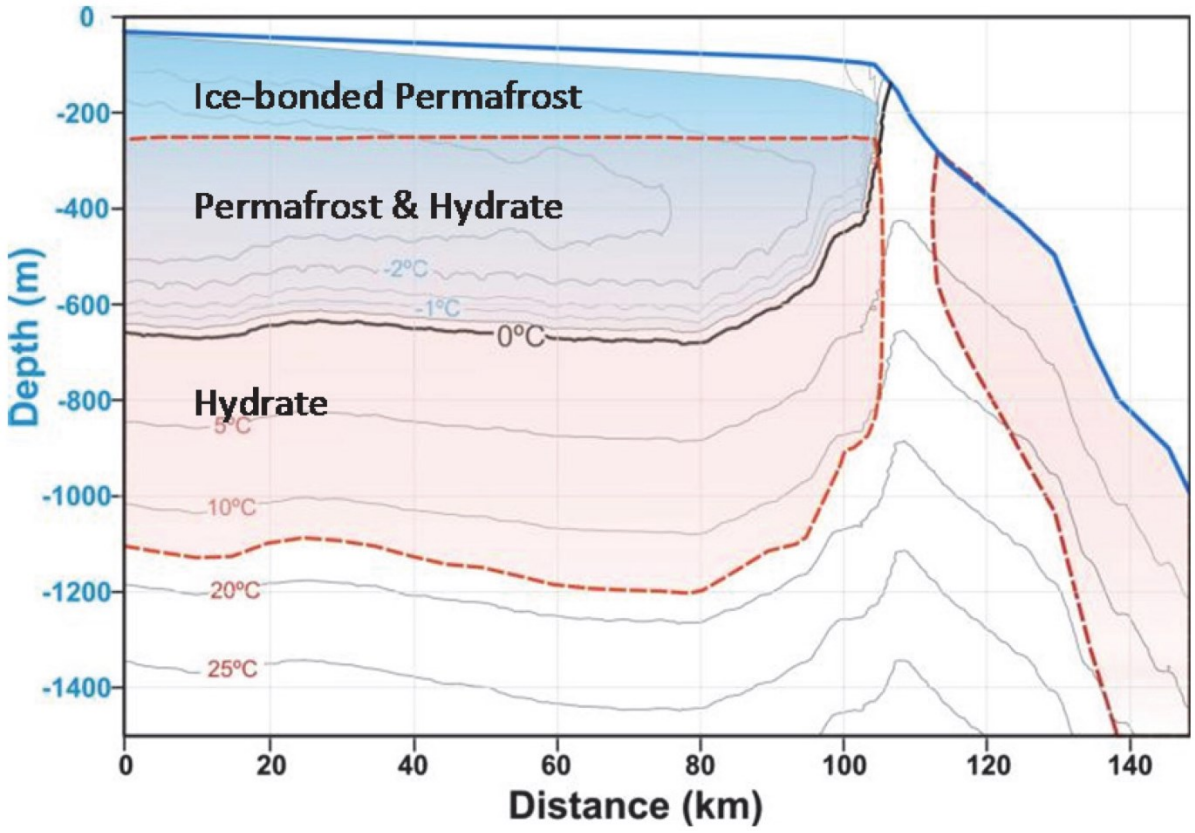

Figure 40: Modelled cross-section scheme of: ice-bonded permafrost, permafrost-associated with GH stability field and deep water marine GH stability field through the Beaufort Shelf (Jin & Riedel, 2014). Blue line indicates the seafloor, red perimeter gives GH stability limit, black line represents the 0°C boundary (coinciding with the permafrost extension) and grey lines represent the isotherm contours.

4.3. Permafrost thawing and slope stability

Since permafrost-bearing sediments have their pore space and fissures partially filled by ice veins that support in some measure the overburden load, a broad range of effects can be observed. Such sediments to possess markedly heightened compressive and shear strength as well as lower porosity and permeability than their unfrozen correspondents. Additionally, as the overburden load is kept from being fully absorbed by the sediment itself, the process of normal consolidation can be largely inhibited, resulting in under-consolidated sediments. Consequently, the thawing of such sediments (and the ensuing strength deterioration) in slopes might result in severely weakened intervals that should be more prone to strain deformation and failure. The disruption of PF can also result in loss of sediment strength from the release of pore water, leading to over-pressure (Ruffel et al., 1988, Paull et al. 2007, Jin & Riedel, 2014).

Though the calculation of precise values for the loss of shear strength in sediments that undergo PF thawing areas is not pursued in this work, the appraisal of locations where such thawing could occur in consequence to given increases in temperature is. Estimating whether thawing would or not occur is here based on the computation of water-phase boundaries constrained by salinity, pressure and temperature (Fofonoff& Millard, Unesco, 1983). The motivation for this approach is that the loss of ice-bonding by itself reduces the material strength properties enough to put an involved slope area at substantial failure risk.

The results illustrated in section **3.5** indicate that within the depth reach of the available subsea temperature profiles, PF is not to be found (except for the top of STN 09 and 13), but from **Figure 40** the geothermal gradient of the first couple hundred meters of the shelf sediment appears to decrease downwards, hence making PF possible deeper down (for temperature variations given in the **Calculations** section). From this observation it is considered that the risk of slope failure from PF thawing is plausible if sediment temperature increases at depths were the PF is currently stable. Sediment depths with stable PF (where the temperatures are low enough for ice formation) are speculated to be below 2.5 mbsf.

4.4. Temperature changes and GH dissociation

Of the variables responsible for controlling GH stability, the one most likely to be considered to suffer important alteration is the temperature. The currently well publicized climate change trends are here considered to represent a realistic mechanism to induce thermal change effects, especially concerning the implications of altered oceanic heat content and pathways of oceanic currents, all aggravated by the Arctic region being expected to most dramatically suffer such climatic consequences (*IPCC*, 2014). From this perception, the key trigger to GH dissociation in sediments is the temperature increase derived from the water column.

Based on the described regional context for ***Subsea Gas Hydrate***, **Figure 7**, **Figure 33**, **Figure 34** and **Figure 40**, it can be observed that the presence of GH on the first meters of sediment is of significance on the Beaufort Shelf at water depths of about 230 m or more, which is also a depth range correlated with a temperature increase in the water column, down to ca. 700 m, where water temperatures begin then to decrease downward. If other factors for the presence of GH (e.g.: manifestation of gas, salinity) are favorable, the dissociation of GH from warming would - in the considered scenario - take place initially in sediments at the top of the stability zone (which could even be right at the seabed), with the consequent released fluids possibly being: a) trapped (conceivably accumulating pressure), b) dissipated into the water column or c) migrating through sediments and eventually following one of the previous prospects. The available documented stratigraphy, geophisical surveys and direct measurements strongly suggest that the sediments of the concerned region have, most relevantly in the described Unit A (**Figure 5**), alternated layers of material with porosity and permeability differences conducive of fluid migration and trapping.

4.5. GH dissociation and slope stability

The dissociation of GH produces a release of both fresh water and free gas (Sultan, 2007). If the expected higher bottom water temperatures take effect, the dissociation of previously stable GH should provide enough fluids to decrease sediment structural strength and induce overpressure, that if allowed by sediment characteristics such as a requisite stratigraphy, porosity and permeability. Concerning the changes in sediment properties, when hydrate dissociation takes place higher GH contents induce progressively higher losses in slope stability, with soil properties and slope geometry as key factors in determining how the material would behave in the case of GH dissociation. The effects of stability loss are more severe if the hydrates are near the up-dip limit of their stability zone and at shallower waters –

lower pressures allow for greater gas volume/mol. In addition, void ratio and plasticity index have a particularly significant impact on the slope stability, with void ratio limiting the conceivable amount of GH per volume of sediment and the plasticity index determining how much deformation can be sustained (Nixon & Grozic, 2006). The argued temperature rise forecasts for the Arctic region point towards a general reduction of the GHSZ at its top, therefore the destabilization of GH could result in the intensification of mass wasting episodes (**Figure 41**).

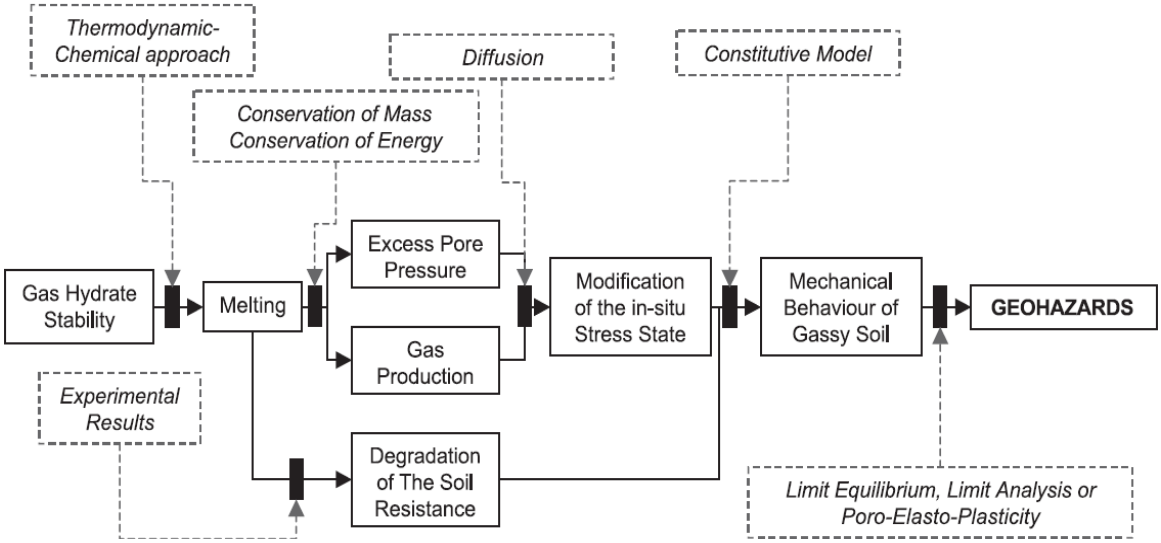

Figure 41: Flowchart connecting gas hydrate melting and geohazards (Sultan et al., 2004).

The processed CPT of STN 92 gives an example of a set-up prone to the effects of stability loss from GH dissociation. Observing the plots of the measured geotechnical material properties (**Figure 42** and **Figure 43**) we can identify at ≈ 0.9 mbsf a transition characterized by:

- Peak in sleeve friction (fs);
- Sensitivity reaches a minimum and increases downwards to a peak at about 0.95 mbsf, after which it decreases again;
- Undrained shear strength surges (at 0.9 mbsf) reaching a considerable maximum at about 0.95-0.97 mbsf. Values range from about 10 to 50 kPa.
- Cone resistance follows the same pattern of the undrained shear strength, with values from ca. 160 to 590 kPa.
- By 0.7 mbsf sleeve friction begins to rise (downwards) at a higher rate than above, reaching a maximum at 0.9 mbsf (approx. from 5 to 12 kPa), after/below which it quickly decreases back to the levels of 0.7 mbsf, until at about 0.95 mbsf it begins rising again.
- Excess pore pressure is practically constant (ca. 20 kPa) until about 0.87 mbsf, at which point it quickly reaches a peak (40 kPa; at 0.875 mbsf), and after this peak it decreases.

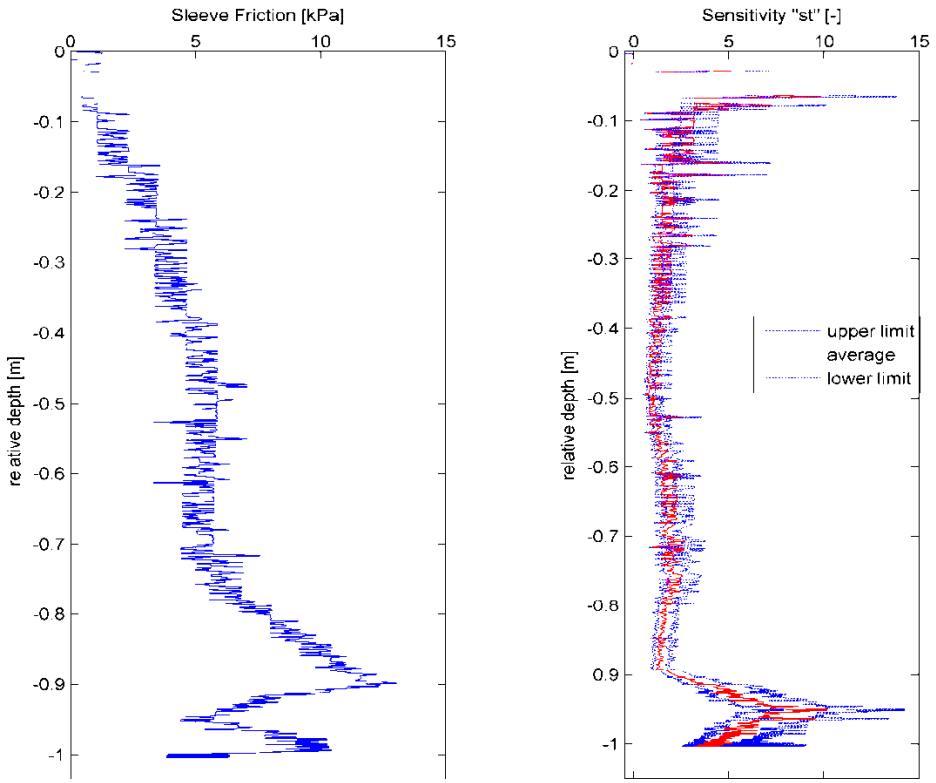

Figure 42: Sleeve friction and sensitivity plots from CPT STN 92.

This series of observations indicates a downward passage from lower to higher permeability and porosity. This sort of transition favors a mechanism in which the lower, more porous and permeable layer transports and accumulates the fluids released from GH dissociation, which would be trapped by the upper more impermeable layer. That could result in overpressure, loss of structural stability and eventually, slope failure. The limits of CTP penetration into the sediment hinder a precise characterization of deeper sediment portions, nevertheless the available **SBP**, and the study of the **Stratigraphy and Structure** of the region allow to infer that the sort of sedimentary transition exemplified in STN 92 is conceivably found at adjacent points of the Beaufort Shelf and Slope and feasibly repeated through the upper stratigraphic Unit A (Blasco et al., 2013).

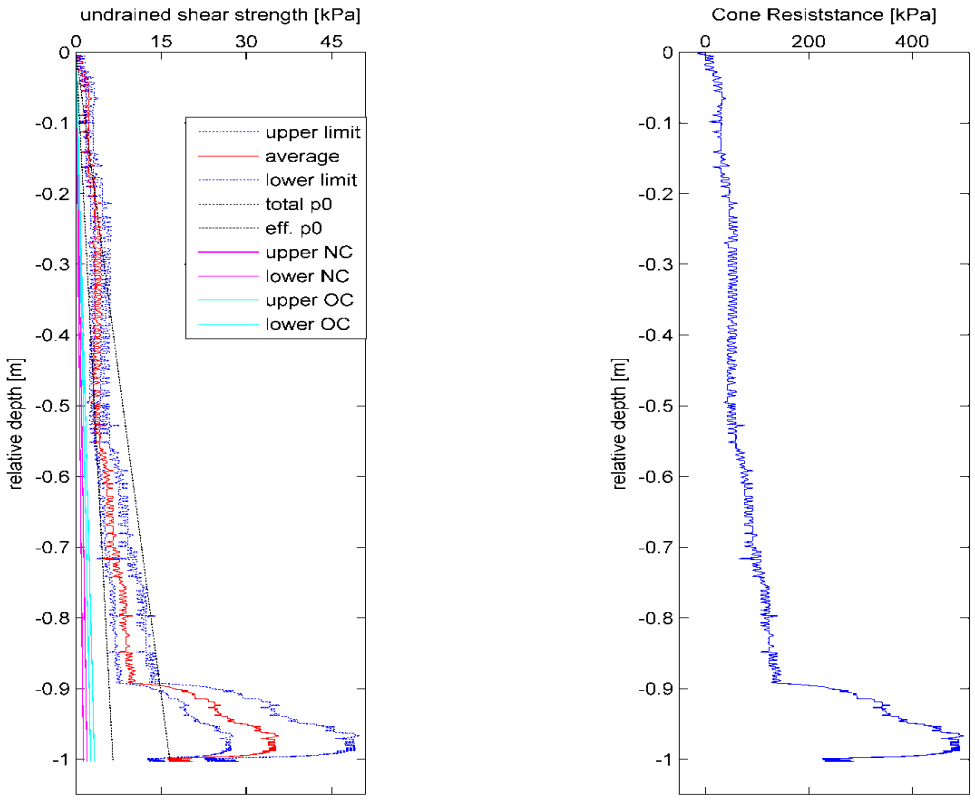

Figure 43: Undrained shear strength and cone resistance from CPT STN 92. NC: normally consolidated; OC: Over consolidated.

The SBPs of **Figure 20**, **Figure 21** and **Figure 22** typify the parallel nature of the deposited layers, an important factor especially at the slope, since due to the slope angle itself the upward migration of low-density fluids from destabilized GH could plausibly accumulate (e.g.: where strata pinch out or in anticlines of folded strata) and create conditions for overpressures that could overcome the static load, eventually undermining the local stability.

Shifts analogous to that described on the CTD of STN 92 (admitting tolerable differences) are found in the profiles of STN 12 (≈0.5 mbsf), STN 114 (≈0.4 and 0.7 mbsf) and in a more gradual manner in STN 86 (from top to ≈ 0.6 mbsf) and STN 116 (≈ 0.5 mbsf) (**Figure 29**, **Figure 30**, **Figure 31** and **Figure 32**).Having the SBP ARA05C_ag (**Figure 25**) as representative of a type of geometry predisposed to slope failure, the following can be remarked. Regarding the general topography, it can be seen that the position of the head scar itself is at a point where the slope goes from relatively steep to nearly flat. Based on other profiles crossing the Beaufort Shelf and Slope, the outline of the sub bottom reflectors is practically parallel to the seabed, leading to the presumption that it was also the case of the reflectors in the SBP ARA05C_ag before the deemed mass wasting. From this, it becomes safe to think that the failure occurred where the reflectors (thus arguably the strata) transitioned uphill from steepened to flat (or

even slightly dipped in the opposite direction, which in the context of buoyant fluid release from GH dissociation (i.e.: gas) could represent a zone of preferential overpressure accumulation, ultimately overwhelming the overburden pressure and destabilizing the slope. This general type of geometry is found throughout the Slope-Shelf transition, feeding concerns that other areas of the region could be threatened by disruption of the top of GHSZ.

The resulting calculations indicate that a sediment temperature increase of ≈ 1°C would promote GH dissociation and slope failure in the areas marked in **Figure 44**, where the center of the radial color gradient match the points where data (e.g.: subsurface temperatures and CPT) were available and the fading towards ends of these areas represent the loss of certainty rooted on data scarcity. Inferring from the data at hand, it is deduced that the entire slope area would be passive of GH related mass wasting, but cautiously, as seen in **Figure 44**, the area marked by the yellow dotted perimeter to the SW was not asserted to suffer such effects because of the lack of temperature data at the slope, hence not allowing a dependable estimation of the GHSZ and the computing of its disruption. Other portions of the study area were also estimated to endure the referred effects of GH destabilization, particularly the West and North Canyon (**Figure 10**, **Figure 70** and **Figure 71**), but these outcomes were calculated to develop at rather high (thus less likely)temperature increments, of ca. 8°C.

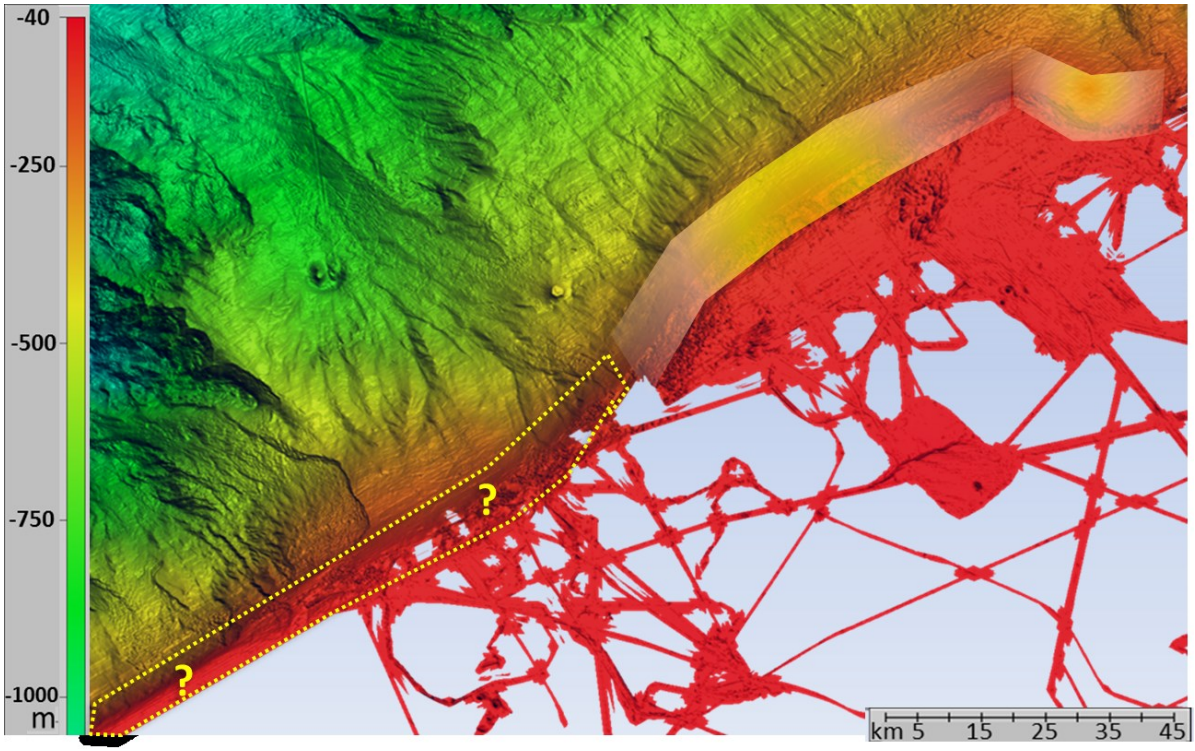

Figure 44: Areas where GH dissociation is calculated to occur with a sediment temperature increase of ca. 1°C. The radially gradient colors of the two NE areas indicate the loss of certainty from the center to the edges. Dotted yellow line marks a zone where the same kinds of effects as described for the gradient-colored perimeters are expected, but no such results were obtained in the calculations due to limitations in data coverage, hence lacking reliability.

The areas regarded as prone to failure are, besides for the performed calculations, defined based on the availability of data. The whole slope seems to be subject to mass wasting from GH destabilization, but due to caution based on the coverage of the available data this assumption is not patently expressed in **Figure 44**, where the shelf areas around the yellow interrogation marks represent the uncertainty – for instance, in the South of Slide (around STN 111 and 113) slope destabilization was not asserted because the data points are all above the shelf (none on the actual slope), therefore not providing enough information to estimate slope failure on the slope below.

4.6. Size of possible mass movements

Taking into account the so far explored aspects of the study area, assessing the potential size of future mass wasting events is in this thesis done mainly based on the type of interval found on the CPT and on the SBPs. Even though the construction of such estimations is exposed to many uncertainties, it is here attempted. If dissociation or thawing occurs at rather trivial sediment depths in an interval where there is no relevant transition from a lower to a higher permeability layer (which could make fluid trapping, migration to areas with more important overlying sediment thickness and overpressure accumulation plausible), the fluids should simply be released into the water column, perhaps with some superficial sediment disturbance.

The type of interval described by the CPT profile STN 92 (**Figure 42** and **Figure 43**) is of the kind that should represent a considerable risk to slope stability, and the amount of sediment found above it would correspond to the mobilized material, which is observed to vary among the shown profiles between roughly 0.4 and 1 mbsf. Considering the SBPs and the introduced regional stratigraphy, a succession of such type of interval is conceivably repeated through the top stratigraphic unit (**Figure 5**). Therefore, if GH dissolution occurs gradually from the top to the bottom strata, it is expected that the dissociation provokes gas to be released within the more permeable layer and trapped by more impermeable layer above, and, as soon as the overpressure is sufficiently accumulated to overcome the static load, slope destabilization would occur, displacing a volume of material corresponding to the presumed 0.4 – 1 m overlying sediment. In this scenario several somewhat regular and considerably modest mass wasting events are presupposed (depending on the thickness of the discussed sedimentary alternations and such).

Here it is cogitated that the incidence of more massive slides (involving sediment thicknesses greater than that of the top impermeable-permeable layer transition and of course triggered undermining the

top of the GHSZ) would require a circumstance in which the production of gas from GH dissociation occurs downslope, deeper into the sediment position and the generated gas migrates upslope through the mentioned type of permeability-related sediment alternations. The accumulation of overpressure could then build up below thicker sediment packs and, given the larger static load, considerably higher overpressures would have to be accrued in order to promote slope failure. Such larger pressures would then need longer periods of time to mount up. In this kind of scheme mass wasting events would be more prominent and happen with larger temporal hiatuses than in the previous case. Alas, a reasonable mechanism that would yield such instance failed to be conceived in this dissertation, thus being deemed less probable.

Another proposed mode for slope destabilization is one in which gas produced within the sediment downslope migrates all the way to the shelf break, around the area where PLFs occur, not being trapped and feasibly causing gas bubbles to emanate from the seafloor. The emission of bubbles would disturb the top sediments, which could be energetic enough to jeopardize the slope integrity. In this hypothesis the involved sediment thickness is tougher to determine, given the uncertainty in the amount of gas involved and in the intensity of its discharge.

The lateral scale of the theorized material displacements is here seen to be highly passive of error due to the limited and somewhat scattered nature of the used datasets. However, generalizing and deducing from the data, it is here thought that the gas production from GH dissociation, the isotherms (and their eventual temperature shift) and the thickness and physical properties of the different sediment layers (which should also be rather continuous) should be fairly homogeneous, at least within a certain sub region (e.g.: East, Central Shelf). Accordingly, the potential slope failure is cogitated to laterally extend at the scale of the full size (or substantial segment) of a specific sub region.

From the discussed in section **4.3** and based on the data at hand, PF thawing related slope failure would be less likely to occur due to the thicker (>2.5 m) sediment interval that would have to be incrementally warmed to cause PF thawing (except for the top of STN 09 and 13), that is, to reach the PF occurrence zone. Nevertheless, in the case of sufficient thermal increment in the sediments, destabilization of the shelf edge from PF thawing would involve volumes of material thicker than 2.5 m. It must be said that data coverage is limited and a denser and broader dataset might contradict what is stated here.

4.7. Error assessment

The results attained in this work are inescapably subject to errors, possibly stemming from several sources such as equipment malfunction, faulty calibration, sample disturbance or simply mishandling during sample or data acquisition. Though, the relative uncertainty abundance does not impede the evaluation of the conceivable errors. The data pondered as most influential in defining the outcomes of this work are the measured **Physical properties**, as they serve as input for the realized calculations. The **Materials and Methods** section depicts the procedures and their corresponding execution stages, therefore exposing sources of eventual faults during data acquisition. The second general type of possible errors is the subsequent data handling and processing.

The most varied dataset, the summaries of physical properties of stratigraphic Unit A (**Table 1**, **Table 2** and **Table 3**), has the advantage of showing a range for the data they give, which is for each property a minimum, maximum and mean values, indicating the level of variability to be expected. Here the mean values were used. This first data group is of considerably high influence in the final results of this thesis. The granulometric data (**Figure 26**, **Figure 27** and **Figure 28**), being a rather direct measurement, have as possible error sources the disturbance (specially mixing) of the used samples and (maybe to a lesser extent given the procedure relative robustness) the material handling, both of which with error margins not grasped in this paper. The granulometry, though important, does not play a primary role in the done calculations. The CPT plots (**Figure 30**, **Figure 31**, **Figure 32**, **Figure 42** and **Figure 43**) show quite precise curves, which is by itself reason to suspect of errors. Based on the publication by Ghafghazi and Shuttle (2010) error margins of ± 7% to the CPT extracted values are expected here, which does not hinder the achievement of the general results of this work but do have an effect on the cogitated sizes of possible mass movements, as the thickness and intervals of more/less permeability and porosity sediment layers end up with dimensions oscillating within the assumed ± 7% reach.

Grounded on the calculations done in this work, the first thing to note is that an important threshold is given by the point at which GH become unstable with changing conditions, being a result of the remarkable amount of gas released by GH dissociation, with about 164 m^3 of gas produced by each cubic meter of methane hydrate (of course corrected by the in-situ hydrostatic pressure) here considered as fully developed. This signifies that a vigorous change in pore pressure is caused and its containment is hardly impeded by the rather modest overlying sediment thicknesses considered in this work. Thus, the corresponding variables observed in this thesis (temperature, salinity and pressure) are the main source of error. The pressures, as results of quite straightforward calculations based on the

water density (in turn related to the salinity), are seen as reasonably accurate. For the temperature, in the lack of a precise margin of error, it was attempted to apply increasingly high error margins to the hydrate stability calculations (computing the GH stability for the higher and the lower extreme of a given margin of error for each temperature data point). The result of this exercise was that even with margins of error of 10% (considered generous) for the measured temperatures, the points where GH had been calculated as stable or not remained in such a way; which can be attributed to the considerably sharp GH stability boundary and the distance of the discussed values from it.

Applying the same mode of procedure as for validating the assurance of the temperature values (this time testing the Factor of Safety calculations by using higher and lower extremes of each data point within a range of 10% of the initial, used value) to porosity, density, confined compression modulus of the soil, shear strength and slope angles utilized in the determinations (considered highly influential variables), it turned out that the reported results remained unchanged. In other words, where slope failure was estimated to occur (in effect at the points where GH got destabilized) after a 1, 8 and 11 °C temperature increments, the outcome rested in the same condition after re-trying the same calculations with a ± 10% change to the mentioned parameters. The conclusion of this error analysis is that even though the used parameters are passive of imprecision, the goal of this work is satisfied even if the error margins are at one tenth for the used figures.

4.8. Implications and outlook

The study of slope stability at the Beaufort Shelf and Slope is of academic as well as of very practical scope, with ramifications that are likely to progressively gain importance as the Arctic Ocean region is considered of interest by governmental and private actors. The current expansion of initiatives brought upon by nations that surround the Arctic Ocean (Canada, Denmark (Greenland), Finland, Iceland, Norway, Russia, Sweden, and the United States) shines a light on how the better understanding of the largely uncovered geological dynamics at play in the region are geopolitically consequential.

Global trends of economic development and the corresponding search for new mineral and fuel resources (the US Geological Survey believes that the region may house approximately 25% of the world's oil reserves) put the Arctic region within the aim of economic exploitation, which in the past received less attention due to the more remote necessity of its resources and, perhaps principally, due to challenges represented by the highly hostile Arctic conditions. Another frequently neglected type of resource that might create impasse is the local sea-life, being of consequence for fisheries. With vast,

very promising, but mostly undetermined resources, the region is to require large efforts in studying its potential, hence representing a major target for research investment. Parallel to the interest in its resources, modern effects of climatic change have set off severe modifications in the sea-ice regime in the Arctic, resulting in the opening of new navigation routes that are of great economic interest (and dispute) as shorter trade routes, as well as carrying consequences for strategic defensive and offensive military capabilities since formerly naturally impervious areas become of easier access.

In order to fulfill the referred prospective goals, two general aspects can be highlighted as primary steps to be taken, namely the settlement of personnel and the construction of infrastructure. The regional geohazard analysis is of great relevance when it comes to the feasibility and risks taken into account when planning such enterprises, particularly at sea, where arguably most of the resource-related objectives could be drawn to (besides of course being the focus of this thesis). As trends in environmental change and human presence in the Arctic continue, a crucial element for a successful occupation of the region is the medium- to long-term forecast of the local conditions, for instance in relation to the temperature changes (considered to be rapidly evolving and somewhat explored in this work), but also regarding possible reorganization of oceanic currents, further effects in sea-ice, salinity, etc. Such goals represent both a great challenge and a valuable opportunity.

5. Conclusions

Considering the aspirations of this work, the scrutinized data and the derived deliberations lead to conclude about the GH- and PF-related slope stability forecasts for the focused Beaufort Sea region that:

- The region is vulnerable to slope destabilization resulting from temperature changes, particular from GH dissociation and at the Beaufort Slope;
- Regarding the top meters of sediment (roughly <10 m), PF thawing and GH dissociation occur separately, since PF is found at the shelf and GH are found on the slope below 200 m of water depth;
- PF thawing in the top meters of sediment (at least < 10 m) would interest just the Beaufort Shelf (shallower than ≈ 120 m water depth) - the area where PF is found. Hence, possible slope destabilization from such thawing would take place around the Shelf Break, where the loss of material strength would encounter slope gradients prone to failure.
- A temperature increment of 1°C in the GH-bearing sediment of the Beaufort Slope was computed as sufficient to prompt slope failure; other parts of the study area where punctual data were available, i.e.: the Western and the Northern Canyon, were calculated as prone to similar effects with sediment temperature increments of 8 and 11°C respectively.
- Forecasts of global climatic change predict that, especially at the Arctic region, environmental modifications of sufficient magnitude to trigger the kind of slope failure here described are realistic to occur;
- Contemplating that sediment warming would be transferred from the bottom waters to the sediment and then progressively migrate downward, in the positions where this warming leads to GH dissociation on the Slope, the eventual ensuing mass wasting episodes would also occur progressively –as the superficial GH-bearing layer has its GH destabilized. The resulting release of gas and loss of strength would cause this top layer to fail, until the warming reached the next such layer and the process could be repeated.

Acknowledgements

The completion of this work is certainly an event that would not have come to pass without the support of a unique group of people, who helped me with their wisdom, knowledge, guidance, experience, and work. Most directly, my supervisor Prof. Dr. Achim Kopf was of key importance, from the initial conversation about the theme choice, to the definition of the main guidelines and of course the either personal or virtual dependable availability for clarifications and evaluations. The PhD student Walter Menapace was another top agent in the development of this work, in practice being the person that I bothered the most with my occasional problems and conundrums, but invariably being open to discuss the issue at hand facilitate the reach of a solution. Robert Roskoden, a fellow Marine Geosciences M.Sc. student, was also very helpful with the processing of the CPT data, sharing literature and offering insights on the broad development of the research theme. Plus, I would like to express my appreciation to the other members of the Marine Geotechnics workgroup at the MARUM, namely Timo Fleischmann for the provision of data and technical support with the CPT, Matthias Lange and Dr. Matt Ikari for the assistance and very important elucidations concerning geotechnics and the operation and results of the Ring Shear test and Dr. Gauvain Wiemer for the enlightenment about geotechnical theory and the useful observations

An essential and very honorable contribution I received in this work is also one that came from very far away, from the Korean Institute for Polar Research, in which Dr. Young Keun Jin and Nari Seo were enormously diligent in providing me with a very good quality and well processed set of sub-bottom profiles, without which my understanding of the geological context of the Beaufort Sea shelf and slope would be severely debilitated.

To all my professors during my M.Sc. studies at the University of Bremen (and also during my B.Sc. at the University of Bologna), who equipped me with the necessary knowledge to pursue my aspirations as a geologist, I wish to communicate my immense appreciation for their work.

I would also like to thank all those persons who are not mentioned here, who in many different ways supported me with their criticism, suggestions, friendliness and friendship.

To my family, thanks for all the most important things.

List of figures

List of tables

Appendix

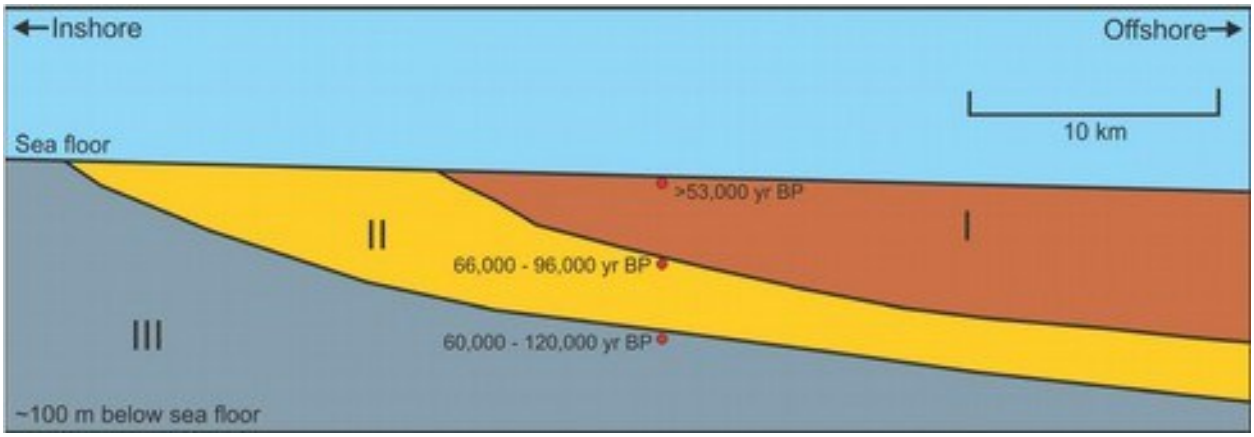

Figure 45: North-south schematic cross section of the Western Beaufort Shelf displaying the stratigraphic units of the upper 100m of sediment. Further description of units I, II and III are found in text (Blasco et al., 2013).

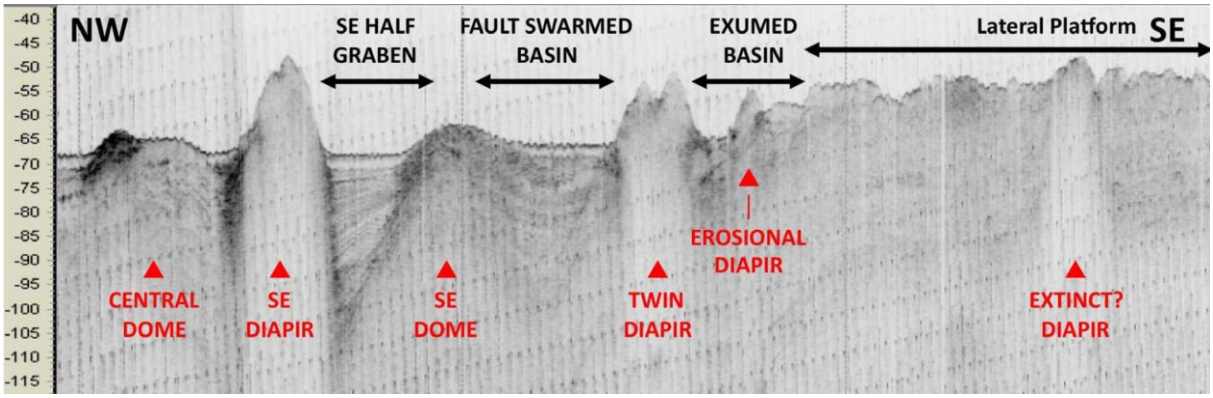

Figure 46: Illustrational example of seismic profile showing several diapiric structures in the southeast lateral platform of the Garry Knolls area (Blasco et al., 2013).

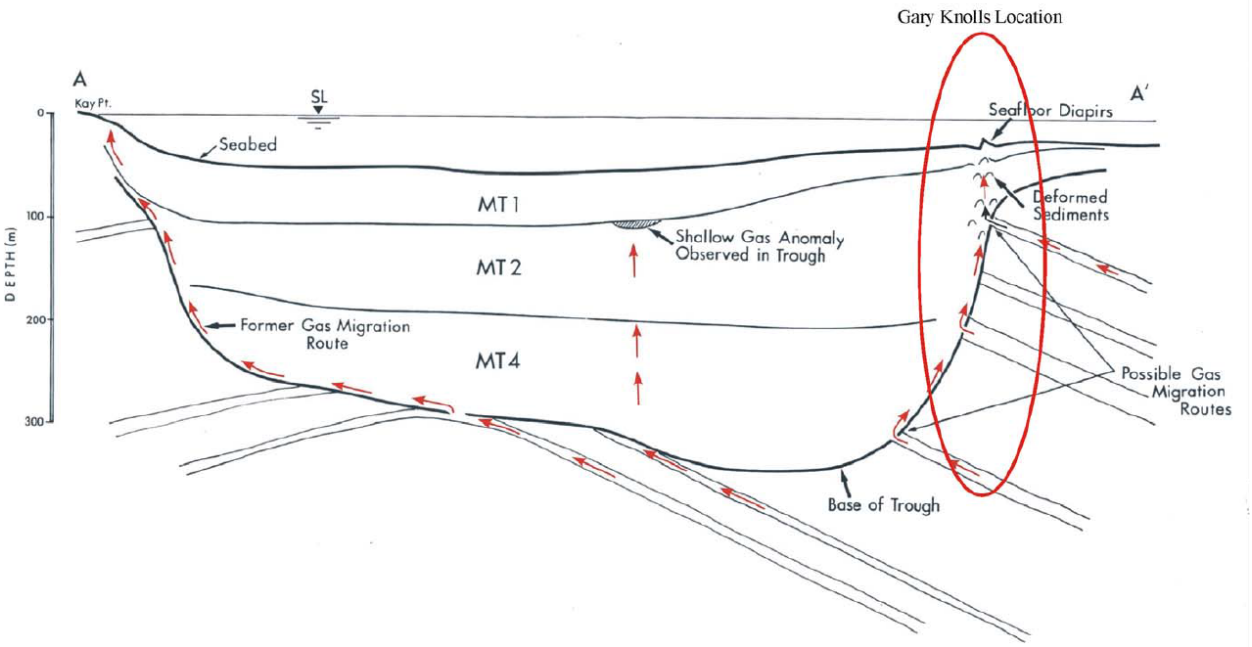

Figure 47: Schematic of theorized gas migration mechanism in the Mackenzie Trough (O'Connor, 1985).

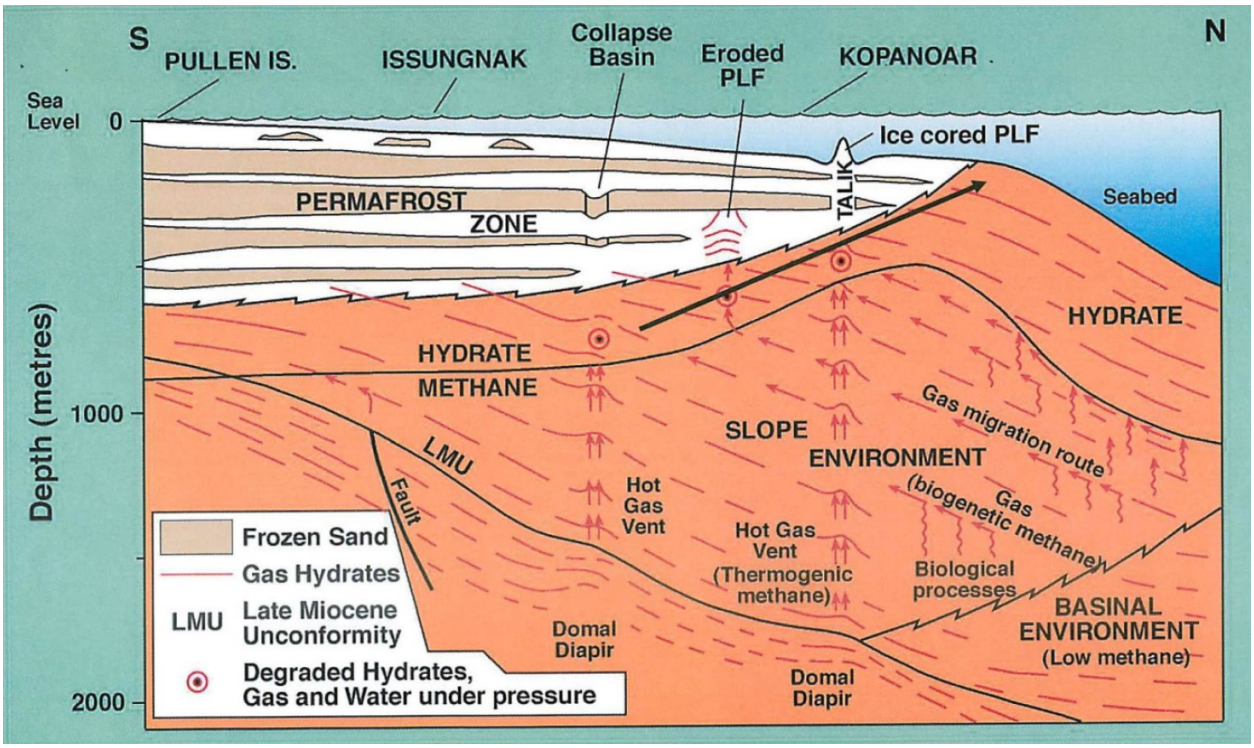

Figure 48: General scheme by Fortin & Blasco (1990) describing several elements related to permafrost, gas hydrates, gas migration and such.

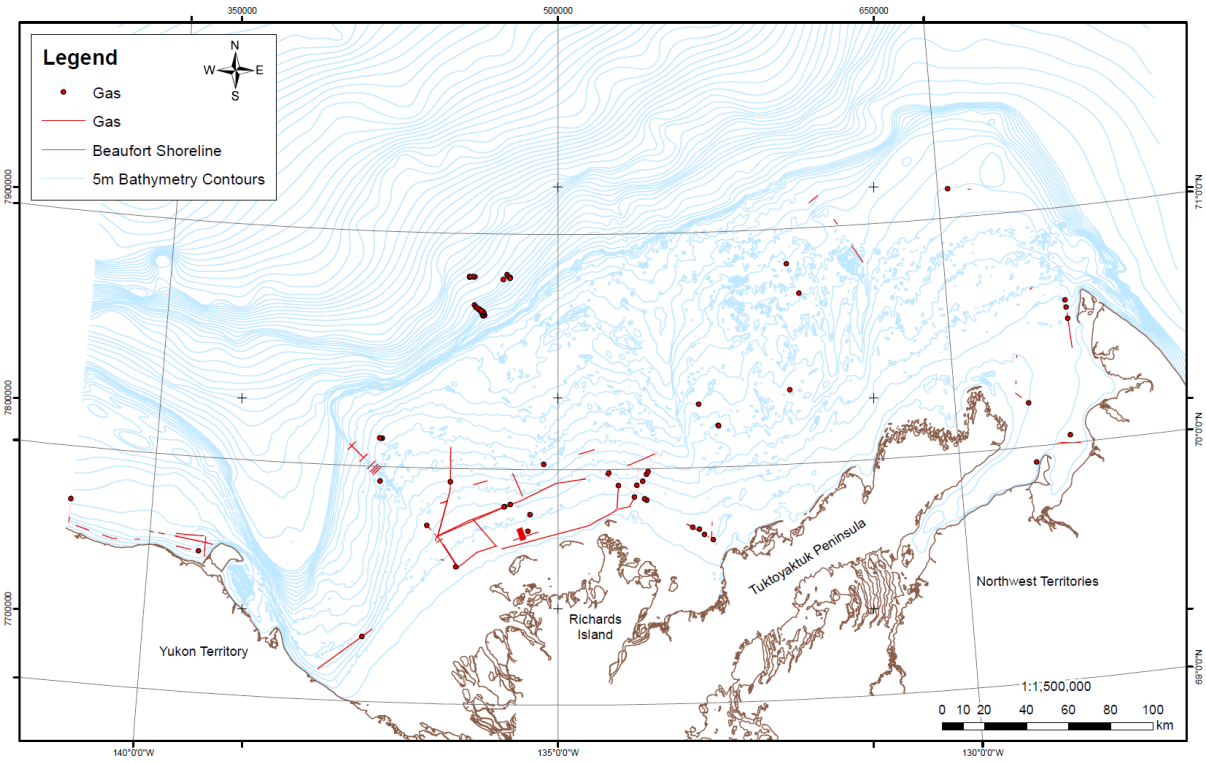

Figure 49: Location of areas where shallow gas has been identified by the Canadian Seabed Research (CSR) between 2004 and 2009 (Blasco et al., 2013).

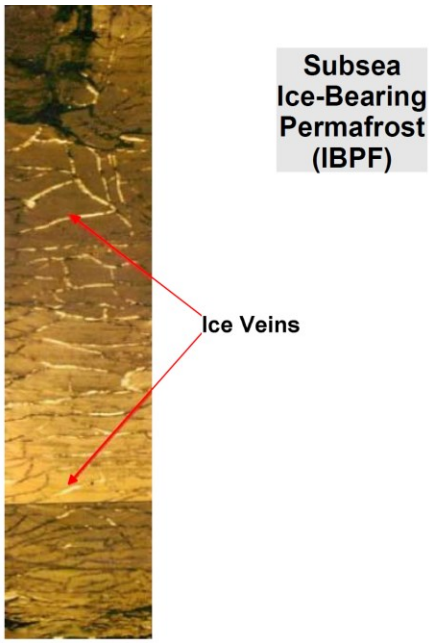

Figure 50: Detail of a geotechnical borehole sample of permafrost with ice veins (Blasco et al., 2013).

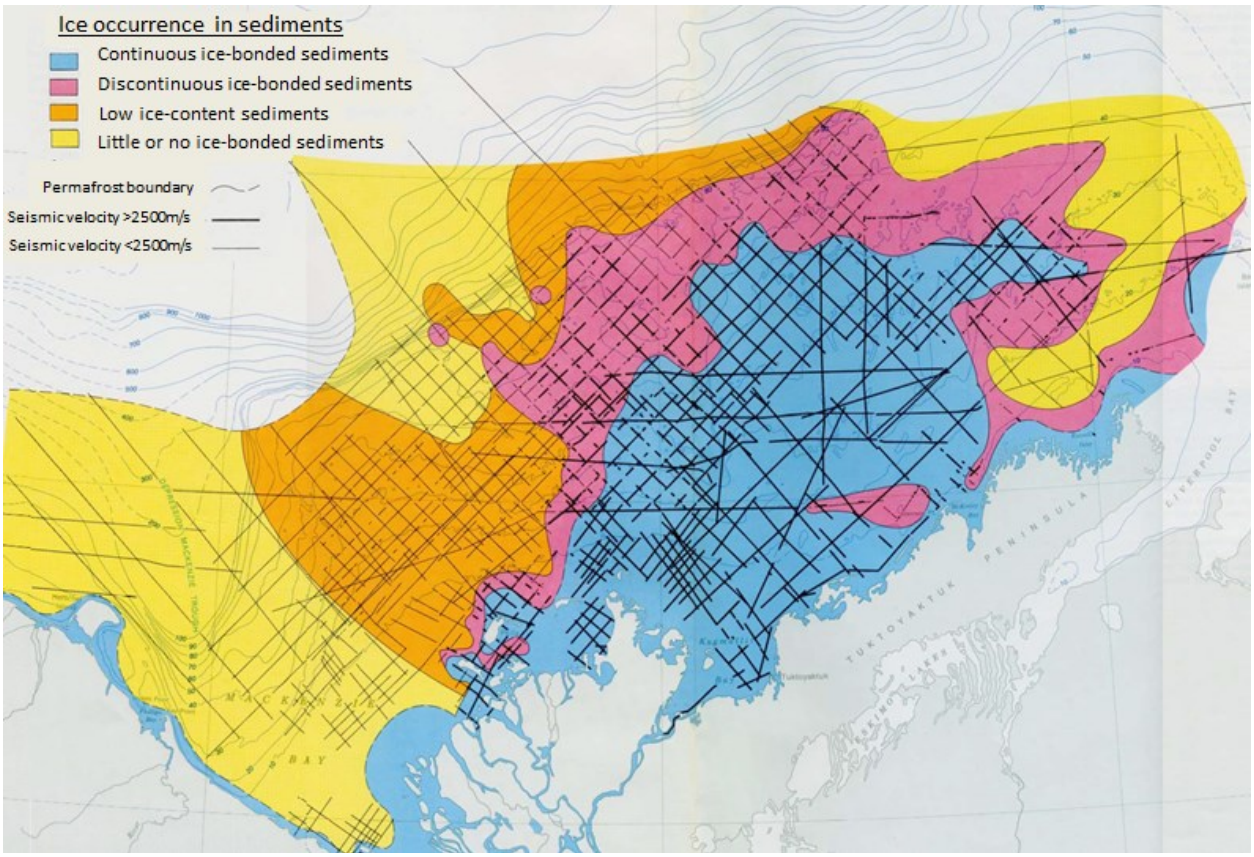

Figure 51: Map of areas where permafrost has been identified with seismic refraction analysis (modified after Pullan et al., in Pelletier, 1987). Legend: Blue: continuous ice-bonded sediments; Pink: discontinuous ice-bonded sediments; Orange: low ice-content sediments; Yellow: little or no ice –bonded sediments; Outer dashed lines: subsea permafrost boundary; Thicker straight lines: seismic velocities >2500m/s; Thinner straight lines: seismic velocity <2500m/s.

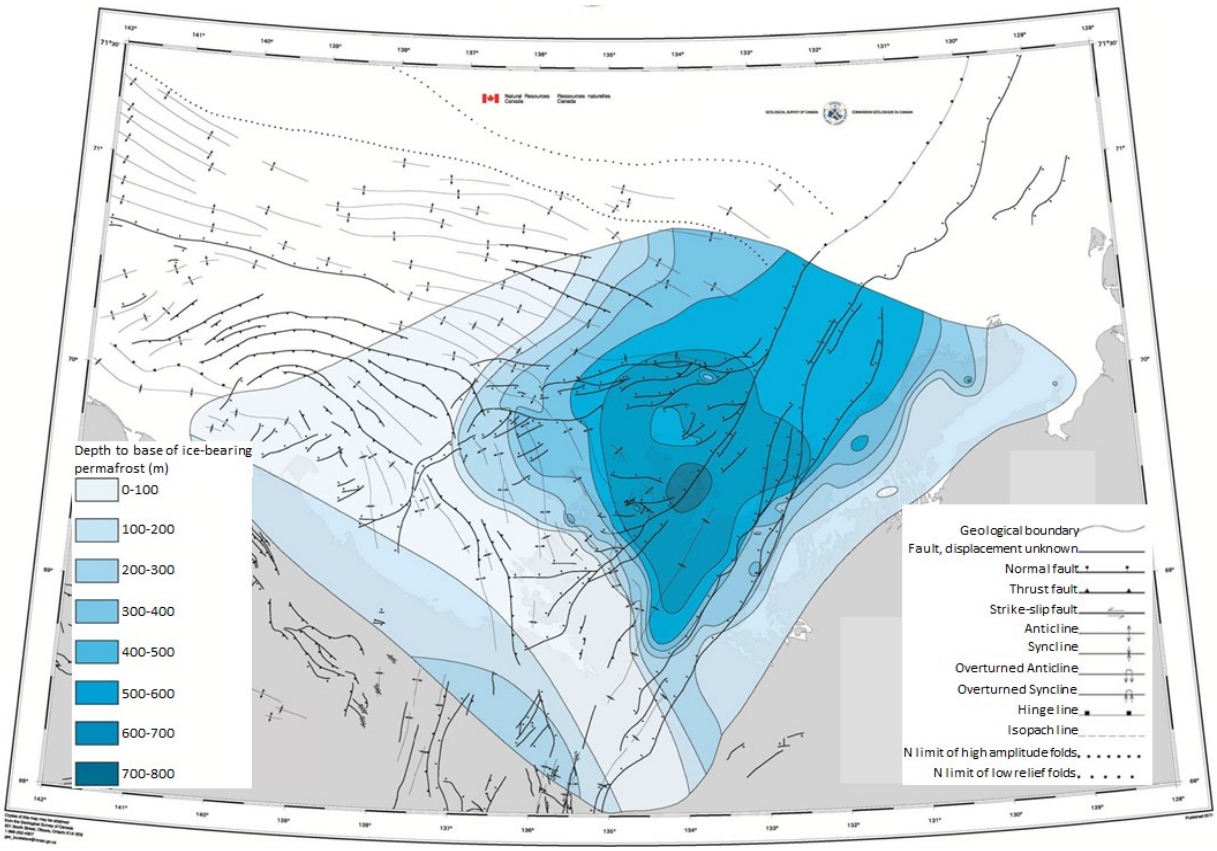

Figure 52: Distribution of depths to the base of ice-bearing permafrost (modified after Issler et al, 2013).

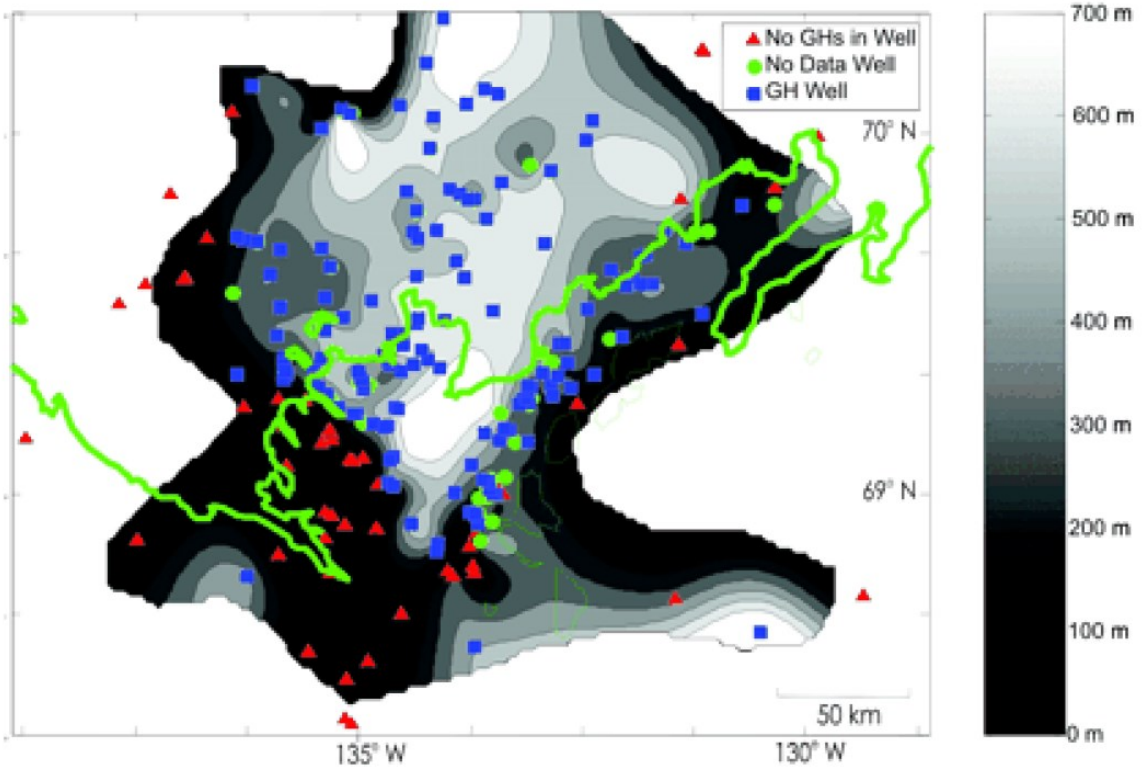

Figure 53: Thickness of the subseafloor depth intervals with geothermal conditions that would allow for gas hydrate stability (Osadetz and Chen, 2007). Point features indicate drill well positions (Osadetz and Chen, 2007).

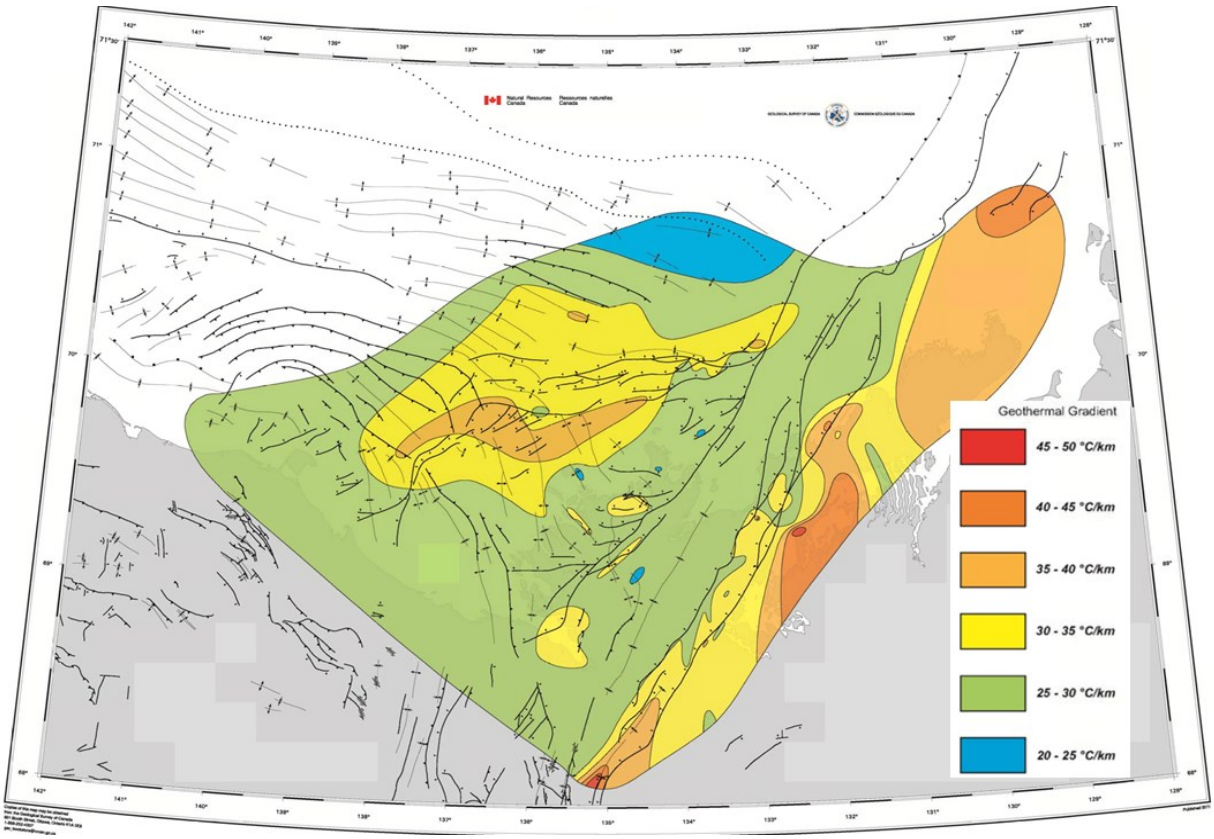

Figure 54: Regional geothermal gradient of the Beaufort MacKenzie Basin (modified after Issler et al., 2011).

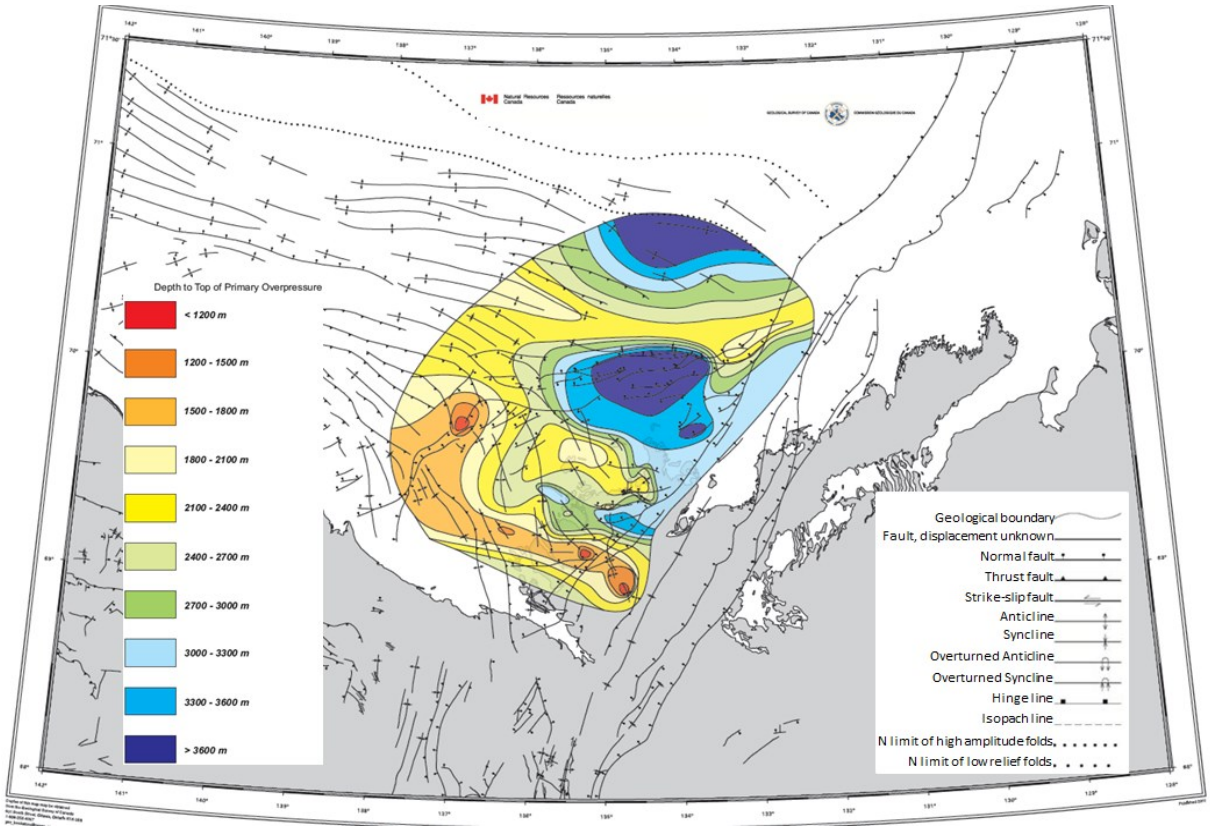

Figure 55: Contour map with the depth to the top of overpressure zones (modified after Blasco et al., 2013).

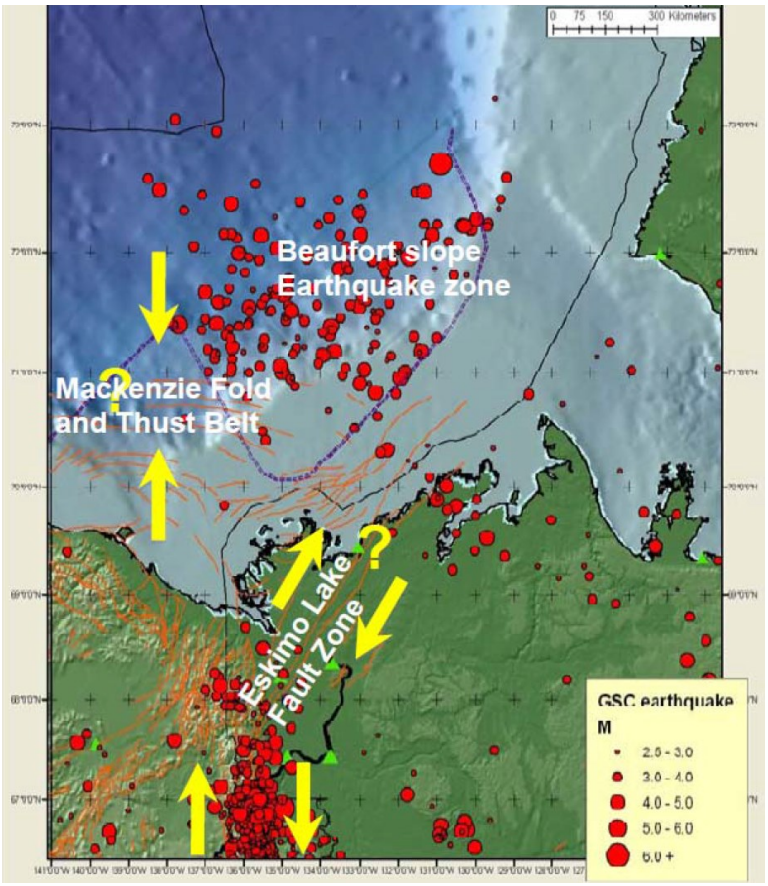

Figure 56: Locations of historical earthquakes, their estimates intensities and suggested earthquake zones (Blasco et al, 2013).

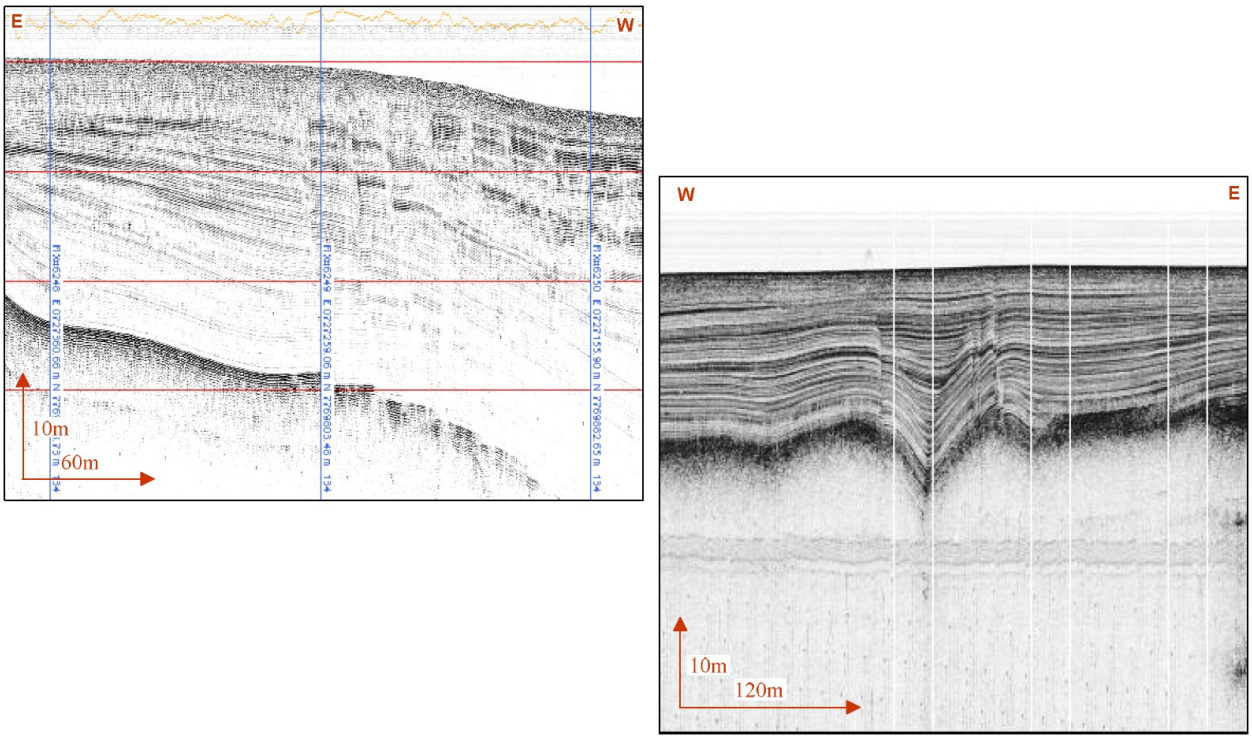

Figure 57: Profiles showing small scale faulting in laminated sediments (Campbell at al., 2008).

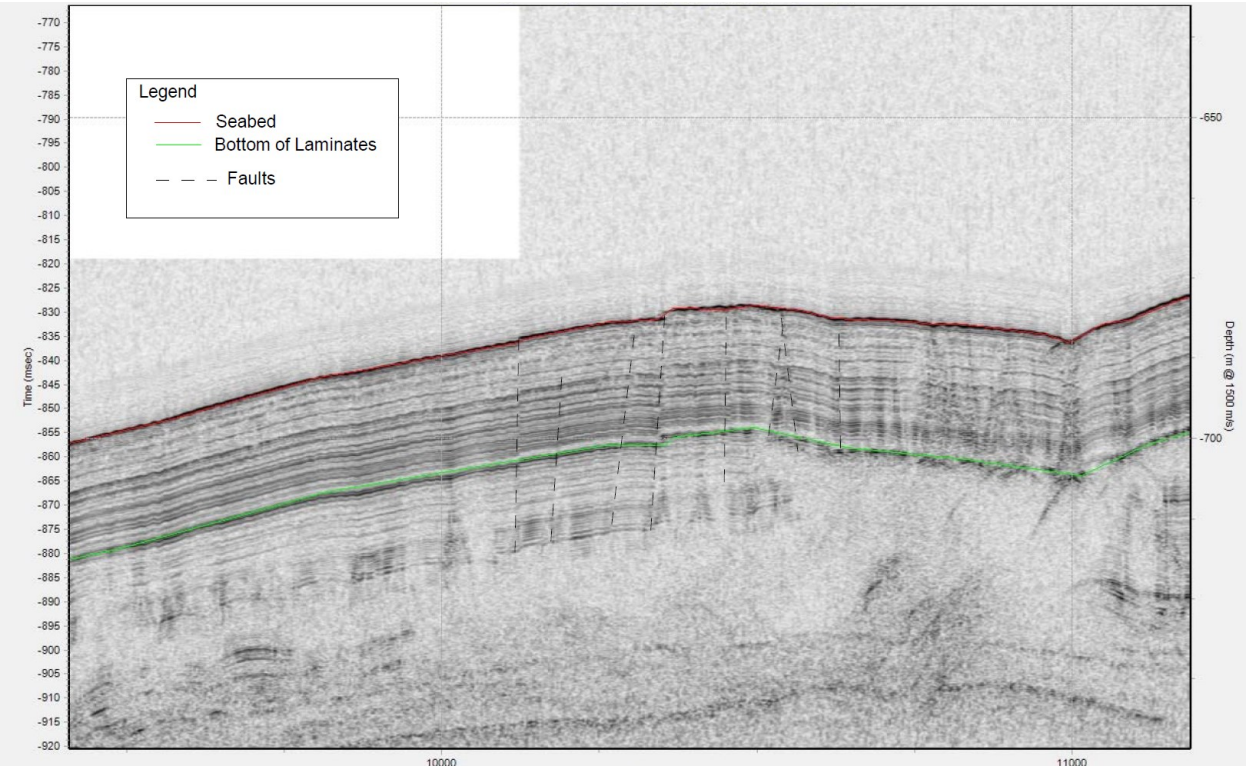

Figure 58: Profile showing compressional faults at the base of the Beaufort Slope (Campbell et al, 2009).

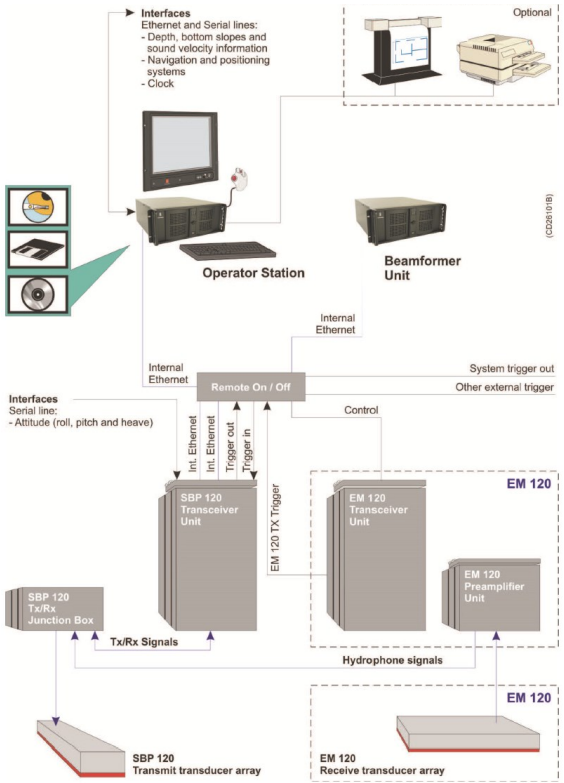

Figure 59: Diagram with system components and interfaces of SBP 120 installed on the ARAON research vessel (Jin & Riedel, 2014).

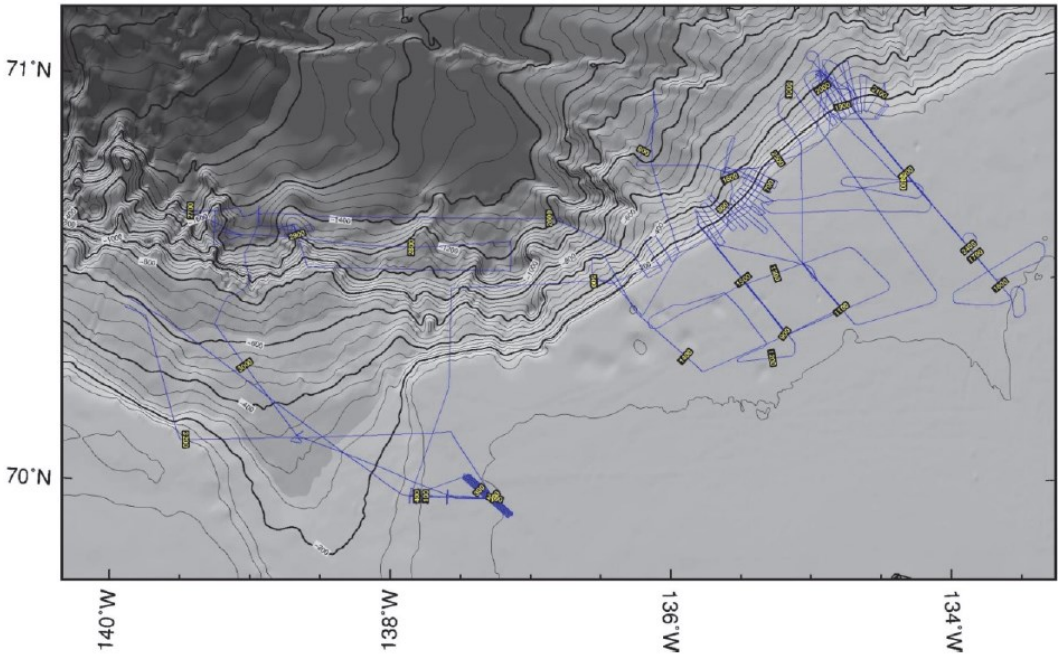

Figure 60: Map of the region investigated during expedition ARA04C, with ship navigation tracks (blue line) (Jin & Riedel, 2014).

Table 4: Settings of SBP 120 system during the ARA04C expedition.

Used Settings	Value	Unit
Runtime Parameter		
Transmit mode	Normal	
Synchronization	Fixed ping rate	ms
Acquisition delay	manual & automatic mode	ms
Acquisition window	400	ms
Pulse form	Linear chirp up	
Sweep low frequency	2500	Hz
Sweep high frequency	6500	Hz
Pulse shape	80	%
Pulse length	30	ms
Source power	0	dB
Beam widths Tx	Normal	
Beam widths Rx	Normal	
Number of Rx beams	1	
Beam spacing	3	1deg
Calculate delay from depth	X	
Delay hysteresis	30	%
Bottom screen position	50	%
Automatic slope corrections	On	

Gain	36	dB
Bottom tracker		
Window start	40	ms
Window length	20	ms
Threshold	80	%
Time Variable Gain		
TVG control	manual	

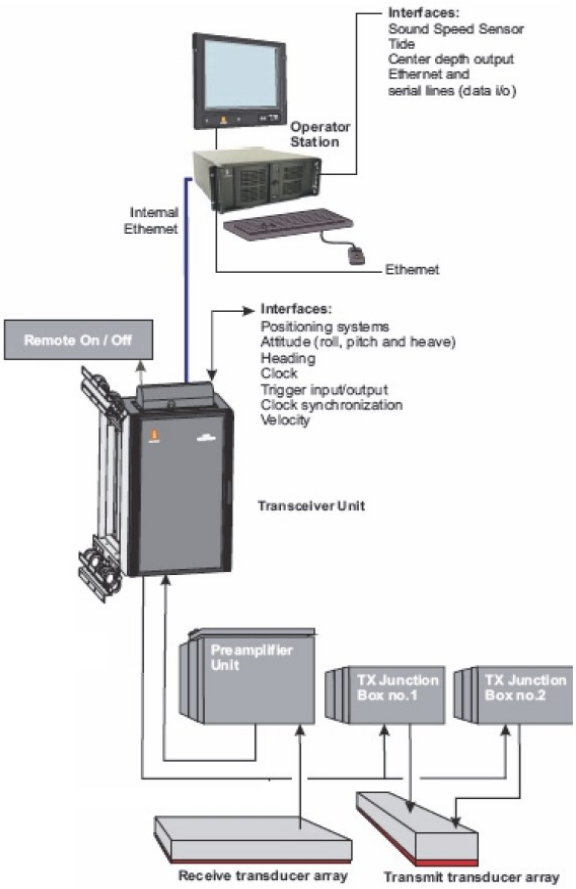

Figure 61: Schematic with components and interfaces of the EM122 Multibeam system (Jin & Riedel, 2014).

Table 5: Configuration of the EM122 using during the ARA04C expedition.

Operating frequency		12kHz
Depth range		20-11000m
Swath width		6X depth. To approx. 30km
Pulse forms		CW and FM chirp
No. of beams		432
Swath profiles per ping		1 or 2
Motion compensation	Yaw	±10 degrees
	Pitch	±10 degrees
	Roll	±15 degrees
Sounding pattern		Equi-distant on bottom/equiangular
Depth resolution of soundings		1cm
High resolution mode		High density processing
Sidelobe suppression		-25dB
Modular design, beam width		0.5 to 4 degrees

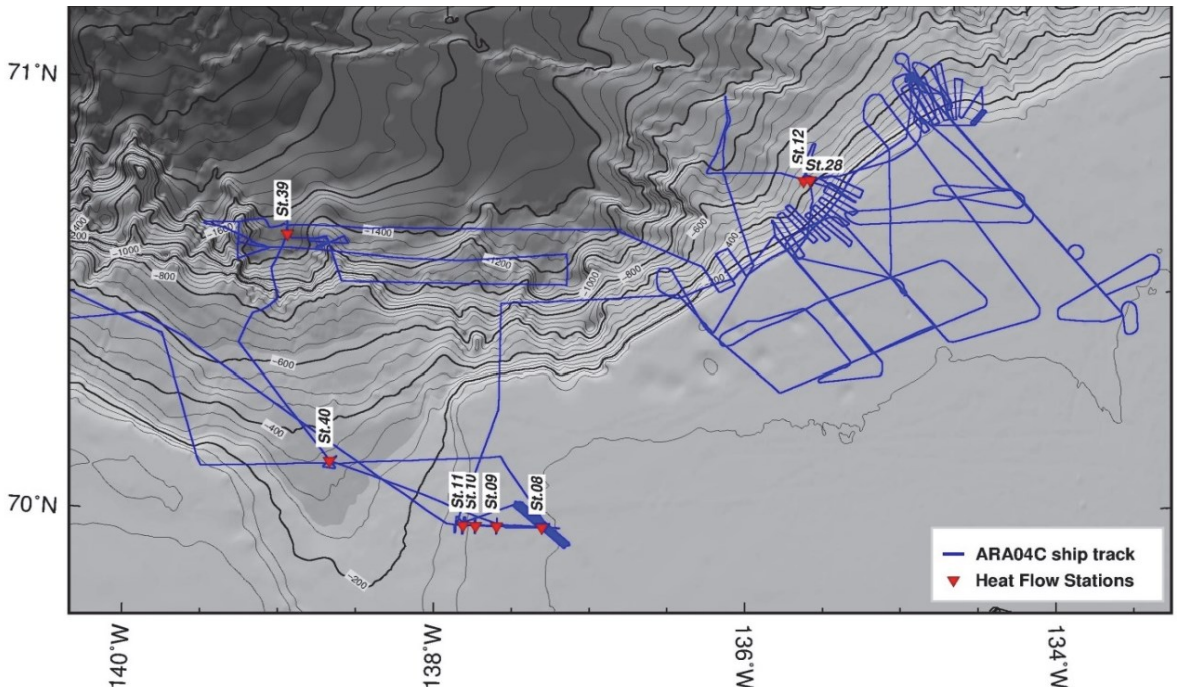

Figure 62: Map with red triangles representing the locations where heat flow measurements took place during cruise ARA04C (Jin & Riedel, 2014).

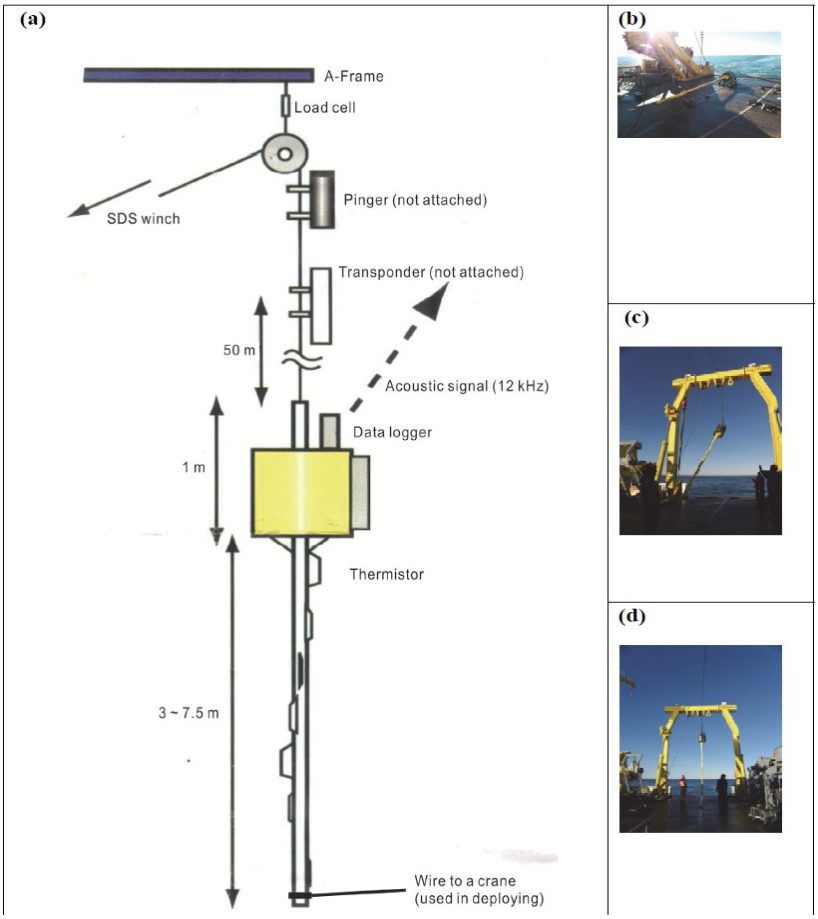

Figure 63: Ewing type heat probing system used in cruise ARA04C. (a) Diagram of equipment components and interfaces; (b) probe positioned on deck of IBRV ARAON; (c) and (d) snapshots of deployment procedure (Jin & Riedel, 2014).

Table 6: Specifications of the Ewing type heat probe used during ARA04C expedition.

Part	Specification	
Data logger	Dimension	50 kg
		Ø144*775 mm
	Housing	Up to 6000 m
	Measuring channel	#1~#10
		#10 for fixed resistor as reference
	Measuring interval	30 sec
	Measurable resistance	1500-6500Ω
	Depth sensor	Up to 6000 m with accuracy of 1 m
	Tilt sensor	Up to ±45 degree on X, Y axes with accuracy of 0.1 degree
	Memory	32MB (corresponding to 0.5 million records)
	Heat pulse	On/Off
		When mode 'On', for 12 seconds with 5 V in 6/8/10 minutes after shock
	Pinger frequency	12/13/14/15 kHz

	Pinger pulse length	2/5 ms
	Pinger oscillation mode	3
		(Heater On/Heater Off/Tilted)
	Connectivity	RS-232C
	Battery	NiCd 7.2V *1 for measurement
		NiCd 25.2V *1 for the pinger
Thermistor	Length	Up to 6.5 m
	Type	2
		(Heat-generating/Normal thermistor)
	Measurable temperature	~1500 Ω for 80 degree
		6000 Ω for 0 degree
		Accuracy: 0.01 degree
Frame	Head	400 kg
		Ø540*1330 mm
	Barrel	~35 kg/1.5 m
		Adjustable using 2 units (1.5 m/3.0 m)

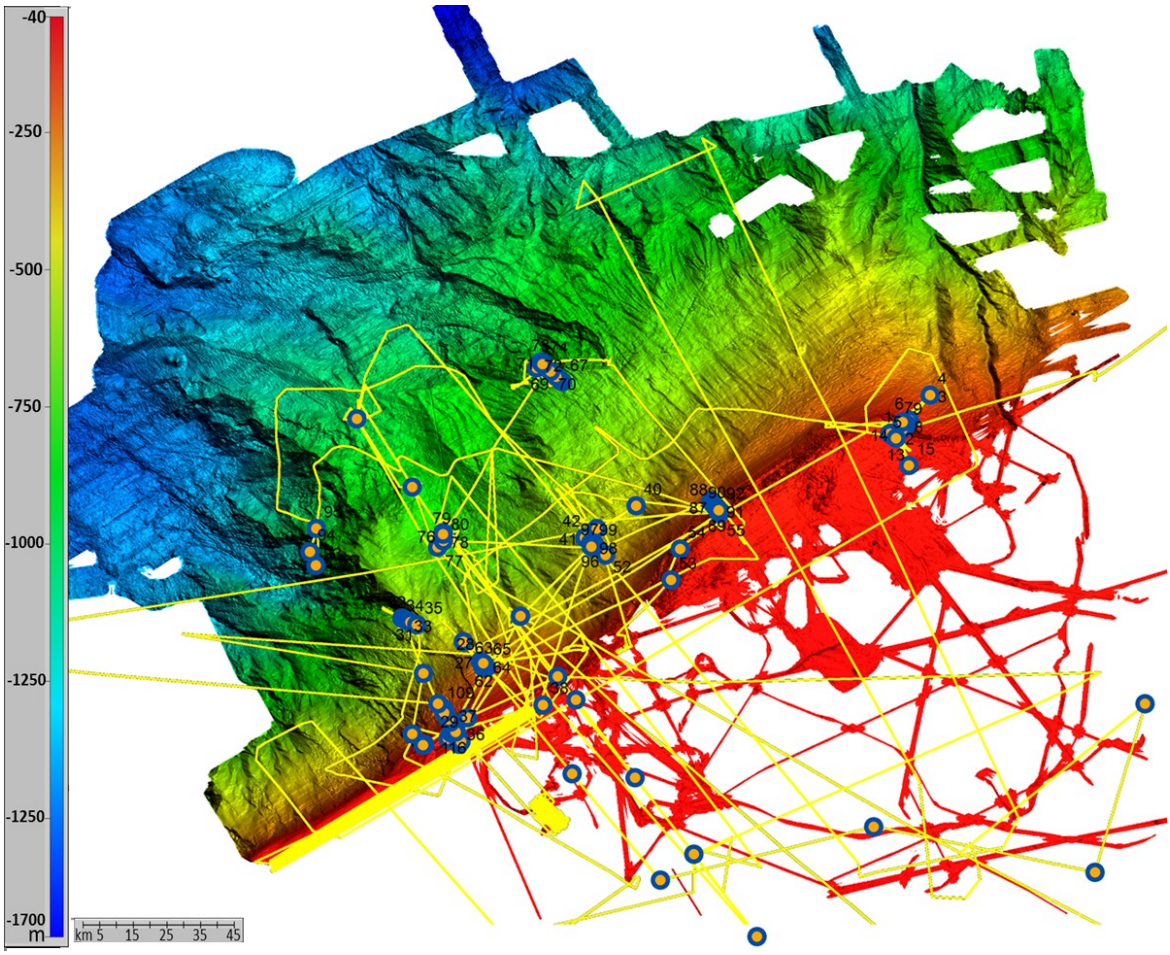

Figure 64: Map including ship tracks (yellow line) and all sampling locations (orange-blue dots).

Table 7: Specifications of the multi-sensor core logging equipment GEOTEK MSCL-25 used in cruise ARA04C.

P-wave velocity and core diameter	Displacement transducer orientation: horizontal
	Plate-transducer diameter: 40 mm
	Transmitter pulse frequency: 500 kHz
	Pulse repetition rate : 1 kHz
	Received pulse resolution: 50 ns
	Gate: 5000
	Delay: 0 s
Density	Radiation beam orientation: horizontal
	Gamma ray source: Cs-137 (1983)
	Activity: 356 Mbq (1983)
	Energy: 0.662 MeV
	Collimator diameter: 5.0 mm
	Gamma detector: Gammasearch2, Model SD302D, Ser. Nr. 3043 , John Count Scientific Ltd., 15 s counting time.
Temperature	Infrared Sensor: MICRON M50-1C-06-L
	Range: -20° - 300° C
	Output Voltage: 10 mV
Electrical Resistivity	Sensor Type: Geotek
	Principle: Magnetic Induction
	Detection Range: 0.1-10 Ωm
	Resolution: approx. 20 mm
	Loop sensor: BARTINGTON MS-2C
	Loop sensor diameter: 14 cm
Magnetic susceptibility	Alternating field frequency: 565 Hz, counting time 10 s, Precision 0.1 * 10-5 (SI).
	Magnetic field intensity: ca. 80 A/m RMS

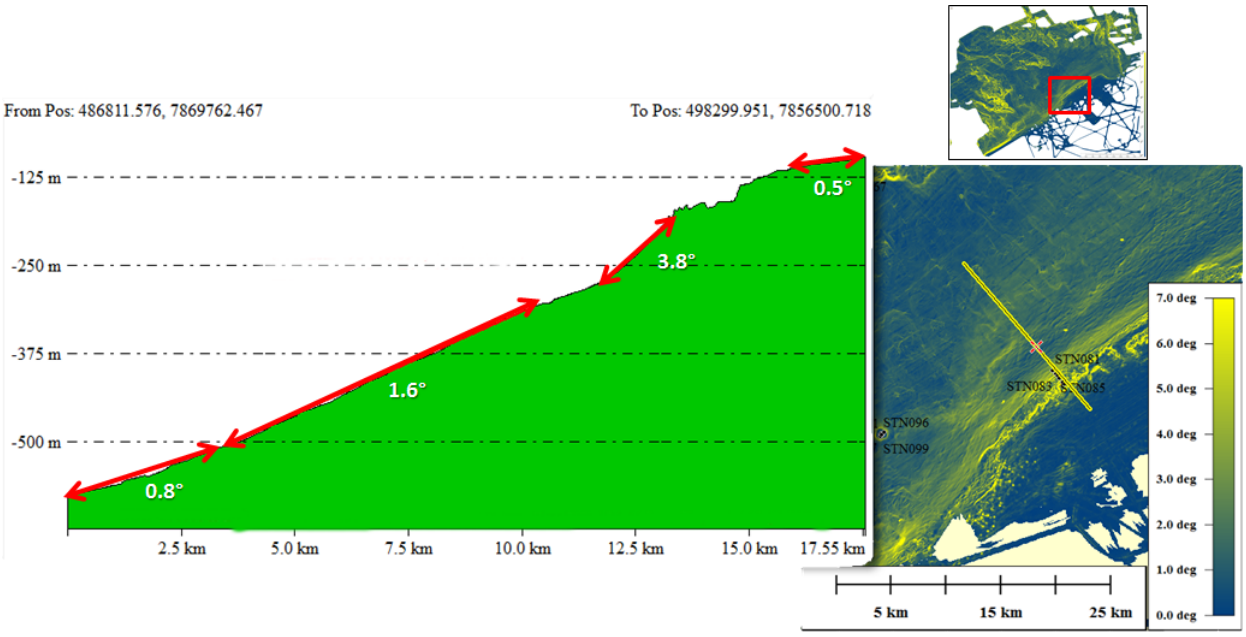

Figure 65: Approximate slope angles of represented transect across the Beaufort Central Shelf and by map colors (in yellow are steeper and in blue are flatter areas; angles according to scale). Detail map shows its relative position on overview.

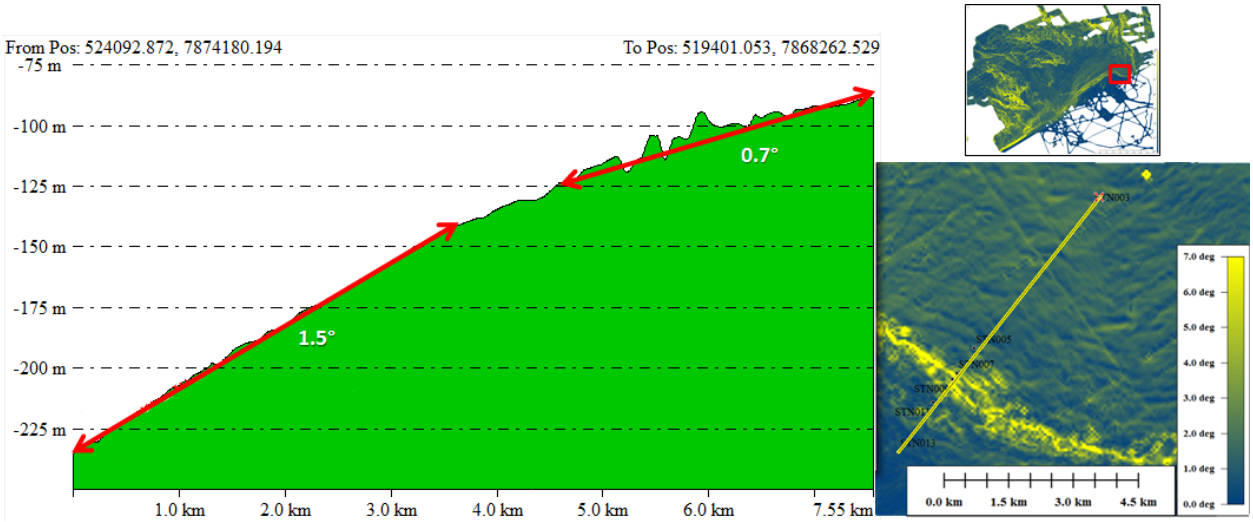

Figure 66:Approximate slope angles of represented transect across the Beaufort East Shelfand by map colors (in yellow are steeper and in blue are flatter areas; angles according to scale). Detail map shows its relative position on overview.

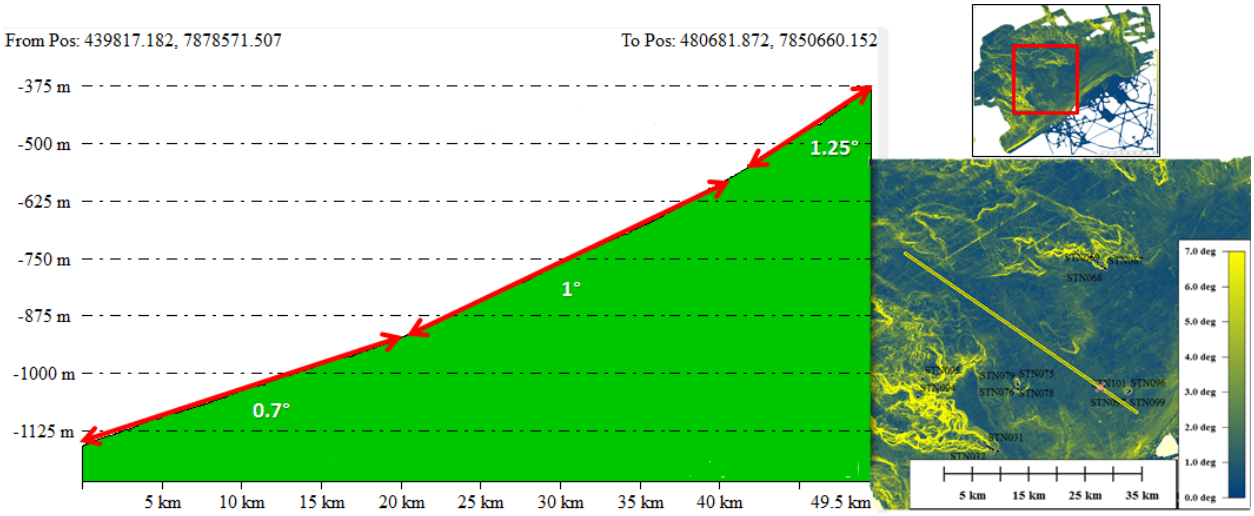

Figure 67: Approximate slope angles of represented transect across the deeper Beaufort Slopeand by map colors (in yellow are steeper and in blue are flatter areas; angles according to scale). Detail map shows its relative position on overview.

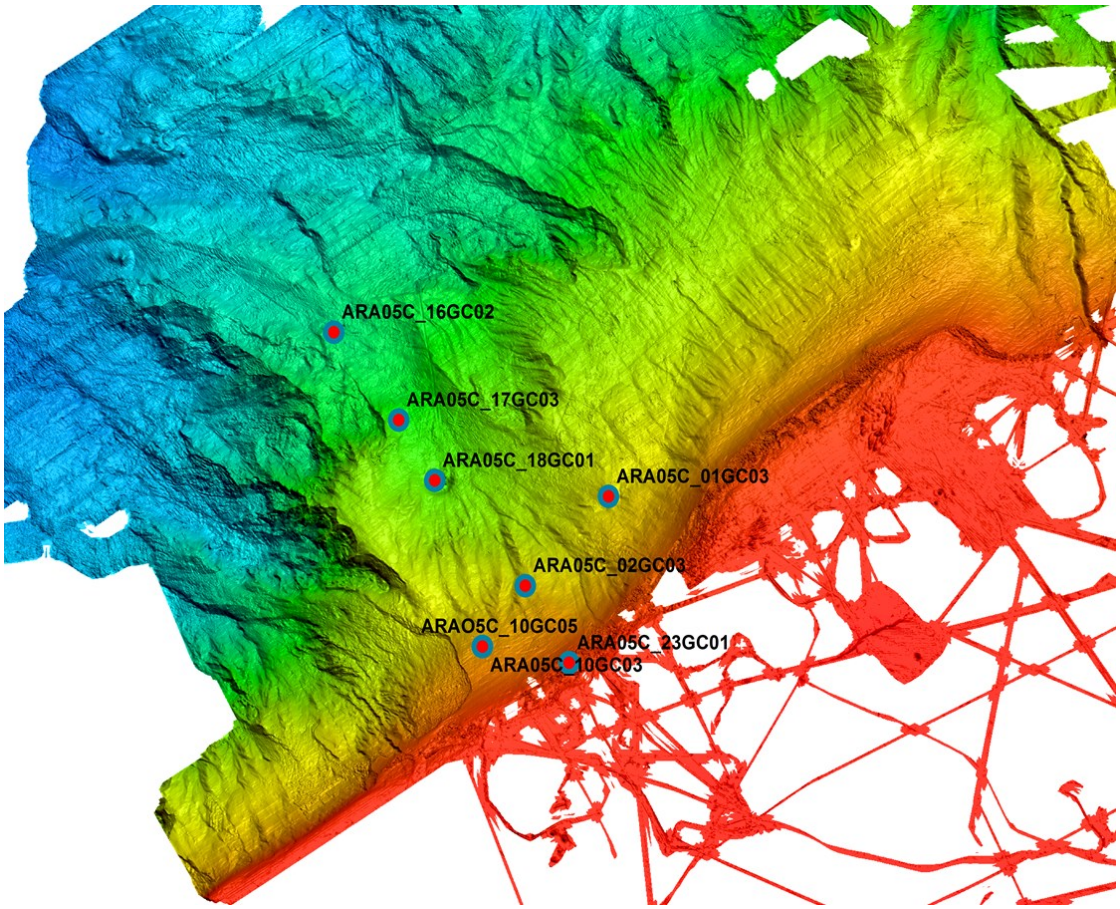

Figure 68: Gravity core positions of cruise ARA05C.

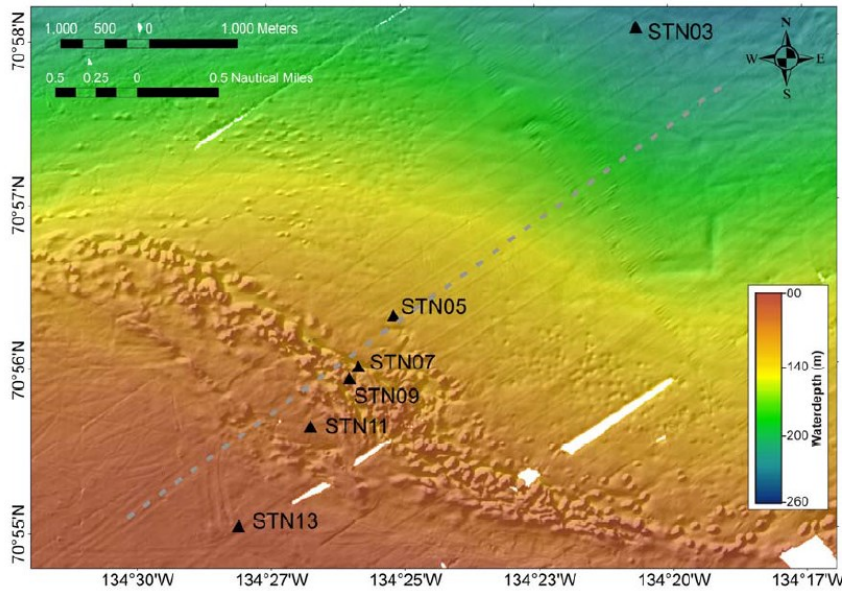

Figure 69: Eastern Shelf transect from cruise CCGS Sir Wilfrid Laurier 2013, with temperature measurement stations. Station numbers and respective water depths: 03 (235m), 05 (128m), 07 (125m), 09 (110m), 11 (105m) and 13 (90m) (Riedel et al., 2014).

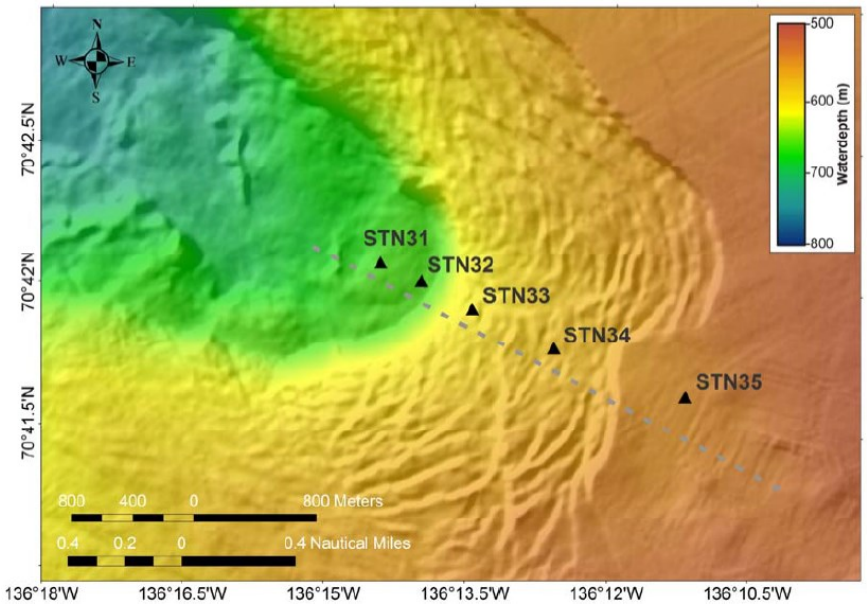

Figure 70: Western Canyontransect from cruise CCGS Sir Wilfrid Laurier 2013, with temperature measurement stations. Station numbers and respective water depths:31 (688m), 32 (685m), 33 (620m), 34 (607m) and 35 (568m) (Riedel et al., 2014).

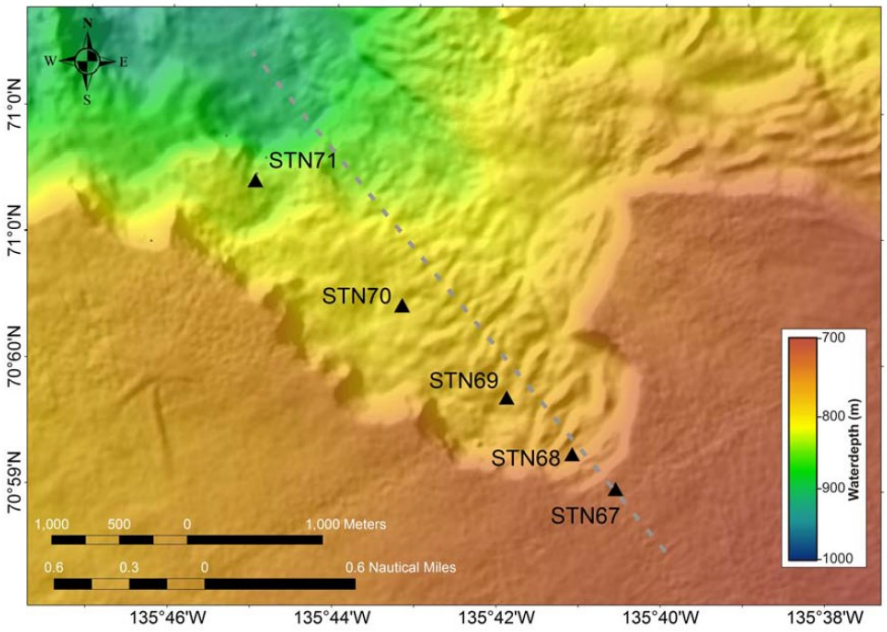

Figure 71: Northern Canyon transect from cruise CCGS Sir Wilfrid Laurier 2013, with temperature measurement stations. Station numbers and respective water depths:67 (748m), 68 (770m), 69 (770m), 70 (828m) and 71 (865m) (Riedel et al., 2014).

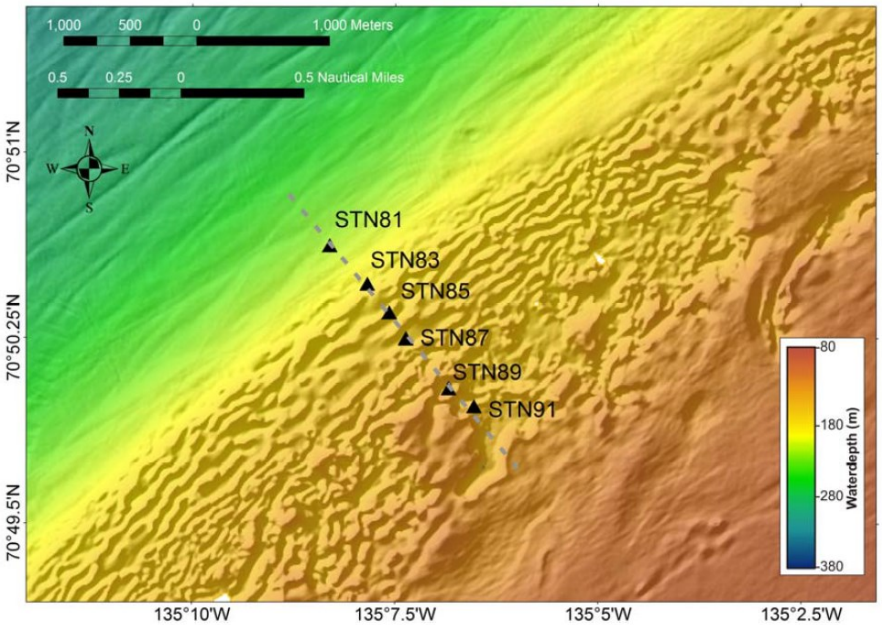

Figure 72: Central Shelf transect from cruise CCGS Sir Wilfrid Laurier 2013, with temperature measurement stations. Station numbers and respective water depths: 81 (230m), 83 (210m), 85 (180m), 87 (185m), 89 (175m) and 91 (170m)(Riedel et al., 2014).

Table 8: Sediment temperatures of the study area.

Area	Lat	Long	**Water Depth** (m)	Depth (mbsf) of sed. Temp.	**Sediment Temperature** (°C)
E Shelf STN_03	70.968	-134.343	235	0.001	-0.187
	70.968	-134.343	235	0.7	0.042
	70.968	-134.343	235	1.2	-0.175
	70.968	-134.343	235	2.3	-0.187
E Shelf STN_05	70.939	-134.420	128	0.7	-1.32
	70.939	-134.420	128	1.2	-1.3
	70.939	-134.420	128	2.3	-1.29
E Shelf STN_07	70.933	-134.431	125	0.001	-1.731
	70.933	-134.431	125	0.7	-1.359
	70.933	-134.431	125	1.2	-1.332
	70.933	-134.431	125	2.3	-1.325
E Shelf STN_09	70.932	-134.434	110	0.001	-1.854
	70.932	-134.434	110	0.7	-1.406
	70.932	-134.434	110	1.2	-1.38
	70.932	-134.434	110	2.3	-1.404
E Shelf STN_11	70.927	-134.446	105	0.7	-1.4
	70.927	-134.446	105	1.2	-1.401
	70.927	-134.446	105	2.3	-1.413
E Shelf STN_13	70.917	-134.468	90	0.001	-2.014
	70.917	-134.468	90	0.7	-1.399
	70.917	-134.468	90	1.2	-1.382
	70.917	-134.468	90	2.3	-1.387
W Canyon STN_31	70.702	-136.241	688	0.8	0.252
	70.702	-136.241	688	1.3	0.254
	70.702	-136.241	688	2.3	0.363
W Canyon STN_32	70.701	-136.234	685	0.8	0.255
	70.701	-136.234	685	1.3	0.252
	70.701	-136.234	685	2.3	0.371
W Canyon STN_33	70.699	-136.224	620	0.8	0.277
	70.699	-136.224	620	1.3	0.244
	70.699	-136.224	620	2.3	0.322
W Canyon STN_34	70.697	-136.210	607	0.8	0.336
	70.697	-136.210	607	1.3	0.367
	70.697	-136.210	607	1.8	0.371
	70.697	-136.210	607	2.3	0.399
W Canyon STN_35	70.694	-136.187	568	0.8	0.355
	70.694	-136.187	568	1.3	0.384
	70.694	-136.187	568	1.8	0.386
	70.694	-136.187	568	2.3	0.409
N Canyon STN_67	70.983	-135.676	748	0.6	0.088
	70.983	-135.676	748	1.1	0.091
	70.983	-135.676	748	1.6	0.121
	70.983	-135.676	748	1.95	0.129
	70.983	-135.676	748	2.3	0.177
N Canyon STN_68	70.986	-135.685	770	0.6	0.1

	70.986	-135.685	770	1.1	0.136
	70.986	-135.685	770	1.6	0.168
	70.986	-135.685	770	1.95	0.164
	70.986	-135.685	770	2.3	0.179
N Canyon STN_70	70.995	-135.720	828	0.6	0.072
	70.995	-135.720	828	1.1	0.11
	70.995	-135.720	828	1.6	0.141
	70.995	-135.720	828	1.95	0.136
	70.995	-135.720	828	2.3	0.148
N Canyon STN_71	71.003	-135.750	865	1.1	0.039
	71.003	-135.750	865	1.6	0.067
	71.003	-135.750	865	1.95	0.07
	71.003	-135.750	865	2.3	0.142
S of slide STN_111	70.568	-136.042	115	1.3	-1.462
	70.568	-136.042	115	1.8	-1.325
	70.568	-136.042	115	2.3	-1.33
S of slide STN_113	70.569	-136.043	110	0.6	-1.425
	70.569	-136.043	110	0.95	-1.369
Central Shelf STN_81	70.844	-135.138	230	0.6	0.15
	70.844	-135.138	230	0.95	0.034
	70.844	-135.138	230	1.3	-0.154
	70.844	-135.138	230	1.8	-0.171
	70.844	-135.138	230	2.3	-0.192
Central Shelf STN_83	70.841	-135.131	210	0.95	-0.268
	70.841	-135.131	210	1.3	-0.428
	70.841	-135.131	210	1.8	-0.497
	70.841	-135.131	210	2.3	-0.563
Central Shelf STN_85	70.839	-135.126	190	0.6	-0.942
	70.839	-135.126	190	0.95	-0.785
	70.839	-135.126	190	1.3	-1.07
	70.839	-135.126	190	1.8	-0.943
	70.839	-135.126	190	2.3	-0.649
Central Shelf STN_87	70.838	-135.123	185	1.3	-0.709
	70.838	-135.123	185	1.8	-0.786
	70.838	-135.123	185	2.3	-0.506
Central Shelf STN_89	70.834	-135.114	180	0.6	-0.93
	70.834	-135.114	180	0.95	-0.826
	70.834	-135.114	180	1.3	-0.766
	70.834	-135.114	180	1.8	-0.928
	70.834	-135.114	180	2.3	-0.919
Central Shelf STN_91	70.833	-135.109	179	0.6	-1.01
	70.833	-135.109	179	0.95	-1.027
	70.833	-135.109	179	1.8	-1.115
	70.833	-135.109	179	2.3	-0.798

References

Atkinson, G.M., Charlwood, R.G., 1988. Seismic hazard maps for northern and western Canadian offshore regions. Canada Oil and Gas Lands Administration Special Publication. Natural Resources Canada, Ottawa (March 1988).

Best, A. I., Gunn, D.E., 1999.Calibration of marine sediment core loggers for quantitative acoustic impedance studies. Marine Geology 160, 137-146.

Bekryaev, R. V., I. V. Polyakov, and V. A. Alexeev, 2010: Role of polar amplificationin long-term surface air temperature variations and modern Arctic warming. J.Clim., 23, 3888–3906.

Blasco, S., Bennett, R., Brent, T., Burton, M., Campbell, P., Carr, E., Covill, R., Dallimore, S., Davies, E., Hughes-Clarke, J., Issler, D., MacKillop, K., Mazzotti, S., Patton, E., Shearer, J., White, M., 2013. 2010 state of knowledge: Beaufort Sea seabed geohazards associated with offshore hydrocarbon development. Geological Survey of Canada Open File 6989 (307 pp.).

Blasco, S., Bennett, R. Brent, T., Campbell, C., Carr, R., Covill, S., Dallimore, S., Davies, E., Hughes-Clarke, J., Issler, D., MacKillop, K., Mazzotti, S., Patton, E., Shearer, J. and White, M., 2011.2010 Status of knowledge Geological Survey of Canada, Open File Report, 6989.335 pp.

Blasco, S., Woodworth-Lynas, C., Rankin, S., Hawkins, J., Dingler, J., 2012.Outer shelf and upper slope seabed dynamics. Canadian Beaufort Sea based on Geological Data. ArcticNet Annual Science Meeting, December 10–13 (Vancouver, B.C. Program with Abstract http://www.arcticnetmeetings.ca/asm2012/index.php).

Bloch, J. and Issler, D.R., 1996. Petrographic and geochemical analyses of Beaufort-Mackenzie Basin shales.Geological Survey of Canada, Open File 3220, 95 p.

Bohrmann, G and Torres, ME, 2006. Gas hydrates in marine sediments. In: Schulz, HD and Zabel, M (eds.) Marine Geochemistry. Springer, Berlin Heidelberg, 481-512. ISBN 3540321438

Bringué, M., Rochon, A., 2012. Late Holocene paleoceanography and climate variability over the Mackenzie Slope (Beaufort Sea, Canadian Arctic). Marine Geology 291–294, 83–96.

Bromhead, E.N., 1979. A simple ring shear apparatus. Ground Eng., 12, 40-44.

Campbell, A., Carr, E., White, M., Campbell, P., Breton, C., and Blasco, S.M., 2008.2007 Beaufort Sea Mapping Program – Geological Analysis. Draft Report prepared by Canadian Seabed Research Ltd. for the Geological Survey of Canada.

Campbell, A., White, M., Campbell, P., and Blasco, S.M., 2007. 2006 Beaufort Sea Mapping Program – Geological Analysis. Draft Report prepared by Canadian Seabed Research Ltd. for the Geological Survey of Canada.

Campbell, P., Carr, E., Beaton, F., and Blasco, S.M., 2009. 2009 Beaufort Sea Seabed Mapping Program - Operations Report. Draft Report prepared by Canadian Seabed Research Ltd. for the Geological Survey of Canada.

Campbell, P., Kendell, K., Orlando, L., and S.M. Blasco, 2002. 2001 Beaufort Sea Ice Scour Repetitive Mapping Program, Canadian Beaufort Sea. Draft Report prepared by Canadian Seabed Research Ltd. for the Geological Survey of Canada; 129 pp.

Campbell, P., White, M., Oickle, E., and S.M. Blasco, 2004. 2003 Sediment Transport Study at Artificial Island Sites, Canadian Beaufort Sea. Draft Report prepared by Canadian Seabed Research Ltd. for the Geological Survey of Canada.

Carslaw, H. S., and Jaeger, J. C., 1959.Conduction of heat in solid, 2nd edition, Claredon Press, 510p.Kim, Y.-G.et al. ,2010. New heat flow measurements in the Ulleung Basin, East Sea (Sea of Japan): relationship to local BSR depth, and implications for regional heat flow distribution, Geo-Marine Letters, 30, 595-603.

Carson, M.A., Jasper, J.N., Conly, F.M., 1998. Magnitude and sources of sediment input to the Mackenzie Delta, Northwest Territories, 1974–94. Arctic 51 (2), 116–124.

Cassidy, J.F., Rogers, G.C., Lamontagne, M., Halchuk, S., Adams, J., 2010. Canada's earthquakes: 'the good, the bad, and the ugly'. Geoscience Canada 37, 1–16.

Chen, Z., Osadetz, K.G., Issler, D.R. and Grasby, S.E., 2010. Pore pressure patterns in Tertiary successions and hydrodynamic implications, Beaufort-Mackenzie Basin, Canada. Bulletin of Canadian Petroleum Geology, v. 58, no. 1, p. 3-16.

Chen, Z., Osadetz, K.G., Issler, D.R. and Grasby, S.E., 2008. Hydrocarbon migration detected by regional temperature field variations, Beaufort-Mackenzie Basin, Canada. American Association of Petroleum Geologists Bulletin, v. 92, no. 12, p. 1639-1653.

Climate Change 2014: Synthesis Report. Contribution of Working Groups I, II and III to the Fifth Assessment Report of the Intergovernmental Panel on Climate Change [Core Writing Team, R.K. Pachauri and L.A. Meyer (eds.)]. IPCC, Geneva, Switzerland, 151 pp.

IPCC, 2014: Climate Change 2014: Impacts, Adaptation, and Vulnerability. Part A: Global and Sectoral Aspects. Contribution of Working Group II to the Fifth Assessment Report of the Intergovernmental Panel on Climate Change [Field, C.B., V.R. Barros, D.J. Dokken, K.J. Mach, M.D. Mastrandrea, T.E. Bilir, M. Chatterjee, K.L. Ebi, Y.O. Estrada, R.C. Genova, B. Girma, E.S. Kissel, A.N. Levy, S. MacCracken, P.R. Mastrandrea, and L.L. White (eds.)]. Cambridge University Press, Cambridge, United Kingdom and New York, NY, USA, 1132 pp.

IPCC, 2014: Climate Change 2014: Impacts, Adaptation, and Vulnerability. Part B: Regional Aspects. Contribution of Working Group II to the Fifth Assessment Report of the Intergovernmental Panel on Climate Change [Barros, V.R., C.B. Field, D.J. Dokken, M.D. Mastrandrea, K.J. Mach, T.E. Bilir, M. Chatterjee, K.L. Ebi, Y.O. Estrada, R.C. Genova, B. Girma, E.S. Kissel, A.N. Levy, S. MacCracken, P.R. Mastrandrea, and L.L. White (eds.)]. Cambridge University Press, Cambridge, United Kingdom and New York, NY, USA, 688 pp.

COGLA, 1989.Report of Investigation of Events Culminating in a Blowout of Gas at Gulf et al. Immiugak N-05.Canada Oil and Gas Lands Administration, Energy, Mines and Resources Canada, and Indian and Northern Affairs Canada, 31 p.

Feseker, T, Pape, T, Wallmann, K, Klapp, SA, Schmidt-Schierhorn, F and Bohrmann, G, 2009. The thermal structure of the Dvurechenskii mud volcano and its implications for gas hydrate stability and eruption dynamics. Marine and Petroleum Geology, 26(9). 1812-1823.

Fofonoff, N. P, Millard, R. C., Unesco, 1983.Unesco Algorithms for computation of fundamental properties of seawater. Ausgabe 44 von Unesco technical papers in marine science, Unesco

Fortin G. & Blasco S.M., 1990.Regional Geological Framework for the Late Neogene / Quaternary Strata Beneath The Canadian Beaufort Continental Shelf. Report submitted to the Geological Survey of Canada.

Frederick, J. M., and B. A. Buffett, 2015.Effects of submarine groundwaterdischarge on the present-day extentof relict submarine permafrost andgas hydrate stability on the BeaufortSea continental shelf, Journal of Geophysical Research:. Earth Surface., 120, 417–432.

Ghafghazi, M., and Shuttle, D.A., 2010. Interpretation of in situ density from seismic CPT in Fraser River sand. In Proceedings of Second International Symposium of the Cone Penetration Test, CPT '10, Huntington Beach, Calif., 9–11 May 2010.

Hart, P.E. ,Pohlman, J.W. , Lorenson, T.D. and Edwards B.D., 2011 Deep water gas hydrate recovery from a seafloor mound in a regional of widespread BSR occurrence. International Conference on Gas Hydrates, Edinburg, Scotland, U.K., July 17-21. pp. 16

Hill, P.R., Mudie, P.J., Moran, K., Blasco, S.M., 1985. A sea-level curve for the Canadian Beaufort Shelf. Canadian Journal of Earth Sciences 22, 1383–1393.

Hitchon, B., Underschultz, J.R.,Bachu, S. andSauveplane, C.M., 1990. Hydrogeology, geopressures and hydrocarbon occurrences, Beaufort-Mackenzie Basin. Bulletin of Canadian Petroleum Geology, v. 38, no. 2, p. 215-235.

Hottmann, C.E. and Johnson, R.K., 1965. Estimation of formation pressures from log-derived shale properties. Journal of Petroleum Technology, v. 17, p. 717-722.

Hughes-Clarke, J.E., L.A. Mayer, and D.E Wells, 1996. Shallow-water imaging multibeam sonars: A new tool for investigating seafloor processes in the coastal zone and on the continental shelf, Marine Geophysical Researches, 18: 607-629.

Hunter, J. A., Neave, K. G., MacAulay, H. A., and Hobson, G. D., 1978 Interpretation of Sub-Seabottom Permafrost in the Beaufort Sea by Seismic Methods; Part 1: seismic refraction methods. Proceedings of the third International Permafrost Conference, V.1, p.514-520.

Issler, D.R., 1992. A new approach to shale compaction and stratigraphic restoration, Beaufort-Mackenzie Basin and Mackenzie Corridor, northern Canada. American Association of Petroleum Geologists Bulletin, v. 76, p. 1170-1189.

Issler, D.R., Hu, K., Bloch, J.D. andKatsube, T.J., 2002a. Organic carbon content determined from well logs: examples from Cretaceous sediments of Western Canada. Geological Survey of Canada, Open File 4362. (CD-ROM or poster)

Issler, D.R. and Jessop, A.M., 2011. Thermal conductivity analysis of Cenozoic, Mesozoic and Paleozoic coresamples, Beaufort-Mackenzie Basin, northern Canada; Geological Survey of Canada, Open File 6734, 128 p.

Issler, D R; Hu, K; Lane, L S; Dietrich, J R. Geological Survey of Canada, Open File 5689, 2011; 1 CD-ROM.

Issler, D.R., Hu, K., Lane, L.S. and Dietrich, J.R. in press. GIS Compilations of Depth to Overpressure, Permafrost Distribution, Geothermal Gradient, and Regional Geology, Beaufort Mackenzie Basin, Northern Canada. Geological Survey of Canada, Open File 5689.

Issler, D.R., Katsube, T.J., Bloch, J.D. and McNeil, D.H., 2002b. Shale compaction and overpressure in the Beaufort-Mackenzie Basin.

Jessop, A.M., 1990. Thermal Geophysics. Developments in Solid Earth Geophysics 17, New York,Elsevier, p. 36-38.

Jin, Y. K., Riedel ,M., Shipboard scientific party, 2014. ARA04C Cruise Report, Korea Polar Research Institute, 174 pages.

Kang, S.H., 2012. Cruise Report: RV Araon ARA03B, August 1 – September 10, 2012. ChukchiBorderlandandMendeleyevRidge. pp. 1–174. Weber, M.E., Niessen, F., Kuhn, G., Wiedecke, M., 1999. Calibration and application of marine sedimentary physical properties using a multi-sensor core logger, Marine Geology 136, 151-172.

Katsube, T.J. and Issler, D.R., 1993. Pore-size distributions of shales from the Beaufort-Mackenzie Basin, northern Canada. In: Current Research, Part E, Geological Survey of Canada, Paper 93-1E, p. 123-132.

Kim, Y.-G.et al., 2013. The stability of gas hydrate field in the northeastern continental slope of Sakhalin Island, Sea of Okhotsk, as inferred from analysis of heat flow data and its implications for slope failures, Marine and Petroleum Geology, 45, 198-207.

Lamontagne, M., Halchuk, S., Cassidy, J.F., Rogers, G.C., 2008. Significant Canadian earthquakes of the period 1600–2006. Seismological Research Letters 79, 211–223.

McCutcheon, S.C., Martin, J.L, Barnwell, T.O. Jr., 1993. Water Quality in Maidment, D.R. (Editor).Handbood of Hydrology, McGraw-Hill, New York, NY (p. 11.3)

McNeil, D.H., Dietrich, J.R., Issler, D.R., Grasby, S.E., Dixon, J. and Stasiuk, L.D., 2010. A new method for recognizing subsurface hydrocarbon seepage and migration using alteredforaminifera from a gas chimney in the Beaufort-Mackenzie Basin. In: L. Wood, ed., Shale Tectonics: American Association of Petroleum Geologists Memoir 93, p. 197 - 210.

Meigh, A.C., 1987 "Cone Penetration Testing - Methods and Interpretation", CIRIA,Butterworths.

Melling,H., DFO Canada, Science Plan for CCGS Sir Wilfrid Laurier, September-October 2013,IOS Cruise 2013-22.

Nixon, Mark F.; Grozic, Jocelyn L. H., 2006. A simple model for submarine slope stability analysis with gas hydrates. Norwegian Journal of Geology / NorskGeologisk Forening;2006, Vol. 86 Issue 3, p309

O'Regan, M., de Vernal, A., St-Onge, G., Hillaire-Marcel, C., Rochon, A., 2013. Coring and seismic surveying seaward of the Mackenzie Trough in support of IODP proposal 753 for drilling in the Beaufort Sea.(3 pp. Proposal to SI Nam).

Osadetz, K and Chen, Z., 2010. A re-evaluation of Beaufort Sea-Mackenzie Delta basin gas hydrate resource potential: petroleum system approaches to non-conventional gas resource appraisal and geologically-sourced methane flux Bulletin of Canadian Petroleum Geology; March 2010; v. 58; no. 1; p. 56-71.

Park, K.-P, Bahk, J.-J., Kwon, Y., Kim, G.-Y., Riedel, M., Holland, M., Schultheiss, P., Rose, K., and the UBGH-1 Scientific Party, 2008. Korean national program expedition confirm rich gas hydrate deposits in the Ulleung Basin, East Sea. DOE-NETL Fire In the Ice, Spring, 2008: 6-9, http://www.netl.doe.gov/technologies/oil-gas/publications/Hydrates/Newsletter/HMNews Spring 08.pdf#page=6.

Paull C.K., Ussler W III, Dallimore S.R., Blasco S.M., Lorenson T.D., Melling H, Medioli B.E., Nixon F.M., and McLaughlin F.A. 2007. Origin of pingo-like features on the Beaufort Sea shelf and their possible relationship to decomposing methane gas hydrates. Geophysical Research Letters 2007; 34(1).

Paull, C. , Dallimore, S. , Hughes-Clarke, J. , Blasco, S. , Lundsten, E. , Ussler, w. , Graves, D. , Sherman, A., Conway, K., Melling, M., Vagle, S., and Collett, T. 2011 . Tracking the decomposition of submarine permafrost and gas hydrate under the shelf and slope of the Beaufort Sea. 8th International Conference on Gas Hydrates, Edinburg, Scotland, U.K., July 17-21. in press.

Pelletier, B.R., 1987. Marine Science Atlas of the Beaufort Sea, Geology and Geophysics.Geological Survey of Canada, Miscellaneous Report 40.

Pfender, M., and Villinger, H., 2002. Miniaturized data loggers for deep sea sedimenttemperature gradient measurements, Marine Geology, 186, 557 - 570.

Riedel,M., Villinger, H, Aßhoff, K, Kaul, N., Dallimore, S.R., 2014. Teperature measurements andthermal gradient estimates on the slope and shelf edge region of the Beaufort Sea, Canada,Geological Survey of Canada, Open File 7725.

Riedel, M., Collett, T.S., Malone, M.J., and the Expedition 311 Scientists, 2006a. Proc. Integrated Ocean Drilling Program, IODP 311, Washington, D.C.

Ruffel, J.P, Murphy, T.R. and Graham C. 1988. Planning and execution of a 500m corehole through permafrost, Proceedings, Fourth Canadian Permafrost Conference: Ottawa, National Research Council of Canada,

Saint-Ange, F., Kuus, P., Blasco, S., Piper, D.J.W., Clarke, J.H., MacKillop, K., 2014. Multiple failure styles related to shallow gas and fluid venting, upper slope Canadian Beaufort Sea, northern Canada. Mar. Geol. 355, 136 – 149.

Schell, T.M., Scott, D.B., Rochon, A. and Blasco, S., 2008. Late Quaternary paleoceanographic and paleo-sea ice conditions in the Mackenzie Trough and Canyon, Beaufort Sea. Canadian Journal of Earth Science, 45, 1399-1415.

Schlitzer, R., Ocean Data View, http://odv.awi.de, 2014.

Scott, D.B., Schell, T., St-Onge, G., Rochon, A., Blasco, S., 2009. Foraminiferal assemblage changes over the last 15,000 years on the Mackenzie–Beaufort Sea Slope and Amundsen Gulf, Canada: Implications for past sea ice conditions. Paleoceanography 24, PA2219. http://dx.

Smith, S.L. and Judge, A.S. 1993. Gas hydrate database for Canadian Arctic and selected East Coast wells. Geological Survey Canada. Open File Report 2746, 120 p.

Schell, T.M., Scott, D.B., Rochon, A., Blasco, S., 2008. Late Quaternary paleoceanography and paleo-sea ice conditions in the Mackenzie Trough and Canyon, Beaufort Sea. Canadian Journal of Earth Sciences 45 (11), 1399–1415.

Sultan, N., 2007. Excess pore pressure and slope failure resulting from gas hydratesdissociation and dissolution. In: Conference, O.T. (Ed.), Offshore TechnologyConference. OTC, Houston, Texas, p. 18532.

Sultan, N., P. Cochonat, J. P. Foucher, and J. Mienert, 2004. Effect of gashydrates melting on seafloor slope instability, Mar. Geol., 213(1 – 4),379– 401.

Terzaghi, K. (1942), Theoretical Soil Mechanics, New York: Wiley, ISBN 978-0-471-85305-3

Thomson, J., Dingler, J., Blasco, S. Hughes-Clarke, J., 2010. Integration of multiple data types for geohazard survey planning, Canadian Beaufort Sea. ArcticNet Annual Science Meeting 2010, Ottawa, Ontario, 14-17, 2010.

Tishchenko, P. et al., 2005. Calculation of the stability and solubility of methane hydrate in seawater, Chemical Geology, 219, 37-52.

Von Herzen, R. P.,andUyeda, S., 1963. Heat flow through the Eastern Pacific Ocean floor, Journal of Geophysical Research, 68, 4219-4250.

Von Herzen, R. P.,and Maxwell, A. E., 1959. The measurement of Thermal Conductivity of Deep-Sea Sediments by a Needle-Probe Method, Journal of Geophysical Research, 10, 1557-1563.

Weaver, J.S., and Stewart, J.M., 1982. In situ hydrates under the Beaufort Sea Shelf, in French H.M., ed., Proceedings, Fourth Canadian Permafrost Conference: Ottawa, National Research Council of Canada, p. 312-319.

Yamano, M. et al., 1982. Estimates of heat flow derived from gas hydrates, Geology, 10, 339-343.

Yamano, M. et al, 2008. High heat flow anomalies on an old oceanic plate observed seaward of the Japan Trench, International Journal of Earth Sciences, 97, 345-